Development of Multiparametric MRI Models for Prostate Cancer Detection based on Improved Correlative Pathology

A Dissertation
SUBMITTED TO THE FACULTY OF
UNIVERSITY OF MINNESOTA
BY

Chaitanya Kalavagunta

IN PARTIAL FULFILLMENT OF THE REQUIREMENTS
FOR THE DEGREE OF
DOCTOR OF PHILOSOPHY

Advisor: Gregory J. Metzger
June 2014

Acknowledgements

This PhD work is based on my original contributions to a large interdisciplinary research project led by Dr. Greg Metzger that involved departmental teams across CMRR, Pathology, Urology, Radiology and Biostatistics.

First of all, I would like to thank my advisor, Greg Metzger, PhD. Greg has been always open to new ideas and has always made himself available to answer my research questions. On a personal level I am grateful to him because I have come this far only because of his support and encouragement.

I would like to thank Drs. Patrick Bolan, Bruce Hammer and Essa Yacoub for being on my thesis committee and for their kind support. I am especially grateful to Prof. Russell Ritenour and Prof. Bruce Gerbi for their guidance towards my academic and career pursuits.

I would like to thank my funding sources NCI RO1 CA131013 (primary funding), NCI R01 CA131013-S1, NIBIB P41 EB015894, UMN Department of Urology Bridge Funding and the UMN Graduate School (Doctoral Dissertation Fellowship)

This project would not have been possible without the support of many people. I am thankful to Drs Xiangmin Zhou (LATIS Image Registration), Joseph Koopmeiners (Predictive Modeling), Stephen Schmechel (Pathology Annotation), and Patrick Bolan (Interpolation and XML parsing scripts).

My thanks to Brian Hanna for his amazing all-round IT support and for being a workplace inspiration. Thanks to Jonathan Henriksen, Laura Moench, Sarah Bowell and Andy Johnson for their help with Pathology processing. Special thanks to Diane Hutter for her help with the blood collection and in scheduling and running the MRI studies. My thanks to our clinical partners Drs

Badrinath Konety, and Christopher Warlick. Finally, I would like to thank all the people at CMRR who have helped and supported me all these years and made my stay enjoyable.

Dedication

Jai Sai Ram.

To my parents and my brother who have always encouraged me to achieve new heights.

To my loving daughter Neelu, who is too young to understand the subject matter but is glad that her father is home, my thanks are to you too for cheering me on in your own way.

To my best friend and my wife Janani, there are no words that can express my thanks. Let’s go out and get some coffee.

Table of Contents

List of Tables

List of Figures

List of Abbreviations

PCa – Prostate Cancer

MRI – Magnetic Resonance Imaging

MP-MRI – Multiparametric MRI

DWI – Diffusion Weighted Imaging

DCE – Dynamic Contrast Enhanced

MRSI – Magnetic Resonance Spectroscopy Imaging

ADC – Apparent Diffusion Coefficient

CG – Central Gland

PZ – Peripheral Zone

TZ – Transition Zone

CZ – Central Zone

PSA – Prostate Specific Antigen

DRE – Digital Rectal Exam

TRUS – Transurethral Ultrasound

GS – Gleason Score

qMR – Quantitative MR

ROI – Region of Interest

GFR – Glomerular Filtration Rate

RP – Radical Prostatectomy

ERC – Endorectal Coil

T2w – T2 weighted

TSE – Turbo Spin Echo

SEMC – Spin Echo Multi Contrast

EPI – Echo Planar Imaging

DESPOT1 – Driven Equilibrium Single Pulse Observation of T1

VIBE – Volume Interpolated Breathold Examination

SAR – Specific Absorption Rate

TE – Echo Time

K^{trans} – Forward Volume Transfer Constant

K_{ep} – Reflux Rate between the Extracellular Space and the Plasma

V_e – Fractional Extravascular Extracellular Space

AUGC – Area Under Gadolinium Curve

AIF – Arterial Input Function

H&E – Hematoxylin and Eosin

PWM – Pseudo Whole Mount

QMHS – Quarter Mount Histological Section

LATIS – Local Affine Transformation guided by Internal Structures

DSC – Dice Similarity Coefficient

ERCinMR– in vivo MR image obtained using ERC

TRE – Target Registration Error

inMR – in vivo MR

exMR – ex vivo MR

MI – Mutual Information

COFEMI – COmbined Feature Ensemble Mutual Information

SWMI – Spatially Weighted Mutual Information

BSp – Beta Spline

TPS – Thin Plate Spline

ANN – Artificial Neural Network

GEE – Generalized Estimating Equations

CAD – Computer Aided Diagnosis

PPP – Post Prostatectomy Pathology

IL – Index Lesion

SL – Secondary Lesion

IL – Tertiary Lesion

PC – Pseudo Capsule

ROC – Receiver Operator Characteristic

$ROC_{0.1}$ – Sensitivity value on ROC curve corresponding to 90% specificity

CBS – Composite Biomarker Score

LASSO – Least Absolute Shrinkage and Selection Operator

OVB – Oxygenated Venous Blood

CA –Contrast Agent

AS – Aqueous Solution

GaD – Gd-DTPA

IR-TFL – Inversion recovery Turbo Flash

pO_2 – Partial Pressure of O_2

sO_2 – Hemoglobin Oxygen Saturation

Hct – Hematocrit

T_1 – Longitudinal Relaxation Time

T_2 – Transverse Relaxation Time

T_2* – Apparent Transverse Relaxation Time

R_1 – Longitudinal Relaxation Rate

R_2 – Transverse Relaxation Rate

R_2* – Apparent Transverse Relaxation Rate

r_1 – T_1 relaxivity

r_2 * – T_2* relaxivity

Thesis Statement

Prostate cancer (PCa) is a prevalent disease which affects 1 in 6 men in the United States and has overtaken lung cancer as the leading cause of cancer related deaths in American men and number two worldwide (1). While diagnosis and treatment options are improving, there is still a fundamental problem with its management. It is unclear which PCa is aggressive (life- threatening) and which is non-aggressive (non-life threatening). As a result, overtreatment of PCa results from the absence of tools that can properly differentiate between the two. While magnetic resonance imaging has become an increasingly valuable tool in the management of men with PCa, its use to identify aggressive disease and characterize extent have yet to be developed. The ability to identify the extent of significant disease would increase the effectiveness of focal therapy including cryosurgery and RF ablation which are currently hampered by the absence of good information for targeting treatment. Currently available treatments such as radiation therapy and surgery address the whole gland, while focal therapies treat part of the gland and can more effectively avoid damaging critical structures. Improved detection and evaluation of extent will impact areas of prostate cancer management by improving biopsy yield especially with the growth of MRI targeted biopsies both in the gantry and fused with real-time Ultrasound(2).

Among several diagnostic imaging tests that are available for detection of PCa in the market today, Magnetic Resonance Imaging (MRI) occupies a unique position due to its excellent soft tissue contrast and its ability to generate tissue property dependent multi-parametric data (3). Multi-parametric MRI (MP-MRI) refers to the combination of multiple imaging methods and their associated

quantitative maps such as apparent diffusion coefficient (ADC) maps from diffusion weighted imaging (DWI), pharmacokinetic maps from dynamic contrast enhanced MRI (DCE-MRI) and metabolite ratio maps from three dimensional MR spectroscopic imaging (3D-MRSI). With DWI, MP-MRI can help in tumor identification by mapping areas of restricted diffusion of water molecules that indicate micro-structural changes in cellular density. Angiogenesis, the growth of new blood vessels, is an indicator of cancerous tissue. Using DCE-MRI, we can probe heterogeneous neovascular structure and abnormal vessel permeability that is indicative of cancer. 3D-MRSI is another MR technique that detects cancer by mapping the chemical composition of the prostate (2,3). MP-MRI has been shown to increase sensitivity and specificity compared to any single MRI dataset.

The ability to develop and evaluate MP-MRI to prospectively detect disease, assess aggressiveness and delineate extent, first requires the retrospective validation against post-surgical pathology sections. Despite the large effort made by many groups in this area of research, the correlation of in vivo MP-MRI with pathology is still a challenge and to date is insufficient to develop highly accurate models of disease. To address this problem this thesis showcases:

1. A novel registration approach called LATIS (Local Affine Transformation assisted by Internal Structures) for co-registering post prostatectomy pseudo-whole mount (PWM) pathological sections with in vivo MRI images. This work is presented in **Chapter 3**.
2. A MP-MRI based predictive model for disease detection using a composite biomarker score based on a unique database of pathology co-registered MR data sets. This work is presented in **Chapter 4**.

Chapter 2 details the clinical characteristics of the patient cohort and the MP-MRI acquisition methods and post processing used to generate the data used in chapters **3** and **4**. **Chapter 5** reports on a study where the r_1 and r_2* relaxivities of a common paramagnetic contrast agent are measured in blood and saline at both 3T and 7T. This is important information to have when attempting to perform DCE-MRI studies as part of a MP-MRI protocol. Previous studies done by Metzger et al. (4) have shown that, R_2* effects of typical paramagnetic contrast agents make the determination of subject dependent arterial input functions impossible at 7T and results in an underestimation of pharmacokinetic parameters even if a model based function is used. Similar effects are expected to negatively impact other contrast enhanced studies when performed at 7T such as first pass perfusion and angiography exams relying on T1-weighted enhancement (5). Finally, **Chapter 6** reports on some initial studies comparing MP-MRI with quantitative pathology while also highlighting future directions for the work contained in this thesis.

Chapter 1 Introduction

1.1 Prostate Cancer

According to the GLOBOCAN (Global Burden of Cancer Study) project, which provides contemporary estimates of the incidence, mortality and prevalence from major types of cancer at the national level, for 184 countries of the world, Prostate Cancer (PCa) was the second most common cancer among men worldwide (1) as of 2012. It is estimated that in 2014, 233,000 new cases of PCa will be diagnosed and 29,480 men will die of this disease in the United States alone(6). According to the American Cancer Society, 98.9% of men survive for five years or more after being diagnosed with all stages of PCa (local, regional or distant) (6). The increase of this 5-year survival percentage from 98.9 to 100% for men diagnosed with localized and regional PCa is attributed to early diagnosis of disease (7).

1.2 Prostate Anatomy

The prostate is a walnut-sized gland (Figure 1.1) located inferior to the bladder, superior to the penis and anterior to the rectum. A healthy prostate weighs around 20 to 25 grams, has a volume around 20 cc and measures around 3 cm x 4cm x 2cm. The prostate consists of a base, an apex, anterior, posterior and two lateral surfaces and has the urine in the bladder run through its center via the urethra. The main function of the prostate is to produce a thin, milky fluid containing citric acid and acid phosphatase that is added to the seminal fluid at the time of ejaculation. Also seen in Figure 1.1 are the seminal vesicles, which are a pair of small tubular glands that are attached to the *vas deferens* (carrying-away vessels) at the base of the bladder. The seminal vesicles produce fructose

that helps with the sperm motility. The fluid from the seminal vesicles makes up most of the volume of the ejaculatory fluid (8-13).

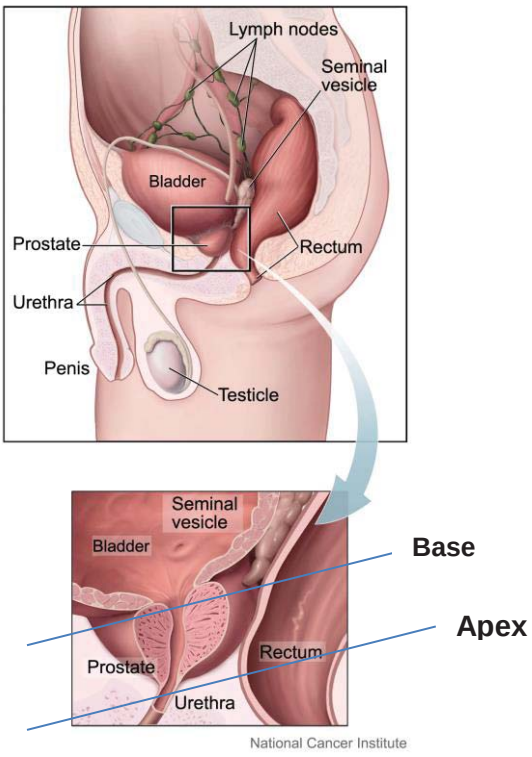

Figure 1.1 shows the anatomy of the prostate in relation to other pelvic structures. Inset figure shows an enlarged view along with the base and apex. This image is provided courtesy of the National Cancer Institute website (http://www.cancer.gov).

The prostate gland is divided into three distinct glandular regions each distinguishable from the other on the basis of histology, anatomical landmarks and susceptibility to pathologic disorders (14). These are the peripheral zone (PZ), which covers 70% of the prostate, central zone (25%), transition zone (TZ) (5%) and anterior Fibromuscular Stroma (5%). Figures 1.2 and 1.3 show these glandular zones in the form of a diagram and as seen on a T_2-weighted MRI image respectively.

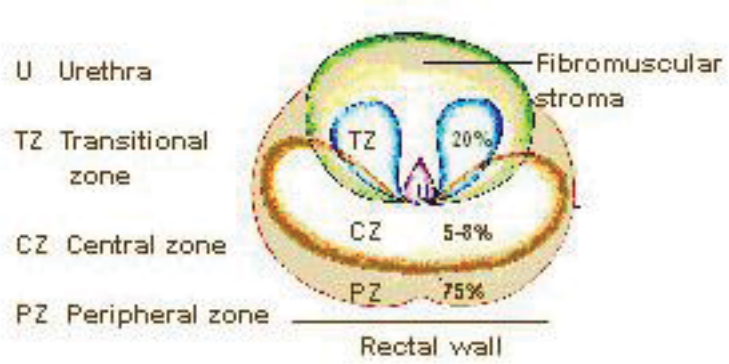

Figure 1.2 shows an axial view of the prostate showing zonal anatomy. The central gland (CG) as defined in this thesis (not shown in figure) is composed of everything other than PZ (i.e. TZ, CZ, Fibromuscular stroma). This image has been provided courtesy of SEER Prostate Cancer Training Module, U.S. National Institutes of Health, National Cancer Institute (http://training.seer.cancer.gov/).

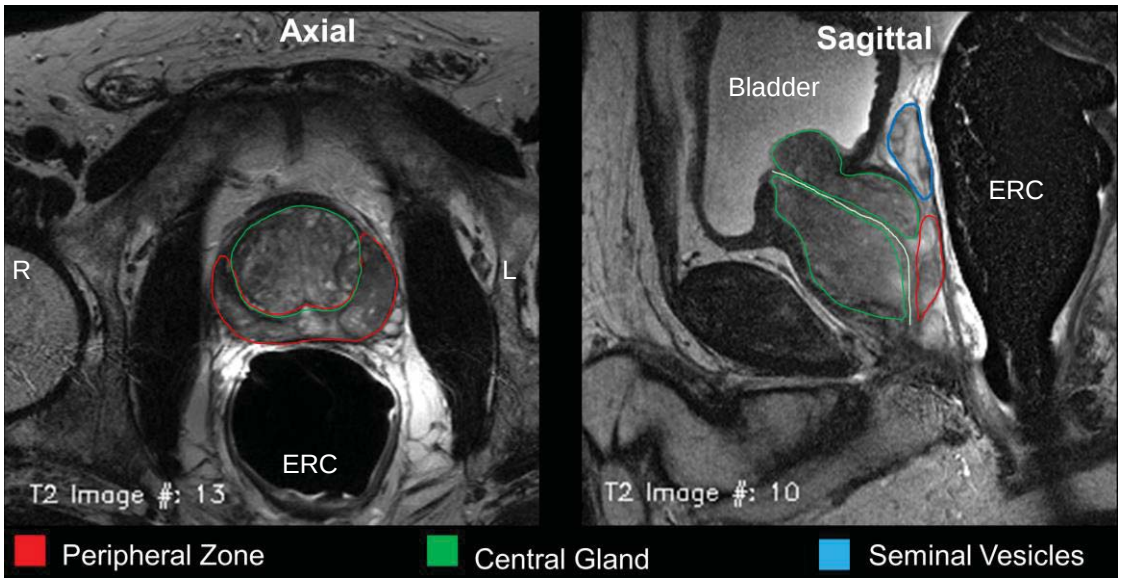

Figure 1.3 shows the zonal anatomy of the prostate as seen on a T_2-weighted MRI. The axial (a) and sagittal (b) images were obtained on a 3T Siemens Magnet using an endorectal coil (ERC). The center of the urethra is depicted by the yellow line.

1.3 Cancer Diagnosis

Adenocarcinomas (cancerous tumors) that arise from the glandular tissue make up 95% of PCa tumors. 75% of all PCa arises in the PZ, 20% in the TZ and about 5-10% in the CZ while local extension of disease tends to be into capsule, bladder base and the seminal vesicles. PCa usually does not present any symptoms unless it reaches a very advanced stage. Most common local symptoms present themselves are urinary outflow obstruction and back pain (15). The serum PSA (Prostate Specific Antigen) level test, DRE (Digital Rectum Examination) and TRUS (Transrectal Ultrasound) guided biopsy are the three clinical examinations used for early diagnosis of PCa. A prostate biopsy is recommended to patients with an elevated PSA level (> 4 ng/mL) in their blood and a suspicious induration on DRE. TRUS guided biopsy is the current gold-standard for prostate biopsies. While a prostate biopsy may be performed to confirm the presence of tumor at the location of a positive DRE and detect the cause of the elevated PSA, TRUS guided biopsies have shown low sensitivity (23-42%) (16,17).

Biopsy results are graded with a Gleason Score (GS) which is based on the glandular pattern description of the tumor. The GS is a two part sum of the primary (predominant) and secondary (second most prevalent) grades, each on a scale of 1 (well differentiated) to 5 (least differentiated). Well-differentiated cancer cells resemble normal cells and are inclined to grow and spread at a slower rate than un-differentiated cancer cells that may lack normal tissue architecture (Figure 1.4). The GS score ranges from 2 to 10 and indicates the likeliness of a tumor to spread. A GS of 7 (3+4 or 4+3) is considered clinically significant with a worse prognosis than a GS of 6 (i.e. 3+3) (18-22).

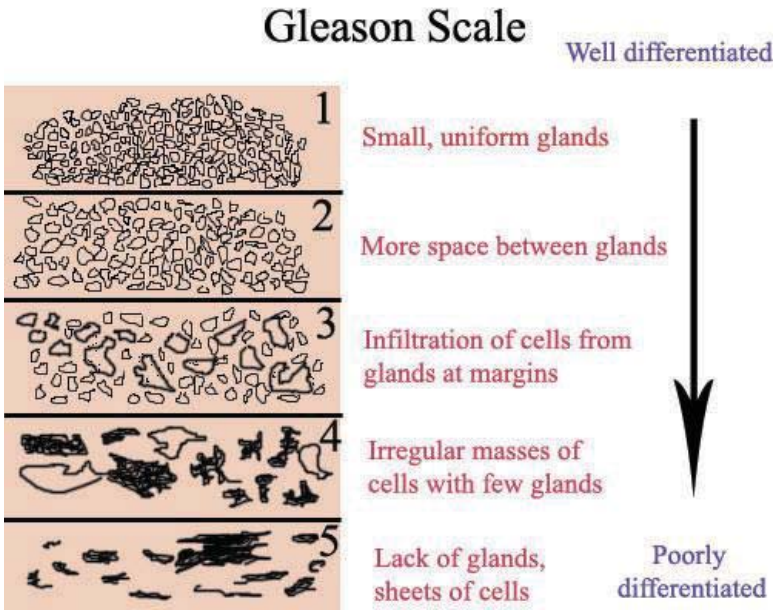

Figure 1.4 Gleason Scale (image courtesy – Wikimedia.org).

1.4 Multiparametric MRI in the detection of Prostate Cancer

Among several diagnostic imaging modalities that are available for detection of PCa, Magnetic Resonance Imaging (MRI) occupies a unique position due to its excellent soft tissue contrast and its ability to generate tissue property dependent multi-parametric data (3). Conventional imaging techniques like CT have found limited use in PCa detection because of insufficient spatial and contrast resolution (23-25). PET/CT is currently used for detection of post-treatment recurrence and has not shown conclusive detection capabilities for primary PCa diagnosis (26-28). MP-MRI is currently one of the most promising tools for PCa detection and staging with the potential to further impact disease management by characterizing disease aggressiveness and extent (12,29-34). MP-MRI refers to

the combination of multiple imaging methods and their associated quantitative maps such as T_2 maps associated with T_2-weighted imaging, ADC maps from diffusion weighted imaging (DWI), pharmacokinetic maps from dynamic contrast enhanced MRI (DCE-MRI) and metabolite ratio maps from three dimensional MR spectroscopic imaging (3D-MRSI). Quantitative MRI (qMR) parameters like T_2, ADC, K^{trans}, K_{ep}, V_e, AUGC and those derived from MRS (Magnetic Resonance Spectroscopy) acquisitions have been shown to detect PCa and correlate with tumor grade (35-38). MP-MRI guided biopsy has shown good results in detecting significant disease and could reduce unnecessary biopsies (39,40).

1.5 Multiparametric MRI based Predictive Models in the Detection of Prostate Cancer

The ground truth in PCa detection is given by pathology. One way to achieve pathology comparable detection using MP-MRI is by the construction of a model that accurately predicts disease as defined on pathology. An MP-MRI model provides a standardized approach of combining multiple datasets for maximizing the predictive power of MP-MRI. A vast body of literature exists in the prediction of PCa using MP-MRI models and there are new studies being added every day (18-24). The process of assessing MP-MRI's ability to predict what is currently only obtained through post prostatectomy pathology (PPP), involves correlating MP-MRI obtained in-vivo (*in*MR) with post-surgical specimens. This correlation with the pathologic Gold Standard involves the transfer of information obtained from pathology (i.e. grade and location of identified disease). This mapping has been accomplished through a variety of methods in the literature: manual mapping of regions of interest (ROIs) (41); visual mapping of sextants (42) or octants (43,44); mapping locations of graded MR guided biopsy specimens (45) or calculated Gleason scores (43,46,47). The process of correlating manually

drawn regions of interest (ROIs) (41) on the MRI corresponding to identified areas of disease on pathology introduces potential biases of ROI drawing and placement used to generate predictive models. On the other hand using pathologically correlated slice sections (sextants (42), octants (43,44)) on MP-MRI is prone to data averaging when a section contains a mix of cancer and non-cancer tissue. These issues are addressed in this thesis (**Chapter 4**) where global anatomic features are used to guide a deformable registration method (LATIS) which is then used to map pathologist annotated regions of cancer directly to endorectal coil obtained in-vivo MRI images (48). The location size and extent are defined by global anatomic features. While an assumption is made about coincident slice locations and there is user interaction involved in defining internal structures for guiding the deformable registration methods, these are arguably less biased than other proposed methods. This image registration method is used to generate co-registered datasets which are then used in the development of MP-MRI based predictive models for the detection of PCa (**Chapter 4**).

Chapter 2 Materials and Methods

2.1 Patient Population

The patient cohort used in this thesis consisted of those who had biopsy confirmed PCa and were scheduled to undergo prostatectomy (46 men, age range 47 to 76 years with a median age of 63 years). All patients underwent imaging at the Center of Magnetic Resonance Research between November 2009 and August 2012 after biopsy and before surgery after providing written consent under an Institutional Review Board approved protocol. The exclusion criteria included contraindications to endorectal coil placement including severe hemorrhoids, latex allergy, surgically absent rectum, severe inflammatory bowel disease; contraindications for MRI including ferromagnetic implants, history to shrapnel or shot gun injury, body mass index ≥ 40, cardiac pacemakers, claustrophobia, large tattoos, hip replacement and penile implants; contraindications to contrast agents including strong history of asthma and allergies, colostomy, kidney disease and Glomerular Filtration Rate (GFR) < 30 ml/min and prior treatment or procedures to treat PCa. Men received radical prostatectomy (RP) after an average gap of 27 days post MRI (range: 0-385 days). The maximum gap of 385 days corresponds to a patient who was initially on active surveillance but underwent RP later. Quarter mounted histopathological sections were generated from the surgical prostate specimens. Table 2.1 shows the clinical characteristics summary of the patient population.

Characteristic	Value		
	Med	Min	Max
Age at MRI (years)	63	47	76
MRI-RP Gap (days)	15	0	385
PSA Level (ng/ml)	6.2	0.5	21.8
PPP Maximum Gleason Grade			
3+3	6		
3+4	15		
4+3	9		
4+4	6		
4+5	5		
5+4	2		
Percentage of tumors with Gleason Grade ≥ 3+4	86		

Med: Median
PSA: Preoperative Serum Prostate Specific Antigen
RP: Radical Prostatectomy
PPP: Post Prostatectomy Pathology

Table 2.1 Patient Population Clinical Characteristics

2.2 MRI acquisition and Parametric Mapping

2.2.1 Imaging Setup

Patients were imaged on a 3T scanner (Siemens Healthcare, Erlangen Germany) transmitting with the whole body coil and receiving with a balloon-type endorectal coil (ERC) combined with an external surface array. The surface array consisted of two rows of 3 elements anteriorly from a flexible body coil and two rows of 3 elements posteriorly from a spine coil. The ERC was inserted after the patient assumed the left lateral decubitus position and inflated with 60 ml of

perfluorocarbon to reduce air induced susceptibility artifacts. Rotating back into the supine position, the anterior surface array was positioned with the coil centered at the level of the greater trochanter in the foot-head direction. In later studies, a urethral catheter (Bard, Latex radiopaque urethral catheter, Robinson model, 18Ch/ french-6.0mm) was inserted with the ERC to provide a pathway to release gas from the rectum which otherwise would build up behind the endorectal coil. While not explicitly quantified, the use of the urethral catheter appeared to relieve the issue of gas in the bowel. In addition, it was inexpensive and did not affect study workflow or patient comfort as an endorectal coil was already being inserted. Other than instructing subjects to be *nil per os* (ingesting no fluids or solids) 4 hours prior to the study, no additional anti-peristaltic or preparation measures were taken.

2.2.2 MRI Acquisitions Overview

Scout images of the prostate in the sagittal, axial and coronal planes were acquired initially to check the depth and rotation of the ERC. After confirming the adequate positioning of the ERC, the rest of the MRI study proceeded and included the following acquisitions.

1. Anatomic imaging using a T_2-weighted (T_2w) Turbo Spin Echo (T_2-TSE) sequence in the axial, sagittal and coronal planes.
2. Additional TSE datasets acquired in the axial plane at different echo times for calculating T_2 maps (T_2-TSE).
3. T_1-weighted Turbo Spin Echo (T_1-TSE) imaging for the detection of post-biopsy hemorrhage.
4. Multi Echo Spin Echo imaging as an alternative method for calculating T2 maps (T_2-SEMC).
5. Single Shot Echo Planar Imaging (EPI) diffusion weighted imaging (DWI) for calculation of Apparent Diffusion Coefficient (ADC) maps.

6. 3D gradient echo data sets for calculating T_1 maps using DESPOT1 (Driven Equilibrium Single Pulse Observation of T_1).
7. Dynamic Contrast Enhanced MRI (DCE-MRI) using 3D Flash VIBE (Volume Interpolated Breathold Examination (T_1w3D-GRE).

Acquisition parameters are tabulated in Table 2.2. All studies were run in the first-level control mode with prostate specific power and B_0 adjustment. Further details for each acquisition and the calculation of parametric maps used for subsequent modeling are detailed below.

	T_2w	TSE For T_2 map	SEMC for T_2 map	T_1w	DWI	DESPOT1 for T_1 map	DCE
Sequence	TSE	TSE	SEMC	TSE	SSH-EPI	GRE	GRE
Scan Duration (mm:ss)	4:56	2:28	6:38	1:15	4:27	0:25	4:59
TR(ms)	≥6000	≥6000	6000	500	3200	4.09	4.09
TE(ms)	107	30,72,144	13.1 to 154.1	13	88	1.44	1.44
Slice Thickness (mm)	3	3	3	3	3	4	4
Acquisition Matrix	256×230	256×230	256×192	256×192	128×128	192×163	192×163
No. of Slices	19	19	19	19	19	19	19
FOV (mm)	140	140	280	160	180	220	220
Flip Angle (°)	140	140	180	120	90	2, 5, 10, 15	≤10
Echo Train Length	23	23	1	3	95	1	1
Pixel Bandwidth (kHz)	190	100	130	130	1395	401	401
Number of averages	2	2	1	1	8	4	1
Number of phase encoding steps	483	507	145	382	95	183	183
Resolution	256×256	256×256	256×256	512×512	128×128	384×384	384×384
Parallel Imaging R Factor	1	2	1	2	2	2	2
Voxel Size (mm×mm×mm)	0.54×0.54×3	0.54×0.54×3	1.09×1.09×3	0.31×0.31×3	1.40×1.40×3	0.57×0.57×4	0.57×0.57×4
In Plane Phase Encode Direction	Row	Row	Row	Row	Row	Column	Row
Temporal resolution (s)	n.a	n.a	n.a	n.a	n.a	n.a	6
b-values (s/mm^2)	n.a	n.a	n.a	n.a	50,400,800	n.a	n.a

T_2w	T_2 weighted
DCE	Dynamic Contrast Enhanced
T_1w	T_1 weighted
TSE	Turbo Spin Echo
SEMC	Spin Echo Multi Echo
DESPOT1	Driven Equilibrium Single Pulse Observation of T_1
SSH-EPI	Single Shot Echo Planar Imaging
GRE	Gradient Recalled Echo
n.a	Not Applicable

Table 2.2 MP-MRI study acquisition parameters

2.2.3 T_2w Anatomic imaging

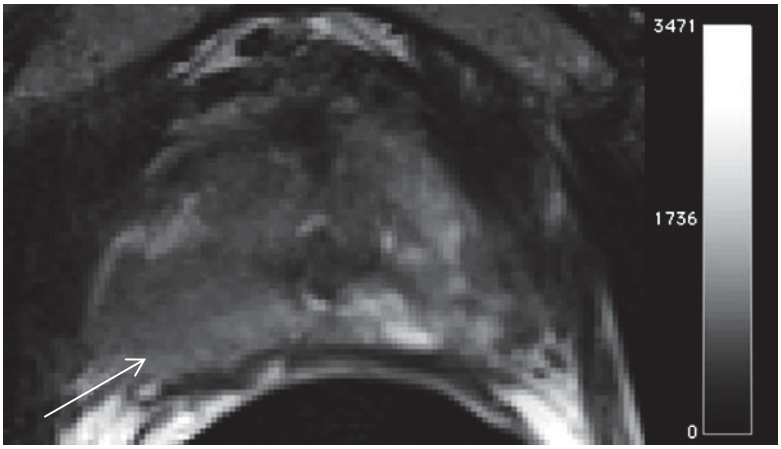

Figure 2.1 T_2-weighted image of the prostate. Hypointense region (arrow) indicates cancer. The units of the scale bar are in ms.

T_2-weighted (T_2w) MRI is the traditional method of imaging the prostate and determining the location of PCa. On T_2w sequences, in general, normal prostate PZ areas show high signal intensity owing to high water content whereas the CG areas (comprising of central and transition zones) show lower signal intensities. While PCa is frequently seen as a hypointense region in the PZ, some cancers are isointense and therefore cannot be seen on T_2w images. T2w sequences show low specificity due to the high frequency of low intensity regions due to prostatitis, atrophy and calcifications (32). Hypointense regions can also be seen with areas of hemorrhage (post-biopsy or otherwise) infection and as a result of radiation or hormonal treatment. For this reason a gap of at least six to eight weeks post-biopsy is suggested prior to performing MRI.

After confirming accurate endorectal coil placement, anatomic images were acquired using a T_2-weighted (T_2w) fast spin echo or Turbo Spin Echo (T_2-TSE) sequence in the transverse plane. The initial axial T_2-TSE acquisition was

acquired with a left-right phase encoding and no parallel imaging acceleration. In cases where the predicted specific absorption rate (SAR) was too high, the repetition time (TR) of the transverse scan was increased accordingly resulting in a nominal repetition time of 6 s. All axial images were positioned such that the slice plane passed perpendicular to the posterior surface of the prostate. Coronal and sagittal T_2w-TSE anatomic scans were acquired in orthogonal planes with respect to the transverse acquisitions with a TE of 107 ms and an acceleration factor of 2 with right-left and foot-head phase encoding directions, respectively. No SAR issues were present in these other orientations as fewer slices were acquired.

2.2.4 T_2 mapping

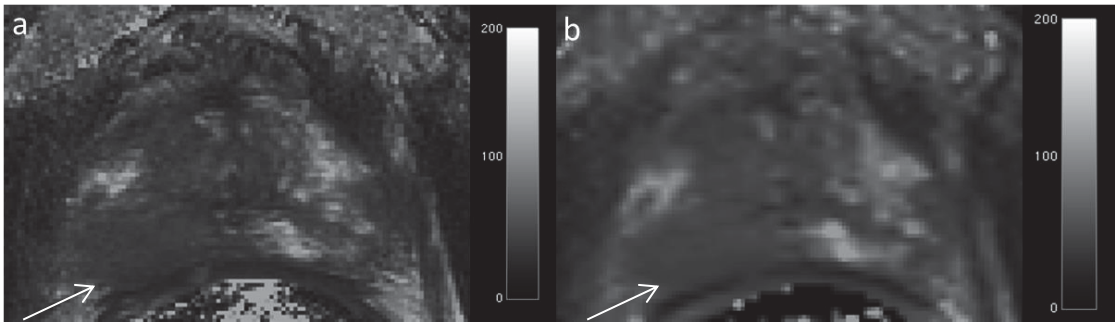

Figure 2.2 T_2-maps of the prostate using (a) T_2-TSE (Turbo Spin Echo) (b) T_2-SEMC (Spin Echo Multi Contrast) methods. Hypointense region (arrow) indicates area of cancer. The units of the scale bars are in ms.

While T_2w anatomic imaging provides the best anatomic detail of the prostate's zonal anatomy and margins, there is evidence that there may be an advantage to calculating T_2 maps (49,50). T_2 mapping provides a measure of the apparent transverse relaxation time in milliseconds (ms) on a voxel by voxel basis. Measuring relaxation times instead of relying of image intensities as in T_2w

imaging, is an ideal way to parameterize the anatomic images. The potential advantages result from the ability to use an absolute value for differentiating tissue and observing therapeutic effect. When there is little normal tissue within a given image it becomes difficult to interpret abnormal regions based solely on signal intensity. Figure 2.2 shows two ways of achieving T_2-maps of the prostate used in this research.

The first method involved acquiring additional axial TSE data sets with echo times of 30, 74 and 144 ms. To accelerate acquisitions of these additional series, parallel imaging with an acceleration factor of 2 was used resulting in a scan time of 2:28s per series. The mapping of T_2 from these data was accomplished by methods previously described and validated by Liney et al. (51) and Gibbs et al.(52). Transverse relaxation rates were calculated through a semi-logarithmic linear least squares fit to the signal intensity equation,

$$S = S_0 e^{\frac{-TE}{T_2}} \tag{2.1}$$

where S_0 represents the signal at TE=0 ms (the proton density signal) and S is the signal intensity at a given TE from the multiple TSE datasets acquired at different echo times. The function LINFIT in IDL (ITT Boulder, CO) was used to compute this value. The T_2-TSE mapping approach was chosen due to its acquisition and hence anatomical similarity to the T_2-weighted acquisition. This is especially important during the transfer of pathology registered tumor regions from the T_2-weighted image to the T_2 map. The T_2-TSE approach is also more time-efficient compared to the multiecho approach and as a result is less prone to motion artifacts.

As an alternative to the T_2 maps generated by the multiple TSE acquisitions described above, a spin echo multi-contrast (SEMC) acquisition was also obtained. In this type of sequence, the echoes of the spin echo train each contribute to a different image with varying T_2-weighting. A total of 11 echoes were acquired thus giving rise to 11 images with echo times ranging from 13.3 to

154.1 ms. The disadvantage of this acquisition compared to the multiple TSE imaging series for generating T_2 maps was a decrease in resolution and increase in scan time while the advantage was the freedom from motion artifacts between images of each echo time and the availability of more datasets for T_2 quantification. Because of the presence of more points along the T_2 decay curve, a non-linear fit using the function CURVEFIT in IDL was used. It was important to remove the image generated from the first echo of the series as this first point exhibited non-monoexponential characteristics. The signal of the first point is a pure echo whereas signals acquired at subsequent TEs are composed of primary and stimulated echoes as the refocusing pulse flip angles are not exactly 180˚ due to B_1 field inhomogeneities. This first point was not included as it would have led to an overestimation of T_2 (53).

2.2.5 T_1-weighted imaging and mapping

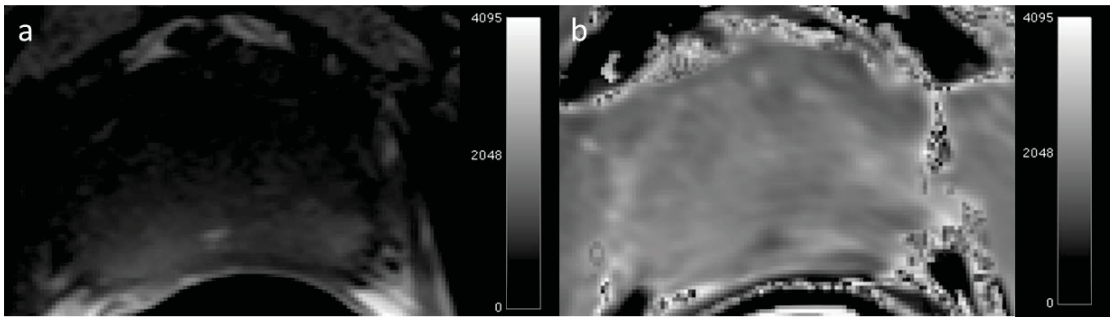

Figure 2.3 (a) T_1-weighted image and T_1 map (DESPOT1) (54) of the prostate. The units of the scale bars in are SI units (a) and ms (b).

In this work, a T_1-weighted Turbo Spin Echo (T_1-TSE) sequence was used for the qualitative assessment of post-biopsy hemorrhage. While an effective means to avoid misreading the associated T2-weighted images, the use of the qualitative T1-weighted images, especially in the presence of an uncorrected sensitivity profile of the endorectal coil, are not reliable for use in the multi-

parametric model development, therefore the generation of T1 maps was desired. T1 maps were generated using the 3D DESPOT1 (Driven Equilibrium Single Pulse Observation of T_1) method (54). The data acquired was the same used for the DCE-MRI studies detailed below but with 4 averages and varying flip angles of 2, 5 10 and 12 degrees. In DESPOT1, the T_1 is calculated by fitting the signal intensities obtained from the multiple flip angle images using the LINFIT function in IDL (ITT Boulder, CO).

2.2.6 Maps of Apparent Diffusion Coefficient (ADC)

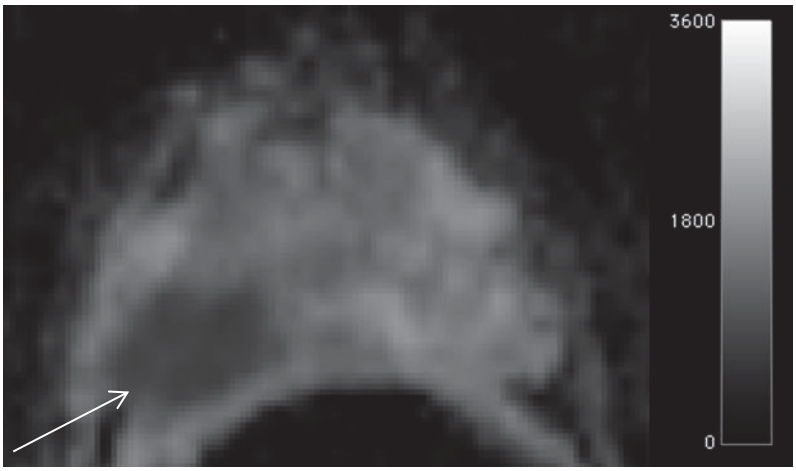

Figure 2.4 Apparent Diffusion Coefficient (ADC) map of the prostate. This image was obtained with a diffusion weights (b) of 50, 400 and 800 s/mm^2**.** Hypointense region (arrow) is indicative of restricted diffusion (cancer). Units of scale bar are in 10^{-6} mm^{2}s^{-1}.

Diffusion Weighted Imaging (DWI) sequences are useful in measuring the restriction of diffusion in biological tissues and properties such as cellular density, membrane permeability and space between cells and thus can aid in distinguishing benign from malignant tissues. They have the combined advantages of short acquisition times and low technical demand for image post-processing in comparison to DCE and MRS acquisitions. DWI images are

generally post-processed to obtain Apparent Diffusion Coefficient (ADC) maps (55) which are used to characterize the Brownian motion of water primarily from the extracellular and fluid filled compartments in tissue (56). Diffusion is more restricted in conditions of high cellular density. Tumor ADC values have been shown to be significantly lower than those found in normal prostate gland (57) due to the denser packing of cells and the loss of the normal ductal architecture in the prostate.

ADC maps were generated from single shot EPI acquisitions with different diffusion weights characterized by their b values of 50, 400 and 800 s/mm^2. These b values were chosen as there is historical precedence with the advantage of reducing the confounding effects of perfusion by avoiding b = 0 s/mm^2 (58,59) and the promise of adequate SNR by restricting the upper b-value to 800 s/mm^2. ADC was calculated by linear fitting the data using the equation,

$$S(b) = S_0 e^{-b \cdot ADC} \quad (2.2)$$

where the ADC is determined by finding the slope of the line fit to the natural log of the DWI signal intensities versus b-values. The ADC map was generated in the Siemens Trio Platform using the “3-Scan Trace” method.

2.2.7 Dynamic Contrast Enhanced (DCE) Imaging

The Dynamic Contrast Enhanced MRI (DCE-MRI) protocol involves the acquisition of images before and after the intravenous injection of the exogenous contrast agent. DCE-MRI provides information about neo-angiogenesis where cancer is typically found to have a faster uptake and higher permeability than healthy tissues (22). Angiogenesis is known to lead to varying combinations of increased blood flow, microvascular density and capillary leakiness in malignant lesions. Quantitative interpretation of DCE-MRI data, involves first converting the acquired dynamic signal intensity curves obtained during the typical dynamic acquisition into the gadolinium concentration curves. This method of assessing

microvascular changes in tumors employs pharmacokinetic models to determine the rate of exchange of contrast between plasma and the extravascular, extracellular space and allows specific quantitative vascular parameters, such as K^{trans}, K_{ep}, V_e and AUGC can be estimated.

K^{trans} (transfer constant) describes the diffusion of contrast agent from the intravascular space to the extravascular (interstitial) space and depends on the flow rate per unit volume, the permeability and the surface area of the tissue capillaries. This can be characterized by the wash-in of contrast to the tissue. K_{ep} (rate constant) represents the leakage of contrast from the extravascular space to the blood plasma. V_e is an estimate of the extravascular extracellular volume also referred as the EES or interstitial space. AUGC stands for the Area Under the Gadolinium concentration curve (22). All of these parameters have been shown to be elevated in tumors. This quantitative approach has also been proposed to be more reproducible, enabling serial measurements of perfusion parameters over time to facilitate evaluation of treatment response (60). Figure 2.5 shows the DCE-MRI maps for a prostate with tumor in right peripheral zone.

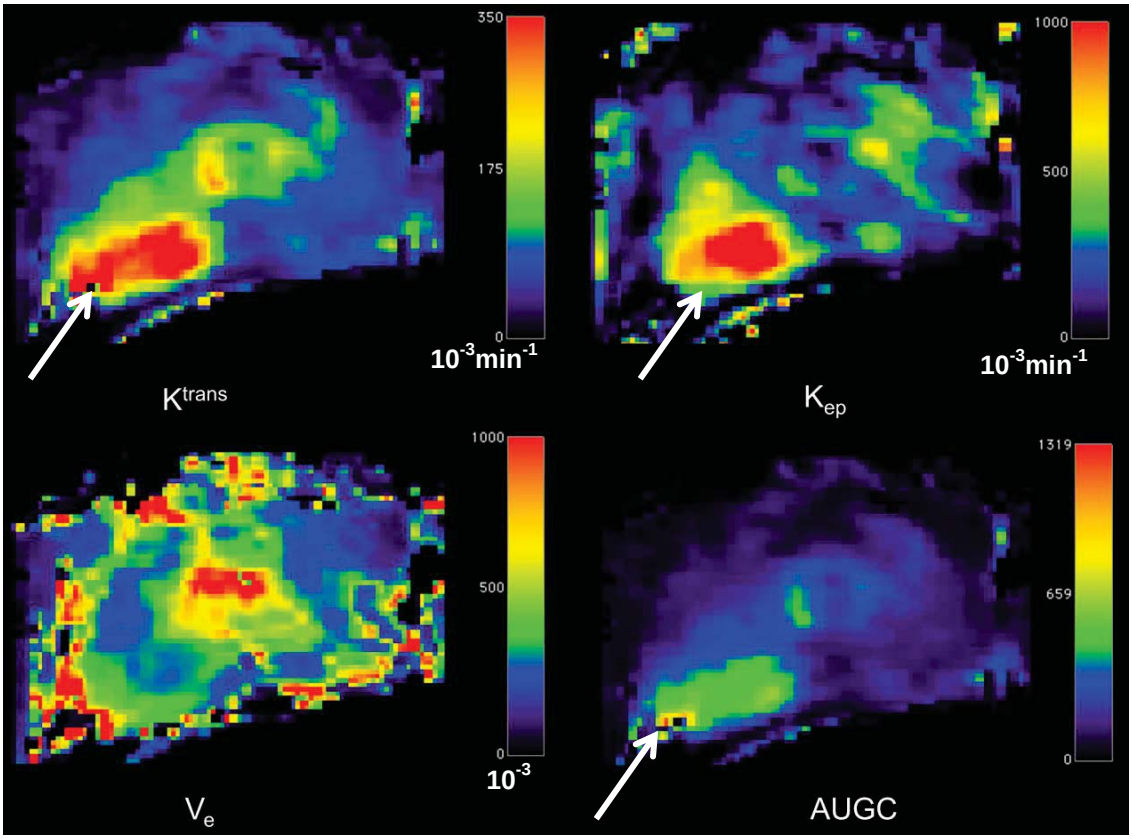

Figure 2.5 DCE-MRI maps of the prostate. Units of the scale bar are $10^{-3} \times min^{-1}$ (K^{trans}), $10^{-3} \times min^{-1}$(K_{ep}) and 10^{-3} (V_e). Increased K^{trans} (wash-in), K_{ep} (wash-out) and AUGC (Area Under Gadolinium Concentration Curve) identifies area of cancer in these maps.

The DCE-MRI data were acquired with a 3D T_1-weighted gradient echo acquisition (i.e. 3D VIBE - Volume Interpolated Breathold Examination in the manufacturers' lexicon). This sequence is referred to as T1w3D-GRE in Table 2.2. In summary, the acquisition has a temporal resolution of 6 s and spatial resolution of 1x1x4 mm^3. A total of 50 dynamics were acquired for a total acquisition time of 5 min. In the case that the calculated power deposition was too high for the acquisition, a slightly lower flip angle was prescribed until the sequence could run. Pharmacokinetic maps were generated by using a modified Tofts model (61) with a population averaged arterial input function (AIF) (62). The

fitted model provided the following pharmacokinetic parameters: K^{trans} (Forward Volume Transfer Constant, min^{-1}), K_{ep} (Reflux Rate between the Extracellular Space and the Plasma, min^{-1}), V_e (Fractional Extravascular Extracellular Space, $V_e = K^{trans}/K_{ep}$) and AUGC (Area Under Gadolinium Curve). All analyses were carried out in IDL (ITT Boulder, CO) (63-65).

2.3 Histopathology

2.3.1 Surgical to Pathology Workflow

After removal from the patient, the prostate is fixed with formalin and then gross sectioned to match, as close as possible, the MR imaging planes. For this purpose, a special sectioning box (Figure 2.6) was constructed and a sectioning protocol established (Figure 2.7 a, b). After amputation of the seminal vesicles and vasa deferentia at the base and shaving off 1mm of the proximal urethral margin, the prostate was placed in the sectioning box so that the posterior surface of the prostate was approximately parallel to the bottom and the long axis of the box. Vertical slits in the box, 3 mm apart, allowed the consistent parallel sections to be cut perpendicular to the posterior surface of the prostate with a thickness of 3 mm to match the orientation and thickness of the axial MRI slices.

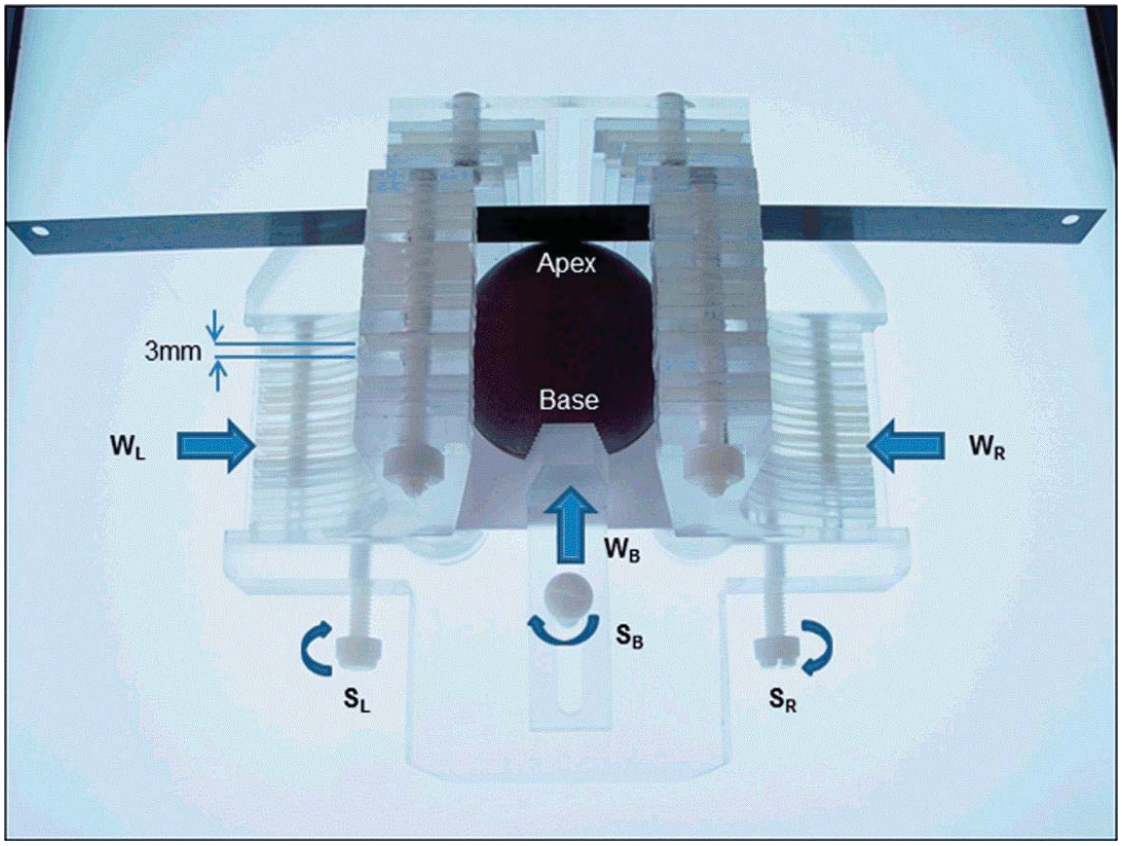

Figure 2.6 Prostate sectioning box made of Acrylic and Teflon**.** The box is shown with a spherical prostate model and the movable walls on the left (WL) right (WR) and base (WB) are pushed in to hold the model securely. Each moveable wall is held in place with a locking screws SL, SR and SB, respectively. A standard pathology blade is inserted through the milled slits in the acrylic pieces that make up the left and right walls. Each successive axial cut through the prostate requires passing through the next slit in the side walls. The tolerance is such that the blade can only traverse through the corresponding slit on the opposite side.

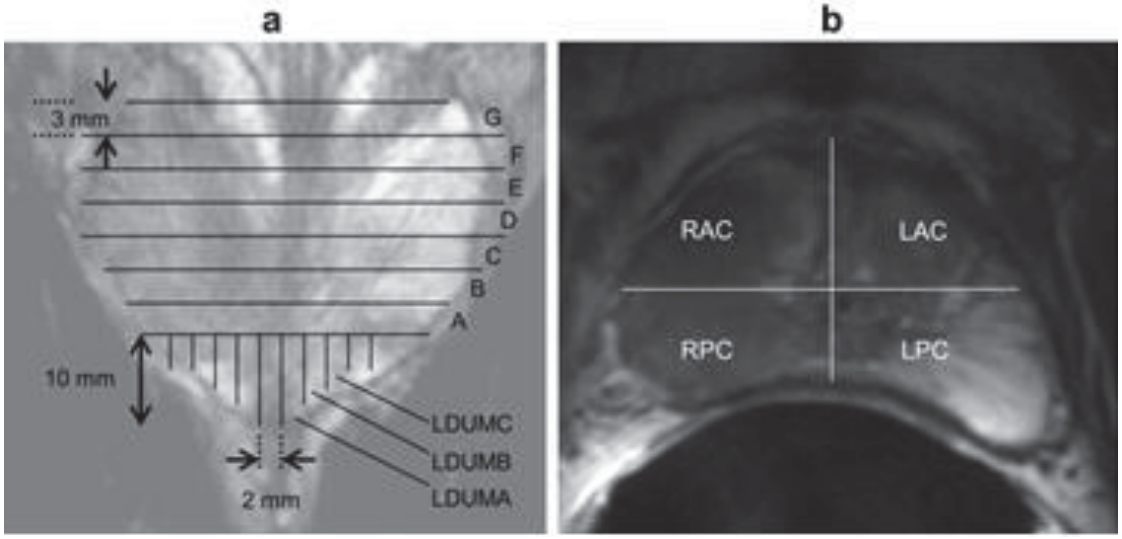

Figure 2.7 Diagrams of pathologic sectioning protocol overlaid on a coronal (a) and axial (b) T_2w image. After placing the prostate in the sectioning box, the first cut made is approximately 0.6 mm from the apex of the gland to create the apical section, with successive axial cuts 3mm apart moving towards the base. The axial cross-sections are designated by letters “A”, “B”, “C”, etc., depending on the size of the prostate, with “A” being the most apical slice. Slices are divided into four quarters (b). Each quarter is labeled based on the letter of the slice from which it comes and its position in the slice (e.g. anterior/posterior = A/P and right/left = R/L). After removal from the box, the apical portion is sectioned in 2mm intervals with parallel cuts emanating from the urethra. The sections near the urethra are labeled “RDUMA” (right distal urethral margin A) and “LDUMA” (left distal urethral margin A). The next two sections from the center are then labeled “RDUMB” and “LDUMB”, etc. This process continues out to the lateral margins of the apical section. Each slice section is then embedded in a paraffin block and one 4-micrometer H&E-stained slide is prepared from each section and digitized. A pathologist then digitally annotates the prostate capsule (red contour) and cancer regions (brown contour) on each slide.

2.3.2 Digitization

Gross sectioned prostates were subjected to quarter mount histological section (QMHS) pathologic processing. Sections were paraffin embedded, Hematoxylin

and Eosin (H&E) stained, and cut at 4 μm thickness. H&E stained slides were digitized using a whole slide scanner (ScanScope CS, Aperio, Vista, CA).

2.3.3 Annotation

The prostate pseudo-capsule and tumor regions within the digitized sections were annotated by a board certified pathologist with 15 years' experience, at 20X magnification (resolution 0.58μm per pixel) using a pen tablet screen (Cintiq 21UX, Wacom, Kazo-shi, Saitama, Japan).

2.3.4 Data Assembly

Digitally annotated QMHS slides were then manually assembled into PWM by aligning the capsule annotations of the quartered pathology sections to form a continuous capsule while minimizing overlap of tissues between the combined sections. Anatomic features in the pathology sections being assembled also aided in aligning the QMHS images (Figure 2.8 a, b).

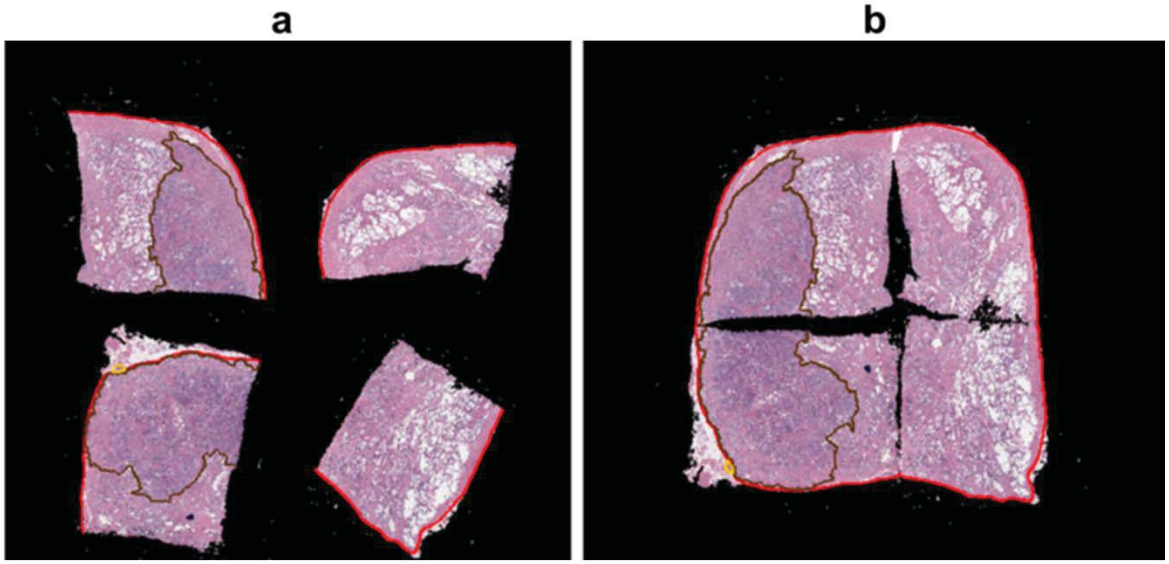

Figure 2.8 (a) Slides from a complete axial slice are then manually assembled into a PWM by aligning the capsule annotations of the quartered pathology sections to form a continuous capsule while minimizing the overlap of tissues between the combined sections (b).

Chapter 3 LATIS Registration

This chapter is adapted with permission from the following publication: Kalavagunta, C., Zhou, X., Schmechel, S. C. and Metzger, G. J. (2014), *Registration of in vivo prostate MRI and pseudo-whole mount histology using Local Affine Transformations guided by Internal Structures (LATIS)*. J. Magn. Reson. Imaging. doi: 10.1002/jmri.24629

This was a collaborative project between Dr Greg Metzger, Dr. Xiangmin Zhou, Dr. Stephen Schmechel and me. My primary role in this project was the development of the Matlab software tools to obtain the necessary inputs for the registration process, perform the registration procedures, visualize the results, validate registration performance and enable the application of all registration results to pathologist annotated cancer regions. Implementation of these procedures and validation was a critical component of the MP-MRI model generation process discussed in Chapter 4.

3.1 Synopsis

A novel registration approach called LATIS (Local Affine Transformation assisted by Internal Structures) for co-registering post prostatectomy pseudo-whole mount (PWM) pathological sections with in vivo MRI (Magnetic Resonance Imaging) images is presented. This study included thirty-five patients with biopsy-proven PCa that were imaged at 3T with an endorectal coil. Excised prostate specimens underwent quarter mount step-section pathologic processing, digitization, annotation and assembly into a PWM. Manually annotated macro-structures on both pathology and MRI were used to assist registration using a relaxed local affine transformation approximation. Registration accuracy was assessed by calculation of the dice similarity coefficient (DSC) between transformed and target capsule masks and least square distance between transformed and target landmark positions. LATIS registration resulted in a DSC value of 0.991±0.004 and registration accuracy of 1.54±0.64 mm based on identified landmarks common to both datasets. Image registration performed without the use of internal structures led to an 87% increase in landmark based registration error. Derived transformation matrices were used to map regions of pathologically defined disease to MRI.LATIS was used to successfully co-register digital pathology with in vivo MRI to facilitate improved correlative studies between pathologically identified features of PCa and MP-MRI.

3.2 Introduction

Multi-parametric maps of anatomic, vascular and metabolic data of the prostate acquired using MP-MRI can yield improved discrimination of the extent and aggressiveness of PCa (66-68). An important step in developing and validating MP-MRI biomarkers to detect the extent and aggressiveness of PCa is the registration of *in vivo* MR images with histopathological sections obtained from

prostatectomy. This multi-modal registration would enable correlation of MRI with postoperative histopathological determination of extent and tumor grade, and ultimately the molecular assessment of aggressiveness.

There has been much interest in the multi-modal co-registration of prostate MRI with other imaging modalities such as CT for treatment planning (69-72), ultrasound for guiding biopsies (73), and pathology for validation of cancer detection (74). With each combination of source and target data come unique challenges for the registration procedure. In this work, the goal was to register *in vivo* MRI data obtained with a balloon-type endorectal coil (ERCinMR) with images of *pseudo*-whole mounts (PWM) constructed from quarter mount histologic sections.

The prostate images from *in vivo* MRI and pathology possess different amounts of deformation/distortion with respect to each other. For example, after digitally assembling quarter mount histological sections into a PWM, the resulting PWM is different from a true whole mount image in multiple ways, including: (a) the boundary shape of the prostate, (b) the unfilled space or gaps between the quarter mount histological sections, and (c) deformation/distortion of each individual quarter. Additionally, the difference between the ERCinMR and the tissue observed on pathology is a result of multiple factors, including: (a) physical distortion of the prostate due to the presence of the inflated endorectal coil, (b) deformation of the tissue after excision and (c) shrinking of the tissue due to fixation. Without completely characterizing all the intermediate deformations, the registration procedure described in this work focuses on directly registering ERCinMR with PWM images due to the fact that both data sets are readily available, and characterization of the intermediate deformations are not easily obtainable.

LATIS is a technique that uses a relaxed Local Affine Transformation approximation assisted by the identification of large Internal Structures. In LATIS, the prostate capsule and large internal anatomic structures are used as

constraints for registration. This technique does not require the accurate definition of a set of multiple paired landmarks between the source and target data which are difficult to obtain in general and the basis for leading registration methods tackling similar problems. The large structures are, arguably, easier to manually identify on both pathology and MRI and provide a larger continuum of spatial information to guide the registration procedure. In this study, the ability of LATIS to co-register PWM and ERCinMR images is evaluated, and the use of this registration to map regions of pathologically identified cancer onto the *in vivo* MRI is demonstrated.

3.3 Methods

Data used in this study was obtained from patients with biopsy-proven prostate cancer (35 men, age range 50-73 years, mean age 62 years) after obtaining written signed consent for a study reviewed and approved by the local Institutional Review Board.

3.3.1 In Vivo MR Data

In vivo MR data was obtained from the T_2-weighted (T_2w) axial MR images. The axial images were positioned such that the slice plane passed perpendicular to the posterior surface of the prostate (See Chapter 2 Sections 2.2.1 to 2.2.3).

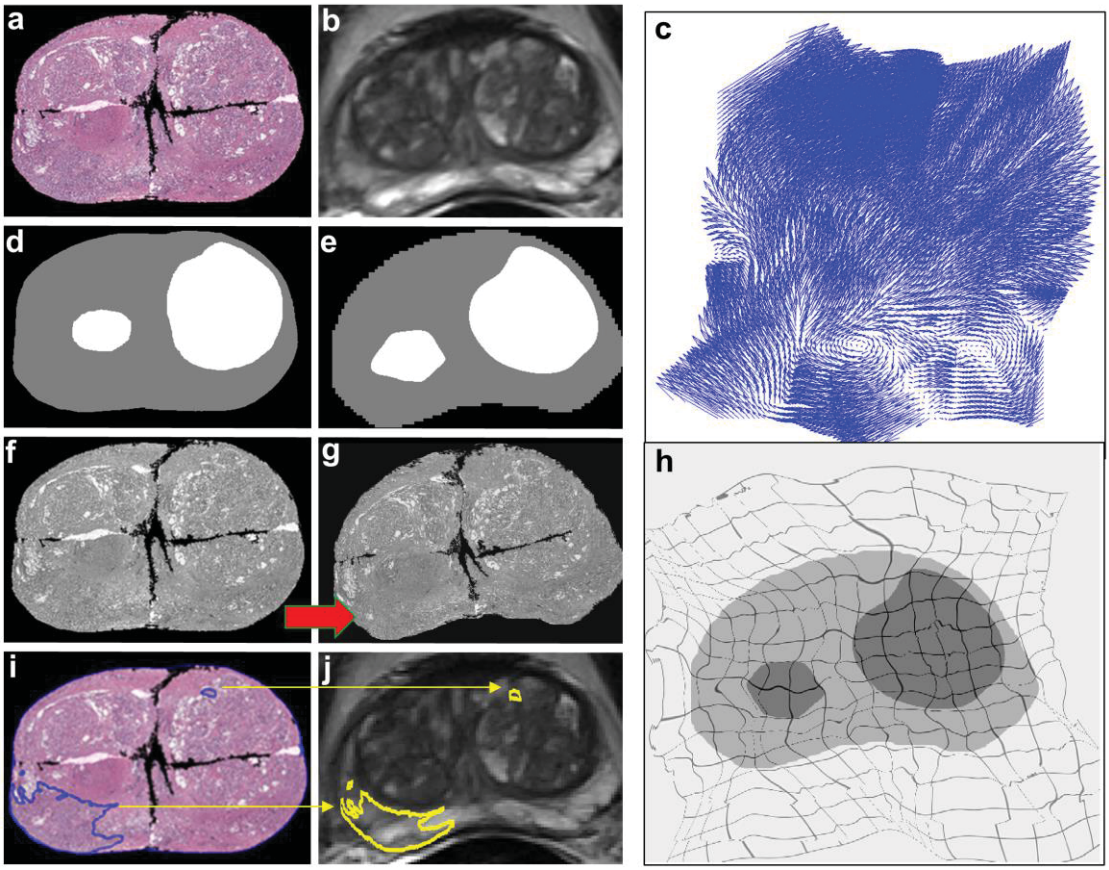

Figure 3.1 A schematic demonstrating the procedure to co-register pathology to T_2w MRI using LATIS. First, the source (a) and target (b) images are segmented, scaled and translated. Second, the prostate capsule and internal structure masks are identified to constrain the pathology transformation. The source and target masks (d and e) are registered and a transformation matrix is obtained. Images (c) and (d) show the transformation flow matrix and applied deformation field respectively. Third, the transformation matrix is applied (red arrow) to the pathology (f) which places it in spatial correspondence to the T_2w MRI resulting in (g).Lastly, applying the transformation matrix to each one of the annotated cancer regions (i) places them in the spatial framework of the anatomic T_2w images (j).

3.3.2 Pathology Data

Excised prostates were formalin fixed, gross sectioned, paraffin embedded, cut at 3 μm, H&E stained, digitized, annotated by an experienced pathologist and assembled into a PWM. The sectioning protocol is shown in Figure 2.7 a and b.

based on a special sectioning box (Figure 2.6). Vertical slits in the box, 3 mm apart, allowed the consistent parallel sections to be cut perpendicular to the posterior surface of the prostate with a thickness of 3 mm to match the orientation and thickness of the axial ERCinMR slices. Positioning both the imaging and sectioning planes perpendicular to the posterior surface of the prostate was the method we used to get slices which matched as closely as possible. From the assembled PWM, binary masks of both annotated tumor regions and the prostate capsule were generated (Figure 3.1). For each patient, a single PWM at the center of the index lesion was chosen for registration (Chapter 2 Section 2.3).

3.3.3 Image Registration

In order to register the PWM (source image) to the ERCinMR (target image) (Figure 3.1), a transformation that can map the source image to the target image must be found. Since the source and target image belong to two completely different imaging modalities, a direct mapping relationship between these two images cannot be readily established without additional inputs or modifications. The first step in the process involved manually converting the source and target into tri-intensity grayscale images (Figure 3.1) such that the internal structures had a grayscale value of 128 and the rest of the prostate has a value of 255. This created the potential for developing a direct mapping between the two datasets. To register the two tri-intensity grayscale images, some assumptions are introduced:

1. The 2-dimensional source and target images correspond to the same cross-section of the prostate in terms of the position and the outward normal direction.

2. There exists a path-independent, unique mapping between the source and the target image.
3. The image intensity between the source and target image is conserved.

These three assumptions are reasonable and can be easily satisfied in most cases. The first assumption is met by the standard data collection and sectioning protocols employed in this study. This condition is of the upmost importance because, as the source and target images diverge in terms of their spatial correspondence, there is decreasing benefit to perform the registration since the cancer region annotated in the source image cannot be guaranteed to exist in the target image.

The second assumption establishes that the problem is well-posed. Supposing assumption No.1 holds, there exists a mapping relation between the source and target images as they both represent different realizations of the same cross-section of the prostate. Employing a linear approximation for the mapping will guarantee a unique and path-independent solution. The existence of a solution and its uniqueness establish that the problem is well-posed (75), hence the solution is guaranteed.

The third assumption forms the basis for the image registration procedure. With assumption No. 1, both the source and the target images are referring to the same cross-section of the prostate but differ due to in-plane deformation. After converting the source and target images to the tri-grayscale-images, the intensity conservation principle (76) is readily applicable and a relationship can be established between the source and target images. With this established relationship, the mapping relation between the source and target image can subsequently be derived with the help of assumption No. 2. The derivation is shown in next section. In summary, although three assumptions were introduced, assumption No. 1 is the most fundamental. If assumption No. 1 is achievable,

assumptions No. 2 and 3 are imposed, both of which serve as a foundation for the following registration derivation.

3.3.4 Theory

Let *I(x, y, t)* be the intensity of an image, which is a function of space and time. When the source and the target tri-grayscale-images are treated as the images of a deforming prostate at two different time points, time is involved. Therefore, one can assign the source image at t_1 and assign the target image at t_2. Following assumption No.1, assumption No. 3 imposes the intensity conservation principle which implies that the total derivative of the intensity is invariant, i.e.

$$\frac{dI(x,y,t)}{dt} = 0. \tag{3.1}$$

Expanding the left hand side (LHS) of the equation, it becomes

$$\begin{aligned}\frac{dI(x,y.t)}{dt} &= \frac{\partial I(x,y,t)}{\partial x}\frac{dx}{dt} + \frac{\partial I(x,y,t)}{\partial y}\frac{dy}{dt} + \frac{\partial I(x,y,t)}{\partial t} \\ &= I_{,x}x' + I_{,y}y' + I_{,t} = 0\,.\end{aligned} \tag{3.2}$$

According to assumption No. 2, there exists a transformation such that the above equation (3.2) is satisfied. Since this exact transformation is unknown, the assumption of a local affine transformation is made between the source and target image, which is,

$$\begin{bmatrix}\tilde{x}\\ \tilde{y}\\ 1\end{bmatrix} = \begin{bmatrix}\cos\theta & \sin\theta & L_x\\ -\sin\theta & \cos\theta & L_y\\ 0 & 0 & 1\end{bmatrix}\begin{bmatrix}x\\ y\\ 1\end{bmatrix} \tag{3.3}$$

where (x, y) represents the source image at t_1, $(\tilde{x}, \tilde{y})$ represents the target image at t_2, (L_x, L_y) is the translation, and θ is the rotational angle. And since the local

affine transformation is a proposed approximation, a more relaxed linear approximation can be adopted, namely,

$$\begin{bmatrix}\tilde{x}\\ \tilde{y}\\ 1\end{bmatrix} = \begin{bmatrix}a_1 & a_2 & a_3\\ a_4 & a_5 & a_6\\ 0 & 0 & 1\end{bmatrix}\begin{bmatrix}x\\ y\\ 1\end{bmatrix} \tag{3.4}$$

which relaxes the θ constraint between the transformation parameters $\{a_1, a_2, a_4, a_5, a_6\}$. This linear approximation satisfies assumption No. 2. With respect to the approximation, there is no qualitative difference between equation (3.3) and equation (3.1) since they are both linear functions but, as shown in a later part of this section, it is desirable to select equation (3.1) over equation (3.3) to reduce the correlation between the transformation parameters resulting in a simpler solution procedure. Substituting equation (3.1) into equation (3.2) leads to the LHS not being equal to zero because equation (3.1) is an approximation and an approximations result in errors. Therefore, locally, we have an error function in terms of $(\tilde{x}, \tilde{y})$ where $\tilde{I}_x$, $\tilde{I}_y$, and $\tilde{I}_t$ are functions of $(\tilde{x}, \tilde{y})$, which states that

$$e(a_1, a_2, a_3, a_4, a_5, a_6) = \tilde{I}_x\tilde{x}' + \tilde{I}_y\tilde{y}' + \tilde{I}_t \tag{3.5}$$

Now the objective of the registration process is to find a set of transformation parameters $\vec{a} = (a_1, a_2, a_3, a_4, a_5, a_6)^T$ such that error function *e* is equal to or is minimal with respect to zero. In order to seek the solution for the transformation parameters, a quadric error functional is constructed as

$$\Pi = \frac{1}{2}e^T e. \tag{3.6}$$

Further taking the variation of the quadratic functional, yields,

$$\delta\Pi = \frac{\partial \Pi}{\partial \vec{a}}\delta\vec{a} + \frac{\partial \Pi}{\partial \vec{a}_i}\delta\vec{a}_i + \cdots higher\ order\ terms \tag{3.7}$$

Since the transformation parameters are constants, the higher order terms vanish after taking the first variation of the quadratic functional, i.e. $\vec{a}_i = 0$, for all i > 1. And according to the Ekeland's variational principle (77), there exist a solution for $\vec{a}$ such that $\delta\Pi = 0$ which corresponding to the minimization of the error function e. Since $\delta\vec{a}$ is arbitrary and is not always equal to zero, the only possibility to yield $\delta\Pi = 0$ is that the following equation is always satisfied,

$$\vec{0} = \frac{\partial \Pi}{\partial \vec{a}} = \frac{\partial e^T}{\partial \vec{a}} e = \vec{c}(\vec{c}^T\vec{a} - f)(\vec{c}^T\vec{a} - f) \tag{3.8}$$

Where

$$\vec{c}^T = \begin{pmatrix} \tilde{x}\tilde{I}_x & \tilde{y}\tilde{I}_x & \tilde{I}_x & \tilde{x}\tilde{I}_y & \tilde{y}\tilde{I}_y & \tilde{I}_y \end{pmatrix} \tag{3.9}$$

$$f = \tilde{x}\tilde{I}_x + \tilde{y}\tilde{I}_y + \tilde{I}_t \tag{3.10}$$

Therefore, the transformation parameters can be solved from the following equation

$$\vec{c}\vec{c}^T\vec{a} = \vec{c}f, \tag{3.11}$$

where the resulting transformation parameters are the optimal solution satisfying equation (3.2) and subsequently, provides the transformation satisfying equation (3.1).

A pixel by pixel solution of the transformation parameters is computationally expensive and may be ill-posed in the sense of Hadamard(75). For reducing the computational cost, the transformation parameters can be solved weakly, i.e., for a neighborhood of *n* by *n* pixels,

$$\left(\sum_{\substack{i=1\\j=1\\(x,y)\epsilon\Omega}}^{n} \vec{c}\vec{c}^{T}\right)\left(\sum_{\substack{i=1\\j=1\\(x,y)\epsilon\Omega}}^{n} \vec{c}\vec{c}^{T}\right)\vec{a} = \left(\sum_{\substack{i=1\\j=1\\(x,y)\epsilon\Omega}}^{n} \vec{c}f\right) \tag{3.12}$$

where Ω represents the domain of the image and *i* and *j* are referring to the index of the pixels in the *x* and *y* directions, respectively. The image is broken up into a grid of these neighborhoods such that the larger the neighborhood, the coarser the grid. However, due to the properties of the tri-intensity grayscale images, equation (3.12) is ill-posed (non-invertible). This is because for the entire neighborhood of *n* by *n* pixels located within the same intensity grayscale region, we have

$$\tilde{I}_x = \tilde{I}_y = \tilde{I}_t = 0 \tag{3.13}$$

and,

$$\vec{c}\vec{c}^{T} = \vec{c} \otimes \vec{c} = 0 \tag{3.14}$$

In order to achieve a solution for equation (3.12), the matrix of the left hand side needs to be diagonally dominant. Thus, the following modifications can be made in equation (3.11) to add a diagonal matrix on both the left hand side and right hand side:

$$(\vec{c}\otimes\vec{c}+\eta)\vec{a}=\vec{f}+\eta\vec{a} \tag{3.15}$$

where η is a diagonal constant matrix with a reasonably large positive number for the diagonal elements and zeroes for the off-diagonals. Based on our experience, a $\eta_{kk}=10^{10}$ is chosen. Since the same quantities are added equally on both side of the equation, it does not change or affect the solution of the original equation but makes it always solvable. Thus equation (3.11) becomes

$$\vec{a}=(\vec{c}\otimes\vec{c}+\eta)^{-1}(\vec{f}+\eta\vec{a}) \tag{3.16}$$

The fixed-point iteration method can now be readily employed for solving equation (3.16). Employing the fixed-point iteration method (49), $\vec{a}$ can be solved iteratively from

$$\vec{a}^{(m+1)}=(\vec{c}\otimes\vec{c}+\eta)^{-1}(\vec{f}+\eta\vec{a}^{(m)}) \tag{3.17}$$

with an initial guess of $\vec{a}^{(0)}=0$ when m=0 for the initial step. `

3.3.5 Multi-Resolution Optimization

Two principle causes of potentially large deformations in local regions of the prostate between the PWM and ERCinMR images result from the sectioning and reassembly of the pathology specimens and the use of an ERC. The optimal neighborhood size, n x n, over which $\vec{a}$ needs to be solved is unknown. For neighborhoods too large, the accuracy of the registration would be insufficient, and for neighborhoods to small, the registration method would be ill-posed in the

sense of Hadamard (75). Therefore, instead of choosing a fixed neighborhood size, a multi-resolution optimization strategy is employed.

The idea behind the method of multi-resolution optimization for registration is that the starting grid of neighborhoods covering the image is small (low resolution) while as the optimization progresses the resolution of the grid increases (i.e. decreasing neighborhood size). The solution in each step in the progression of the grid refinement provides an improved initial guess for the subsequent higher resolution grid. In the course of registering PWM to the ERCinMR image, a sequence of 2^n grids are used, where n is equal to 0, 1, 2 ... etc. The final transformation is the accumulated transformation of the multiple steps with the criteria to stop the refinement of the grid mesh being when the L_2-norm of the displacement between step n and step n+1 is less than 0.1 pixels.

3.3.6 Registration Procedure

The image registration workflow for a sample case is shown in the Figure 3.1. After choosing the assembled pathology PWM slice, the corresponding target T_2w ERCinMR slice was identified by choosing a slice at the same approximate position from the apex and verifying the existence of similar anatomic features. The source (PWM) is shown in Figure 3.1.1a. The target (ERCinMR, T_2w) is shown in Figure 3.1.1b. The prostate region in the ERCinMR image was extracted masking with capsule contours drawn in a semi-automated segmentation program (Segasist, Ontario, Canada) by an experienced prostate MRI researcher (GJM). The PWM images were also masked by the combined capsule annotations defined by the study pathologist (SCS). The masked ERCinMR image was upsampled to 512×512, to match the matrix size of the PWM, and translated to achieve a greater than 50% overlap with the masked PWM. New annotation regions defining the easily identifiable large internal

structures for the PWM data were generated while simultaneously annotating similar structures on the ERCinMR. These internal structures were defined by a number of identifiable features including the central gland-peripheral zone boundary, transition zone, apex-semicircular sphincter and bilateral nodules of benign prostatic hypertrophy. These images were converted into tri-intensity (White = 255, Black = 0, Gray = 128) grayscale source and target images (Figures 3.2a and 3.2b) where the white regions delineate the internal structures. Using the pre-defined controls (large internal structures and prostate boundary) found in the source and target, LATIS was used to register the two images. The local affine transformation component of the registration procedure was adapted from methods originally published by Periaswamy and Farid (78-80). The application of the final transformation matrix to the masked grayscale PWM image (Figure 3.1.3a) and the resulting warped source image (Figure 3.1.3b) is shown. The application of the final transformation matrix warping the tumor region masks from the PWM to the ERCinMR can be seen in Figures 3.1.4 a and b. Other than where specifically stated, the registration steps and the visualization of results were performed in Matlab (MathWorks, MA, USA) running on a Windows 2.80 GHz Intel i5 CPU machine with 12 GB RAM.

3.3.7 Analysis

Two metrics were used to evaluate the accuracy of the registration methods. The first method was the Dice similarity coefficient (DSC) which measures the overlap between the target and registered source. The DSC for two images A and B is defined as the intersection of the two images divided by the mean sum of the images

$$\text{Dice Similarity Coefficient} = \frac{2 \times |A \cap B|}{|A| + |B|} \quad (3.18)$$

The second validation method involved identifying identical landmarks by visual inspection on both the native PWM and ERCinMR images. The process of identifying landmarks was independently performed by two experienced prostate researchers with four (CK) and eleven years (GJM) experience. The landmarks selected were also done so independently from the large internal structures used for registration. Landmark positions on the PWM were masked using circular ROIs (radius, 8 pixels, pixel size = 0.54 mm) to give a feature marked PWM (fmPWM) image. A circular area of this magnitude was chosen to easily identify the feature in the downscaled registered source. The transformation matrix, obtained earlier for this case, was applied to the fmPWM image and transformed pixel positions were obtained from the registered fmPWM image. Target registration error (TRE) in mm was calculated using the root mean squared distance between the transformed pixel positions from the fmPWM and the target pixel position on the ERCinMR. For the thirty five cases, landmarks for the registration accuracy calculation were drawn and a total of 103 such landmarks were identified by the two observers for error analysis. To ascertain the impact of the internal structures as a guide for image registration, these thirty five cases were again registered *without* using internal structures and the registration accuracy assessed. The source and target images in this case were the masked PWM and ERCinMR capsule masks.

3.3.8 Statistical Analysis

The average TRE and DSC are reported as the mean ± standard deviation and were calculated using Matlab (MathWorks, MA, USA). A p-value <0.005 was

considered statistically significant when evaluating the difference in registration accuracy with and without the use of internal structures. The p-value analysis was performed in OriginLab 9.0 (Origin Lab Corporation, USA).

3.4 Results

Five representative cases are provided in Figure 3.2. The assembled PWM images are shown with the annotated tumor regions and cropped to the capsule borders by using the combined capsule annotations created by the study pathologist. LATIS was used to register the PWM data to the ERCinMR. The transformation was then used to warp all annotated cancer regions from the assembled pathology to MRI (Figure 3.2 Column b). The registration calculation per case took on the order of 11 minutes.

The mean DSC after registration was 0.991±0.004 which represents nearly total correspondence by this metric after registration. The mean, minimum, maximum and standard deviation of the registration error based on the landmark method are given in Table 3.1. The average overall registration error was 1.54±0.64 mm when using internal structures and 2.92±1.76 mm without internal structures, a statistically significant increase in registration error of 87% in the absence of additional information to guide registration ($p < 0.0001$). An example of the landmark registration accuracy assessment is shown in Figure 3.3.

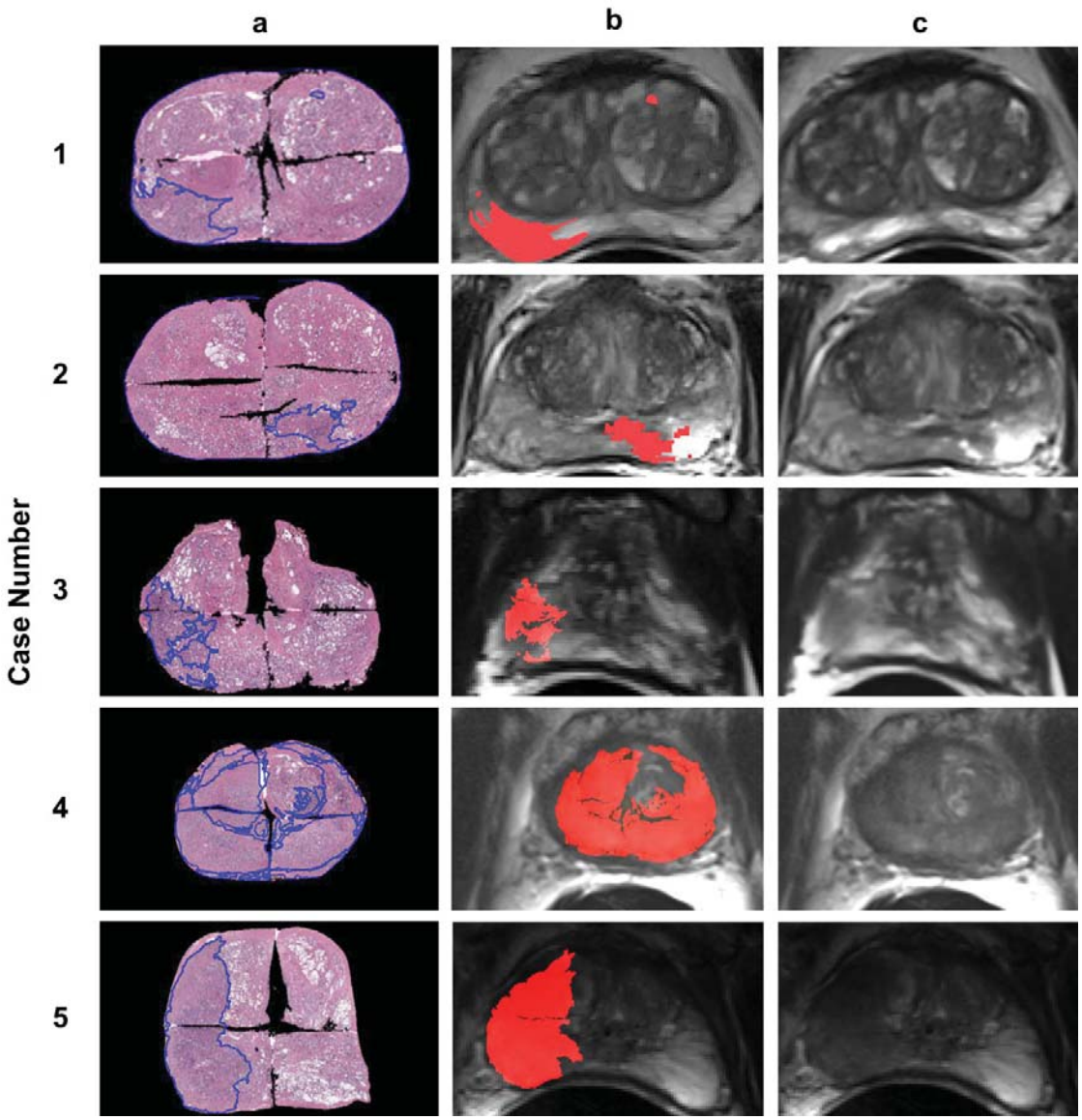

Figure 3.2 Registration results. Column ‘a’ shows the masked PWM with annotated tumor regions. Column ‘b’ shows the registered tumor regions overlaid on the ERCinMR. Column ‘c’ shows the original ERCinMR.

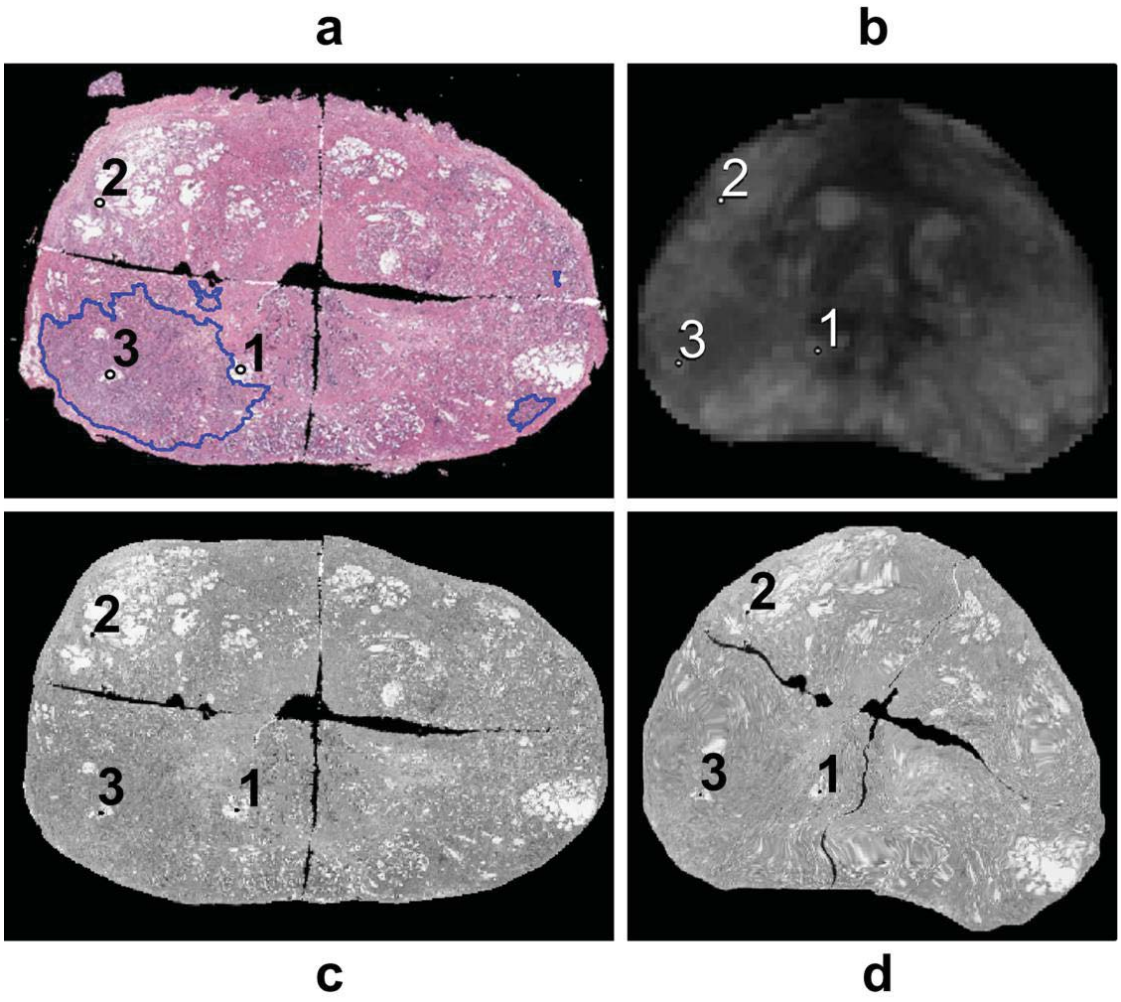

Figure 3.3 Registration accuracy metric calculation workflow - (a) Feature marked masked PWM. (b) Corresponding features on ERCinMR. (c) Warped feature embedded masked PWM. (d) Feature embedded masked ERCinMR.

	Avg(Min,Max) (mm)	SD (mm)	# Points
Total	1.54(0.19,3.26)	0.64	103
Observer1	1.57(0.43,2.92)	0.65	36
Observer 2	1.51(0.19,3.26)	0.64	67

Table 3.1 Multi–user registration accuracy metric statistics

3.5 Discussion

A registration approach using a relaxed local affine transformation approximation, assisted by large internal structures as constraints to improve registration accuracy, has been presented for co-registering post prostatectomy *pseudo*-whole mount pathological sections with T_2-weighted *in vivo* MRI images obtained with an ERC. In this study, slides made from quarter mount histologic sections were used to generate the PWM images as the ability to section, store and digitize whole mount data does not exist at our institution. Many institutions find themselves with similar limitations in terms of processing the excised prostate, therefore the methods presented here are very relevant for MRI studies wanting to use correlative pathology for identifying and validating MRI biomarkers for prostate cancer detection and grading.

3.5.1 Registration Methods

The registration between prostate histopathology and MRI images belongs to the category of multi-modal registration. Previous work in this area has investigated registering whole mount pathology (WM) to *in vivo* MRI (*in*MR) acquired without an ERC (74), *in vivo* MRI acquired with an ERC (ERCinMR) (81-86) and *ex vivo*

MRI (*ex*MR, paraformaldehyde fixed prostatectomy specimen) (86-88). While less prevalent in the literature, registration with PWM pathology has also been performed with *ex*MR (81,89-91), *in*MR acquired without an ERC and *in*MR (85) acquired with an ERC (92).

Two dominant approaches exist in published literature addressing the registration of pathology to MRI; the thin plate spline (TPS)-based (74,81,83-86,89,90,93) and B-spline (BSp)-based (87,94,95) methods. The TPS approach utilizes pre-defined control point pairs identified from different images to warp the source image to the target image using a multidimensional interpolation method (93). The result of the TPS-based methods is highly dependent on the manual selection of the control point pairs, which requires knowledge of the control point locations and distributions in both images. Such information may not be readily available in all the cases within the ERCinMR *and* PWM images. Also, since each pair of control points in the TPS method influences the entire image, this method assumes continuous source and target images, smooth deformation and distribution of control points over the entire image. Such assumptions are not valid for the PWM images used in this study.

In contrast to the TPS-based approach, the influence of the control points for the BSp-based approach is localized especially when it is combined with free form deformation (FFD) (94). With the FFD BSp approach, each control point is predominately influenced by the neighboring grid tiles. This feature makes it suitable for registering the WM to both *ex*MR and *in*MR images as well as the WM to the ERCinMR images. The BSp approach however, provides a smooth and continuous deformation field and thus is far from ideal for directly registering PWM to ERCinMR.

Some studies have used mutual information (MI) as an alignment measure (82,91,92,96-100). MI has been specifically designed to address registration of multi-modal data (100) and is based on information theory (99). The robustness of the MI approach for dissimilar modalities can be enhanced via

the combined feature ensemble mutual information (COFEMI) technique which incorporates additional information for one of the modalities in the form of image features (91). The robustness and the results of this technique are highly dependent on the selection of the image features. The MI-based approach incorporated by the COFEMI technique has been used for registering WM to both *ex*MR and *in*MR images (91) while the Spatial Weighting Mutual Information (SWMI) technique has been used for registering PWM to ERCinMR images (92), addressing the same problem focused on in the current study. While the SWMI work addressed the same challenging problem of registering in vivo MRI with PWM data presented in this work, only a limited number of cases were demonstrated. While the SWMI method doesn't require the identification of the capsule border it also demonstrated lower registration accuracy compared to LATIS with a DSC of 0.83 on average.

Given the scope of registration problems best handled by the previously described methods, we desired a new approach which was more appropriate to register PWM and ERCinMR and required a minimum amount of *a priori* information. First of all, the existing methods available in the literature required an investigator, or sometimes feature recognition software, to identify sufficient numbers and distributions of control points to guide the registration between the histopathological and MRI images. Recognizing the fact that registration between two images requires some pre-defined controls, we observed that there were clearly some features that could be defined with reasonable precision. One feature was the prostate boundary and the others were larger internal structures like the central gland-peripheral zone boundary, transition zone, apex-semicircular sphincter and bilateral nodules of benign prostatic hypertrophy. This addressed the challenge of identifying numerous control points with exact spatial correspondence between the source and target images as required by the BSp and TPS methods. Identification of landmarks was often difficult and the number of points would have been insufficient for guiding registration. The difficulty of

selecting spatially corresponding control points is evidenced by the large discrepancy between the number of points the two researchers selected for determination of registration accuracy. However, the identification of larger anatomic structures was always possible in our test cases.

The second issue with the aforementioned methods was the underlying assumption of a continuous deformation field which is less appropriate when registration involves PWM data. Therefore, we developed a method based on the invariance of the image intensity function, which does not require the assumption of continuous deformation fields. This feature makes the resulting method suitable to handle the local distortions that lie within the PWM images such as the unfilled space or gaps between the QMHS.

To address the discontinuous nature of the reassembled PWM images and to overcome the overall challenge of multi-modal registration, tri-intensity masks of both datasets taking into account the prostate border and large internal structures were used as the source and target images for registration. While not the focus of this work, it could easily be envisioned that BSp and TPS could be used for registering the tri-intensity images in place of the local affine transformation chosen here however, the identification and selection of control points would still be necessary and a limiting factor to their successful implementation.

3.5.2 Registration and Pathology Limitations

Both LATIS, and the other referenced registration studies, have addressed a two-dimensional registration problem. Therefore, an important requirement (i.e. the first assumption in LATIS) is that the source and target images originate from the same plane through the prostate. Even with careful attention to the sectioning protocol multiple factors can lead to axial planes which do not match between the

MRI and pathology, including non-linear shrinking of the tissue during fixation. This lack of correspondence would further complicate, if not eliminate, the possibility to find features for guiding registration. The selection of control points used by TPS and BSp based on small structural features would arguably be the most affected. However, LATIS may be less sensitive to the same offsets due to the persistence of larger structural features through plane. The influence of both through-plane offsets and in-plane registration errors must be considered when evaluating the registration accuracy of annotated cancer regions from pathology to imaging. The relative impact of any error would be greater for smaller areas of disease.

Additional limitations exist in the most apical and basal regions. As described in the sectioning protocol, the most apical section of the prostate is removed and cut in the sagittal orientation. Using LATIS in this orientation has not been explored to date. One obvious limitation is the absence of a complete capsule contour. In the base, several aspects of the sectioning protocol and the anatomy make identification of the prostatic capsule and assembly of the PWM difficult including, the ambiguous prostate-bladder border, amputation of the seminal vesicles and vasa deferentia at the base and shaving of the proximal urethral margin to a thickness prior to placement in the sectioning box. The end result is the absence of a well-defined capsule in the most basal slices which makes them difficult to handle with the proposed methods.

Despite the previously described limitations, the sectioning protocol and registration methods have proven to be relatively robust in the cases studied to date. In general, less than 15% of cases handled in our lab needed to be excluded from registration due to mismatches in slice orientation (i.e. an obvious violation of assumption No. 1) and less than 3% of cases had to be excluded due to index lesions too for inferior or superior in the prostate.

3.5.3 Assessment of Registration Error

The assessment of image registration accuracy in literature has been has been accomplished using a variety of error metrics. In the present study registration accuracy was calculated using 1) the dice similarity as a “global” metric for characterizing the registration of the tri-intensity images (i.e. capsule and large internal structures) and 2) corresponding landmarks identified manually in both source and target images to characterize registration accuracy of internal features of the prostate. Similar methods have been used in the literature to assess registration accuracy (101-109).

The need to perform accurate registration between PWM and ERCinMR stems from the desire to use pathological results as the ground truth for interpreting the MRI results for determining the extent and aggressiveness of disease. A “perfect” registration would permit a reliable pixel–wise analysis of MRI with respect to histopathology however, the ability to approach this ideal correspondence is difficult due to the complexity of the distortions and the limited information available to correct for them. To improve our registration method, future implementations could incorporate other MRI visible structures like the urethra. The LATIS approach could also serve as a baseline method in a cascaded registration procedure, where additional registration steps incorporating other previously proposed strategies and information may be used to further improve the correspondence of salient features between the datasets. Using LATIS would be a valuable first step for the reasons stated above, including that 1) it relies on the selection of large structures rather than specific points which makes it more robust in cases where the prostate slicing and MRI imaging plane are not exactly the same, 2) it does not rely on image intensity from the multi-modal data and 3) it does not assume a smooth continuous deformation field, an assumption, which is violated in the case of the PWM data.

In the future improved error metrics for assessing registration accuracy would also be desired in order to compare LATIS with other registration methods and potentially cascaded approaches. Potentially this is possible by acquiring additional information in the process of generating the PWM and acquiring the ERCinMR data such as images of the gross pathology sections cut into quarters prior to paraffin embedding and imaging of the prostate after excision and before sectioning (exMR). The intermediate exMR acquisition step is useful because of similarity of MR signal intensities between exMR and ERCinMR images and superior axial resolution of the exMR scan excision of the tumor enabling accurate registration with PWM. This information may help elucidate the deformations present between the source PWM data and the target ERCinMR and provide a more complete characterization of the deformations to better evaluate other strategies which do not require the labor and time to acquire the additional data.

In conclusion, the main geometric issues in histopathology-MR image registration are the distortions resulting from the use of an endorectal coil when acquiring the *in*MR data, the deformation due to removal, and fixation and distortion of individual QMHS which result in discontinuities in the final assembled PWM. In this work, this registration problem is addressed by using LATIS which involves identifying large internal structures along with the prostate boundary to guide registration. While the method to assess the registration accuracy was subjective, it is an important first step in the validation of the technique.

Chapter 4 Developing MP-MRI Cancer Predictive Models using Co-registered regions of Defined Disease

This was a collaborative project primarily between Dr. Greg Metzger, Dr. Joseph Koopmeiners, Dr. Stephen Schmechel and me. My contribution consisted of assisting in scanning 70 clinical subjects and developing the analysis workflow which involves coordination, analysis and manipulation of:

1. MRI DICOM images obtained on the scanner.
2. Anatomic and molecular digital pathology data stored on Aperio Servers at the hospital.
3. Intermediate data generated within Matlab.

I incorporated a unified visualization environment based on OsiriX into the workflow as current analysis and visualization tools were found insufficient to handle the types of data required for MP-MRI model generation. This enabled simultaneous visualization of all derived MRI datasets, import and manipulation of registered areas of annotated cancer and generation of ROI location reports for subsequent analysis against co-registered pathologic markers. I generated all co-registered pathology cancer and non-cancer data used in the MP-MRI model and manipulated the statistical processing code in R statistical environment (110) to generate the different MP-MRI model results.

4.1 Introduction

In this chapter, the development of multiparametric models will be addressed for cancer detection from the quantitative data described in Chapter 2. Compared to the use of individual MRI datasets, multiparametric MRI (MP-MRI) models have also shown promise for improving PCa detection (41-47). The most relevant

previous studies are summarized in Table 4.1 and characterized by the following: the types of MRI datasets used, whether these were qualitatively or quantitatively evaluated, identifies which were region or voxel based, the type of pathologic "Gold Standard" used (i.e. biopsy or post-prostatectomy) and the target outcome (i.e. detection or grade). Langer et al. (41) constructed a 3 parameter logistic regression based model for mapping peripheral zone (PZ) tumors using ADC (Apparent Diffusion Coefficient), T_2 and K^{trans} at 1.5T. Matulewicz et al. (42) used an artificial neural network (ANN) model for automatic detection of cancerous voxels in the prostate from ^{1}H-MRSI datasets at 1.5T. Poulakis et al. (46) developed an ANN model for predicting biochemical recurrence based on the pelvic coil MRI, PSA measurement, and biopsy Gleason score, after radical prostatectomy at 1T. Puech et al. (47) used generalized estimating equations (GEEs) to construct a computer assisted diagnosis (CAD) software capable of generating a standardized cancer suspicion score for suspicious foci detected in DCE-MRI T_1-w images obtained at 1.5T. Anderson et al. (43) combined logistic regression and nearest neighbor classification to generate an augmented model using DCE, DW (Diffusion Weighted) and MRSI (Magnetic Resonance Spectroscopy Imaging) datasets to predict PCa in the whole prostate. Litjens et al. (45) developed a Random Forest Classifier based CAD system to detect PCa in the whole prostate at 3T. Finally, Delongchamps et al. (44) used combinations of T_2-weighted imaging, DCE and DWI for the detection of PCa in the whole prostate at 1.5T.

The process of assessing -MP-MRI's ability to predict disease is determined through correlation with a pathologic Gold Standard. This correlation involves mapping the information from pathology (i.e. grade and location of identified disease) onto the MRI data and has been accomplished through a variety of methods in the literature: manual mapping of regions of interest (ROIs) (41); visual mapping of sextants (42) or octants (43,44); mapping locations of graded MR guided biopsy specimens (45) or calculated Gleason scores

(43,46,47). The process of correlating manually drawn regions of interest (ROIs) (41) on the MRI corresponding to identified areas of disease on pathology introduces potential biases of both ROI drawing and placement. Studies that use pathology mapped regions in the form of sextants(42) or octants (43,44) are limited due to the loss of underlying voxel heterogeneity. The limitations of these methods are addressed in the current methods where a direct mapping of digitally annotated regions of graded disease are mapped to the MRI image using LATIS, detailed in **Chapter 3** (48).

#	Reference	Year	Input Parameters							Model			Outcome		Performance
			Used Datasets	Combination	B_0 (T)	# of Patients	Dataset type	Gold Standard	Pathology-MRI Correlation	Type	MRI Basis ROI or Voxel	Detection Area	Continuous or Binary	Result	AUC
1	Langer et al.	2009	ADC, T_2m, K^{trans}	ADC+T_2+K^{trans}	1.5	25	QUAN	WMH & HGS	Manual mapping of ROIs	LR	Voxel	PZ	C	Mapping of PZ tumor	0.706(0.692,0.719)
2	Matulewicz et al.	2013	MRS, AS	MRS+AS	1.5	18	QUAN	WMH	Visual mapping of sextant	ANN	Voxel	WP	B	Detection of cancerous voxels	0.968(0.937,0.999)
3	Poulakis et al.	2004	pMRI. PSA, TBGS, TNM	pMRI+PSA+ GS+CS	1	191	QUAL QUAN	TBGS	Based on GS	ANN	ROI	WP	B	Biochemical failure	0.897±0.063
4	Puech et al.	2009	WI, WO	WI, WO	1.5	100	SQ	TBGS & HGS	Based on GS	GEE	Voxel	PZ & TZ	C	5 point malignancy suspicion score	0.777
5	Anderson et al.	2014	K^{trans},ADC, MRS, T_2m, nCK_{NN}	K^{trans} + ADC + MRS + T_2 + nCK_{NN}	-	28	QUAN	HGS WMH	Based on GS and visual mapping of octants	LR KNN	Voxel	WP	B	Identify risk of cancer and most aggressive cancer on a on a slice	0.85
6	Litjens et al.	2014	T_2w, ADC, b800, T_2m, K^{trans}, K_{ep}, Tau, LateWash. Blobness, Texture, Anatomical	T_2w + ADC + b800 + T_2m + K^{trans} + K_{ep} + Tau + LateWash + Blobness + Texture + Anatomical	3	347	QUAN	MB specimen	Mapped locations of graded MB specimens	RFC	Voxel	WP	C	Likelihood of cancer map	0.81
7	Delongchamps et al.	2010	T_2w,b800, ADC, K^{trans}, K_{ep}, AUGC	T_2w T_2w + DWI T_2w + DCE T_2w + DWI + DCE	1.5	57	QUAL	WMH	Visual Mapping of octants	CA	ROI	PZ & TZ	B	Cancer Detection in the TZ based on a point scale Cancer Detection in the PZ based on a point scale	0.84(0.79,0.89) T_2w 0.88(0.83,0.92) T_2w+DWI 0.70(0.63,0.76) T_2w+DCE 0.75(0.69,0.80) T_2w+DCE+DWI 0.81(0.75,0.86) T_2w 0.92(0.88,0.96) T_2w+DWI 0.91(0.86,0.94) T_2w+DCE 0.92(0.88,0.95) T_2w+DCE+DWI
8	Kalavagunta et al. (Current Work)	2014	ADC, T_2m, K^{trans}, K_{ep}, AUGC	ADC + T_2 + K^{trans} + K_{ep} + AUGC	3	46	QUAN	PWMH	Co-registration	LASSO	Voxel	WP, CG & PZ	C	Composite biomarker score	Please see Results section

pMRI	Preoperative MRI Findings like Extracapsular extension, Seminal vesicle invasion, positive surgical margin and MRI staging
AS	Anatomic Segmentation (percentage)
MRS	MRS :Magnetic Resonance Spectroscopy Metabolite Ratios
MB	MRI Guided Biopsy
CS	Clinical Stage
GS	Gleason Score
nCKNN	No of Cancer Neighbors from the K-Nearest Neighbor Model
VI	Visual Interpretation
WI	Wash-in
WO	Wash-out
TBGS	TRUS Biopsy Gleason Score
HGS	Histopathology Gleason Score
WMH	Whole Mount Histopathology
TNM	TNM Staging System
QUAN	Quantitative
QUAL	Qualitative
PWMH	Pseudo Whole Mount Histopathology
LR	Logistic Regression
ANN	Artificial Neural Network
GEE	Generalized Estimating Equations
KNN	K-Nearest Neighbor
LASSO	LASSO:Least Absolute Shrinkage and Selection Operator
WP	Whole Prostate
CG	Central Gland
T2w	T2-weighted images
T2m	T2-map
b800	High b-value image [ref]
Tau	Dynamic parameter, related to time-to-peak of contrast agent concentration [ref]
Late wash	Dynamic parameter realted to eashout of contrast agent [ref]
Texture	Multi-scale gaussian derivatives on T2w image [ref]
Blobness	Multi-scale blob detection using Li blobness filter on ADC, Ktrans, Latewash and Tau maps [ref]
Anatomical	Relative cumulative position within the prostate mask between 0 and 1 in the x, y, z direction and relative distance from prostate boundary and PZ likelihood. [ref]
RFC	Random Forest Classifier
LGEE	Logistic Generalized Estimating Equations
CA	Correlation Analysis

Quantitative datasets include mpMR parameters,
Qualitative data are obtained from visual based assessment
Semi Quantitative data include colorized parametric maps of WI WO overlaid on top of morphologic images, such as T2WI, to facilitate interpretation.

Table 4.1 A comparison of visual assessment and predictive model resultant combinations of MP-MRI datasets in the prediction of PCa.

In comparison to the studies mentioned in Table 4.1, this chapter presents a predictive model building approach that offers the following distinct advantages that stem from the use of co-registered pathology data.

1. Reduce pathology correlation bias: The use of directly mapped co-registered regions of Post PPP onto in-vivo MP-MRI images is free from biases outlined above.
2. A pixel-wise analysis approach that allows investigation of apparent non-coincidence of quantitative MR (qMR) parameters.
3. All data use in the modeling is quantitative with the potential to apply prospectively to MP-MRI data acquired without any quantitative assessment or interaction.
4. All lesions with volumes greater than 0.19 cc (maximum volume 17cc) were included in the modeling thus not limiting the results to the detection of large volumes of disease.
5. A separate model is presented for discriminating cancer from non-cancerous central gland tissue.
6. Inclusion of all pixels from the prostate – both from cancer and non-cancer allows this model to approach an ideal situation where all available input data is used for model generation. This also allows the full heterogeneity of both cancerous and non-cancerous regions to be accommodated in the model and more closely represent the type of data a model would have to handle when applied in a clinical setting.

In this chapter we develop and validate several models for MP-MRI PCa detection in the whole prostate, central gland (CG) and peripheral zone (PZ) using voxel-wise post prostatectomy pathology (PPP) registered cancer and non-cancer data obtained zonally or from the whole prostate.

4.2 Methods

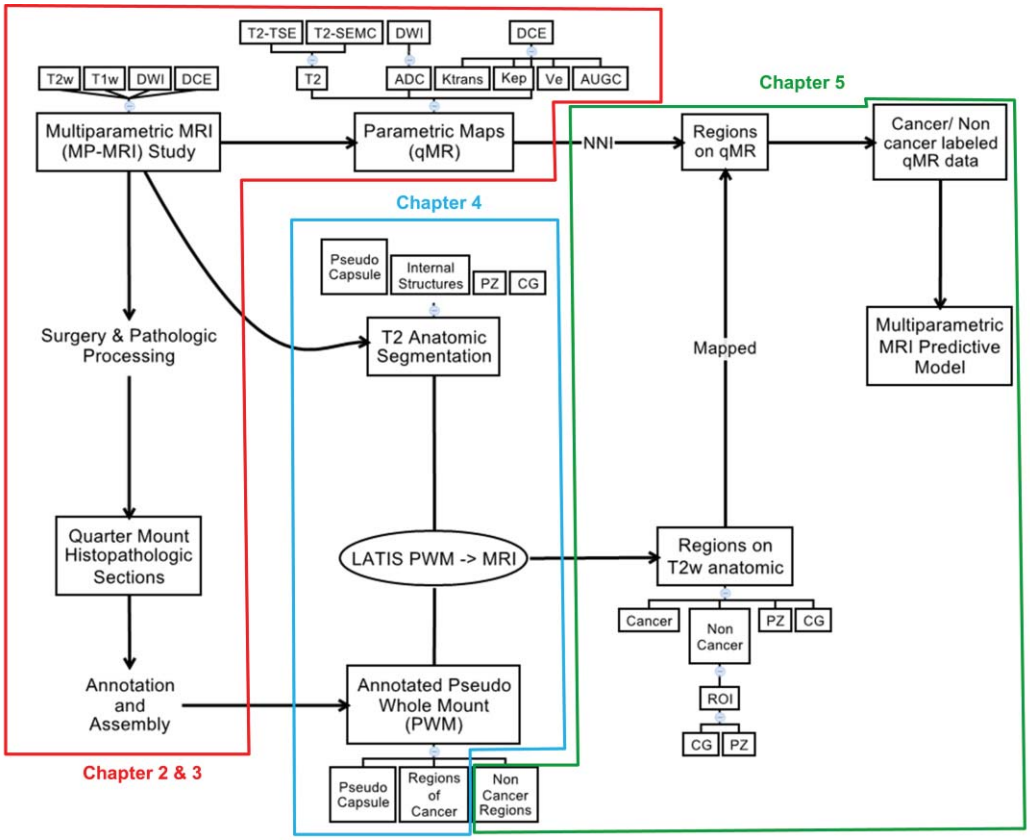

Figure 4.1 Process of acquiring data for predictive model generation.

From the patient studies defined in **Chapter 3 Section 3.1**, input data (i.e. MP-MRI data) and output data (i.e. pathology data) were defined for development of predictive models. This process is outlined in Figure 4.1 and provided below:

1. Assemble the annotated PWM pathology data into volumes and combined capsule annotations and cancer annotations into lesions.
2. Identify coincident slices between anatomic T_2w MRI and pathology for registration.

3. Define the pseudo-capsule border and division between the PZ and CG on the anatomic T_2w Images.
4. For a given slice pair (i.e. MRI and pathology), perform LATIS deformable registration using the capsules and large internal structures defined on both pathology and T_2w images.
5. Map areas of cancer from pathology onto anatomic MRI.
6. Using the mapped areas of disease classify all voxels in the anatomic T_2w MRI slice as non-cancer PZ, non-cancer CG or PCa.
7. Map this voxel classification from the T_2w anatomic MRI to the interpolated quantitative MRI (qMR) datasets accounting for any motion either through-plane or in-plane using a manual rigid body approximation within OsiriX.
8. Extract all qMR from non-cancer and cancer regions for use in developing the predictive models.
9. Perform LASSO regression on subsets of the data to develop regions specific or whole organ predictors for prostate cancer detection.

4.2.1Data for Model Development

Annotations of cancer were defined by a study pathologist on the digitized pathology as detailed in **Chapter 2 Section 2.3.3**. The annotated slides were assembled into pseudo-whole mounts and then into complete prostates. This volumetric reassembly allowed continuous volumes of cancer to be linked together and defined as lesions. A given lesion can be characterized by its size given in units of cm^3 by standard methods knowing the resolution of the digitized pathology, knowledge of the pathologic block thickness and accounting for a shrinkage factor of 25% (111). For a given prostate, the lesion with the highest grade or largest volume was identified as an index lesion (IL). Any other significant volume of disease identified in the prostate were also identified as secondary (SL) or tertiary (TL) lesions based on decreasing grade/volume.

The MRI slice location corresponding to the center of the cancer lesion defined on pathology was determined by verifying the approximate distance from the apex and existence of similar anatomic features. Annotated regions of cancer from pathology were then registered to the corresponding anatomic T_2w image using LATIS (Chapter 4(48)) which has been demonstrated to have a registration accuracy of 1.54±0.64mm and a Dice Similarity Coefficient of 0.991±0.004.

The goal at this point is to define the following regions: non-cancer PZ (NC_{PZ}), non-cancer CG (NC_{CG}), cancer PZ (PC_{PZ}) and cancer CG (PC_{CG}). This process requires several steps. First, the anatomic T_2w images were further segmented into two regions (i.e. CG and PZ) using a semi-automated segmentation program (Segasist, Ontario, Canada). To generate the non-cancer regions, all registered cancer masks were first subtracted from the prostate's pseudo-capsule mask determined from the anatomic T_2w data. The cancer masks were first dilated by 3 pixels (~1.5 mm) before subtraction to accommodate for mis-registration. The NC_{CG} was then given as the intersection of the prostates pseudo-capsule (eroded by 1 pixel) minus the regions of cancer and the segmented CG region. The NC_{PZ} region was the remainder of the voxels from the eroded and cancer subtracted pseudo-capsule. Figure 4.2 (a, b, c) shows three examples of how these regions are defined in the prostate for various cases.

Next, these regions, and the voxels within them, need to be identified on all the qMR datasets. As there is a possibility of motion between scans during an MP-MRI study, accommodations had to be made to shift the regions detailed above. As methods to register between the MP-MRI datasets are not yet developed, a rigid body deformation was assumed to map the regions from the T_2w anatomic series to the qMR data. The through-plane (12/124) shifting and in-plane (35/124) translation for qMR data sets was manually determined to correct for changes due to patient motion and EPI distortion. This was done using OsiriX (Pixmeo, Geneva, Switzerland) software, where all qMR data sets

along with the anatomic T_2w data with registered cancer regions could be displayed simultaneously. Internal features and the borders of the prostate were used to determine proper adjustment on each qMR dataset.

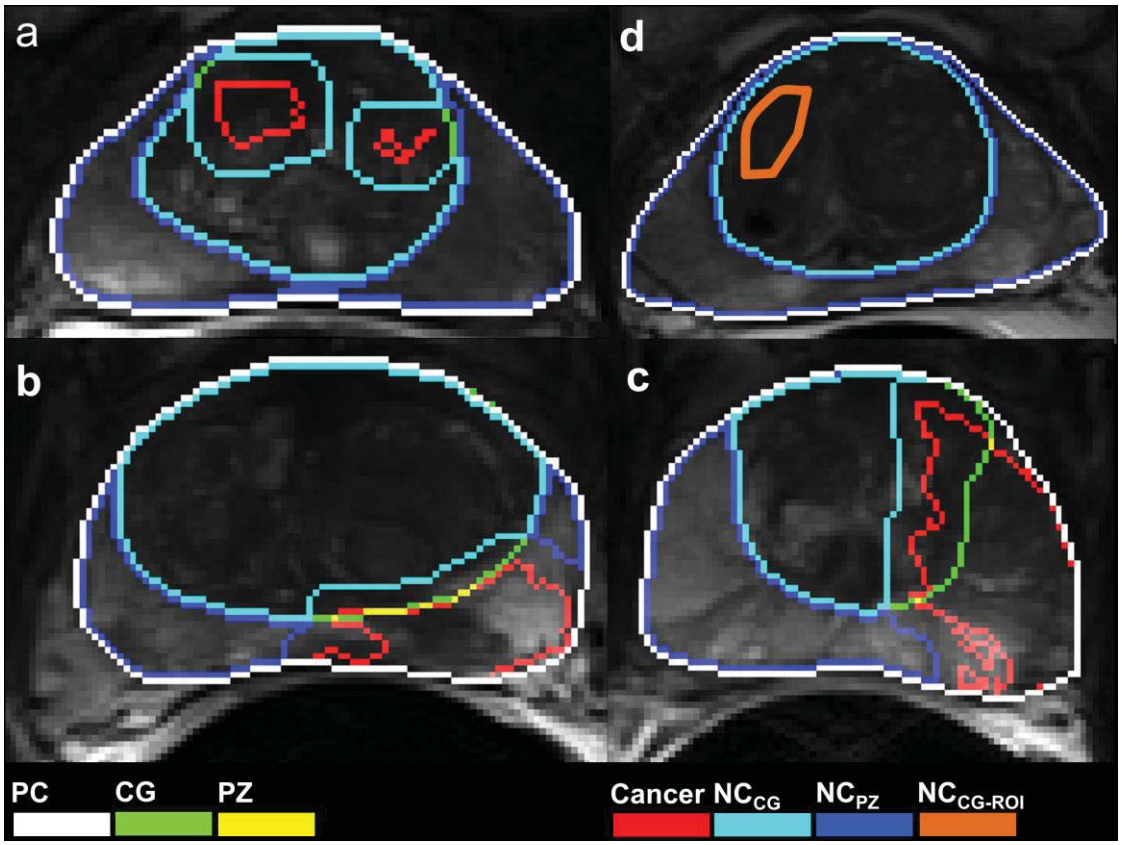

Figure 4.2 Visualization of cancer and non-cancer regions used in model generation from four patients on the un-interpolated T2w anatomic images. PCa is confined to (a) CG only (b) PZ only (c) both CG and PZ. (d) shows an example of a non-cancer user defined ROI in the CG ($NC_{CG\text{-}ROI}$). PC stands for Pseudo Capsule. The CG (green) and PZ (yellow) annotations provided the original segmentation of the two prostatic regions. These annotations are mostly overlapped by the other annotation therefore they only appear as broken curves in this figure.

4.2.2 Non-cancer from user defined ROIs

Non-cancer regions determined from the process above included all non-cancer pixels from the transverse slice of the prostate which intersected the

center of the lesion of interest. Especially for CG, this presents a real challenge both because of the abundance of benign disease but also due to the inclusion of the urethra and the fibromuscular cap which have qMR characteristics similar to cancer even when healthy. To explore the impact of non-cancer voxel selection on the predictive models, a separate set of non-cancer CG data was identified from user defined ROIs. These regions, referred to as $NC_{CG\text{-}ROI}$, were at least 9 mm away from cancer and avoided the urethra and fibromuscular cap.

4.2.3 Predictive Modeling

Data Pool		Cancer Data	Non Cancer Data	
No	Name	Origin	Origin	Type
I	PZ	PZ	PZ	NC_{PZ}
II	CG	PZ + CG	CG	NC_{CG}
III	ALL	PZ + CG	PZ + CG	NC_{CG}, NC_{PZ}
IV	CG_{ROI}	PZ + CG	CG	$NC_{CG\text{-}ROI}$

Table 4.2 Characteristics of data pool (number, name, origin and type of cancer and non-cancer data) used in model generation.

Based on the different combinations of cancer and non-cancer ROIs available, four pools of data were generated as shown in Table 4.2. Pool I and II enabled detection of cancer from non-cancer in the PZ and CG, respectively. Pool III was created to predict cancer from non-cancer across the whole prostate irrespective of zone. Because the CG data in pools I through III were derived from all pixels outside the PZ but in the prostate, it included structures such as the urethra and anterior fibromuscular cap. To investigate how the CG voxel

selection impacted the model development, another data pool (IV) was constructed using $NC_{CG\text{-}ROI}$ data.

Data pools (I-IV) were filtered to exclude zero voxels from failed parametric mapping, primarily from the DCE-MRI and T_2 mapping datasets. The remaining voxels were used to generate cancer and non-cancer median values for each qMR parameter, the correlation between qMR parameters, ROC analysis results for each parameter and ROC analysis results for models based on combinations of the parameters. A p-value comparing the composite marker to the single best marker was also calculated. One-sided p-values were reported instead of two-sided p-values to show the performance of multiple markers compared to a single marker.

All predictive models were run on only those subjects with complete records for all the qMR parameters. The classification accuracy of various approaches (Logistic regression, Generalized Estimating Equations, Naive Bayes Classifier, Support Vector Machines and Least Absolute Shrinkage and Selection Operator (LASSO) (112) in PCa prediction was tested on Data Pool I and was compared with that obtained from an individual qMR parameter (ADC). This comparison was done for each approach using all 9 parameters (ADC, T_2-TSE, T_2-SEMC, T_1-DESPOT1, T_1-TSE, K^{trans}, K_{ep} and AUGC) and a 5 parameter subset comprised of (ADC, T_2-TSE, K^{trans}, K_{ep} and AUGC). Receiver Operator Characteristic (ROC) based Area Under ROC curve (AUC) and ROC (0.1) (Sensitivity corresponding to 90% Specificity) statistics were calculated for each approach. Based on the results of this comparison we chose a LASSO method based modelling approach (112).

Approach	Parameters	AUC	ROC(0.1)
Individual Parameter	ADC	0.82	0.58
Logistic Regression	Subset of all 9 Parameters	0.82	0.56
	Subset of T_2-TSE, ADC, K^{trans}, K_{ep} and AUGC	0.83	0.60
GEE	Subset of T_2-TSE, ADC, K^{trans}, K_{ep} and AUGC	0.83	0.59
Naïve Bayes Classifier	All 9 parameters	0.80	0.49
	Only T_2-TSE, ADC, K^{trans}, K_{ep} and AUGC	0.82	0.49
SVM	All 9 parameters	0.65	0.18
	Only T_2-TSE, ADC, K^{trans}, K_{ep} and AUGC	0.42	0.08
LASSO – using a subset of 9 parameters	2 parameters	0.83	0.61
	3 parameters	0.83	0.60
	4 parameters	0.83	0.60
	5 parameters	0.83	0.59
	6 parameters	0.83	0.60
	7 parameters	0.83	0.60
	8 parameters	0.83	0.59
	9 parameters	0.83	0.59
LASSO- *using a subset of T_2-TSE, ADC, K^{trans}, K_{ep} and AUGC*	2 parameters	0.83	0.61
	3 parameters	0.83	0.60
	4 parameters	0.82	0.60
	5 parameters	**0.84**	**0.62**

Table 4.3 Classification accuracy summaries for various modeling approaches used to develop a MP-MRI model for predicting PCa using cancer and non-cancer data in the peripheral zone only (Data Pool I). The LASSO 5 parameter approach was chosen based on these results.

Feature selection and modeling was performed by logistic regression with the LASSO method run in RStudio (113) utilizing the R statistical environment (110) . All statistical analysis was done using standard R packages such MASS

(114), geepack (9,14,115), e1071 (22), kernlab (116), rje (117), pROC (13) and ROCR (10). After the initial training and validation sets were established forward stepwise selection was performed using leave one out cross validation to select the optimum subset of the 8 qMR parameters. The optimum subset LASSO model was applied to all the data pools (I-IV). For each pool, the corresponding best LASSO model was called L#P_PZ, L#P_ALL, L#P_CG, L#P_CG_{ROI} respectively where # is the optimum number of qMR parameters. Bootstrap methods were used in R for computing standard errors and confidence intervals.

For each data pool, ROC curve plot showing the best LASSO model along with best performing single predictor was generated. The $ROC_{0.1}$ (sensitivity corresponding to 90% specificity) cutoff value was also shown on the plot. Using the $ROC_{0.1}$ cutoff, plots of sensitivity of each model for each cancer region versus the number of voxels in the cancer region were generated. A composite biomarker score (CBS) for each pixel in the cancer region was generated based on the linear regression coefficient output from the model, such that,

$$\mathrm{CBS} = ß_0 + ß_{qMR(1)} \cdot qMR(1) + ß_{qMR(2)} \cdot qMR(2) + \ldots . ß_{qMR(n)} \cdot qMR(n) \qquad (4.1)$$

Where $ß_0$ and $ß_{qMR}$ are the LASSO model output linear regression coefficients for respective qMR parameters and *n* is the optimum number of qMR parameters needed to create the best performing model. The sensitivity of the model per cancer region was calculated by dividing the number of voxels whose CBS was greater than the $ROC_{0.1}$ cutoff (model predicted cancer) by the total number of voxels (true positives) in the cancer region. The specificity of the model per non cancer region was calculated by dividing the number of voxels whose CBS was less than the $ROC_{0.1}$ cutoff value (model predicted non-cancer) by the total number of voxels (true negatives) in the non-cancer region. This method of visualizing region-wise sensitivity and specificity was useful in assessing the performance of the model based on the size of the cancer/non-cancer region.

Image registration and qMR parameter dataset generation was done using the Matlab (MathWorks, Natick, MA). ROC Curves were plotted in Origin (OriginLab, Northampton, MA). Sensitivity per cancer region and specificity per non cancer region plots were generated in Microsoft Excel 2010.

4.3 Results

The total number of cancer and non-cancer voxels per data pool are tabulated in table 4.4. Median, maximum and minimum values of qMR data from the four data pools used for model generation are summarized in Table 4.5. Correlation between qMR parameters was, in general, weak, with the highest correlation seen between DCE-MRI parameters. Correlation coefficients among the DCE-MRI ranged from r = 0.92 between K^{trans} and AUGC, r = 0.68 between K_{ep} and K^{trans} (r = 0.68) and r = 0.52 between K_{ep} and AUGC where r is the correlation coefficient.

Voxels		Data Pool							
		PZ		CG		ALL		CG_{ROI}	
		SP	MP	SP	MP	SP	MP	SP	MP
Cancer	Initial	22,541	22,541	22,541	22,541	22,541	22,541	22,541	22,541
	Final	19,457	18,412	22,541	2,354	22,541	1,574	22,541	6,735
Non Cancer	Initial	46,849	46,849	111,774	111,774	111,774	111,774	8,363	8,363
	Final	34,992	31,104	66,684	6,245	111,774	6,940	8,363	3,883

Table 4.4 Total number of cancer and non-cancer voxels from each data pool used for Single Predictor (SP) and Multi Predictor (MP) model generation. The difference in the number of initial and final cancer and non-cancer MP voxels in CG, ALL and CG_{ROI} pools is due to a sampling cutoff of 200 voxels from each region used in the R code for faster processing. A comparison of the results obtained using all voxels with those obtained using a 200 voxels cutoff showed no difference.

qMR	Data Pool							
	PZ		CG		ALL		CG_{ROI}	
	Cancer	Non Cancer	Cancer	Non Cancer	Cancer	Non Cancer	Cancer	Non Cancer
T_2-TSE (ms)	96 (92, 104)	128 (121, 136)	95 (92, 101)	100 (96, 104)	95 (91, 101)	109 (105, 113)	95 (91, 100)	122 (110, 133)
p value	< 0.001		0.14		< 0.001		< 0.001	
ADC (10^{-6}× mm^2/s)	857 (763, 976)	1372 1329, 1427)	830 (742, 929)	1136 (1058, 1208)	830 (734, 917)	1226 (1163, 1276)	830 (744, 922)	1081 (899, 1189)
p value	< 0.001		< 0.001		< 0.001		0.012	
K^{trans} (10^{-3}×min^{-1})	154 (128, 184)	93 (79, 107)	146 (115, 174)	104 (94, 116)	146 (116, 175)	101 (89, 110)	146 (116, 173)	109 (93, 137)
p value	< 0.001		0.004		< 0.001		0.07	
K_{ep} (10^{-3}×min^{-1})	586 (496, 684)	422 (374.8, 477)	551 (477, 649)	363 (328, 395)	551 (473, 656)	387 (352, 418)	551 (469, 641)	438 (363, 508)
p value	< 0.001		< 0.001		< 0.001		0.02	
AUGC	322 (293, 371)	215 (186, 244)	313 (264, 352)	244 (215, 264)	313 (254, 352)	225 (205, 254)	313 (264, 352)	264 (215, 322)
p value	< 0.001		0.002		< 0.001		0.218	

Table 4.5 Median, 95% confidence intervals for qMR cancer and non-cancer values from data pools used in 5 parameter model generation. Also shown are the p values showing whether cancer qMR values are statistically significant from non-cancer values.

Figures 4.3,4.4,4.5 and 4.6 show the results for LASSO models applied to data pools I to IV respectively. Each figure includes:

a) A Receiver Operator Characteristic (ROC) curve for the best performing LASSO model and single predictor.
b) Table showing AUC and $ROC_{0.1}$ values for each individual predictor and optimum parameter subset based on stepwise addition of significant qMR parameters for each LASSO model.
c) Sensitivity per cancer region plotted vs. number of pixels in each cancer region.
d) Specificity per non-cancer region vs. number of pixels in each non-cancer region.

a

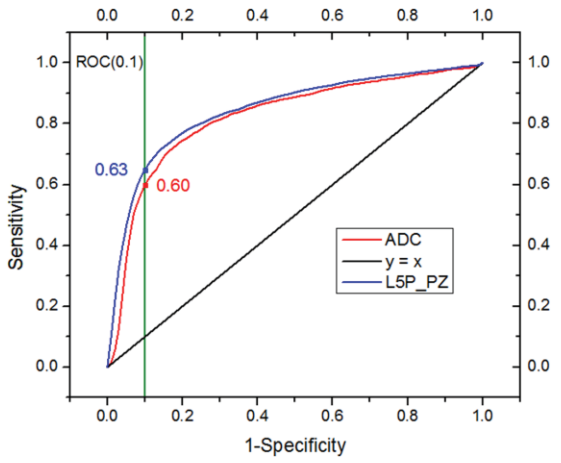

b

		AUC	$ROC_{0.1}$
Single Predictor	**ADC**	**0.82(0.77,0.87)**	0.60(0.47,0.71)
	K^{trans}	0.73(0.66,0.80)	0.33(0.17,0.50)
	AUGC	0.73(0.66,0.79)	0.25(0.15,0.40)
	T_2-SEMC	0.75(0.69,0.81)	0.40(0.27,0.52)
	T_2-TSE	0.74(0.67,0.80)	0.33(0.24,0.45)
	K_{ep}	0.65(0.58,0.72)	0.27(0.15,0.40)
	V_e	0.59(0.51,0.67)	0.15(0.04,0.30)
	T_1-DESPOT1	0.53(0.42,0.63)	0.11(0.05,0.17)
L2P	ADC + K_{ep}	0.83(0.72,0.89)	0.62(0.34,0.75)
p value		0.29	0.41
L3P	Above + AUGC	0.84(0.80,0.90)	0.63(0.46,0.78)
p value		0.05	0.16
L4P	Above + T_2-TSE	0.85(0.80,0.91)	0.65(0.51,0.80)
p value		**0.02**	0.05
L5P	**Above + K^{trans}**	**0.84(0.81,0.90)**	0.63(0.54,0.78)
p value		**0.02**	**0.03**

c

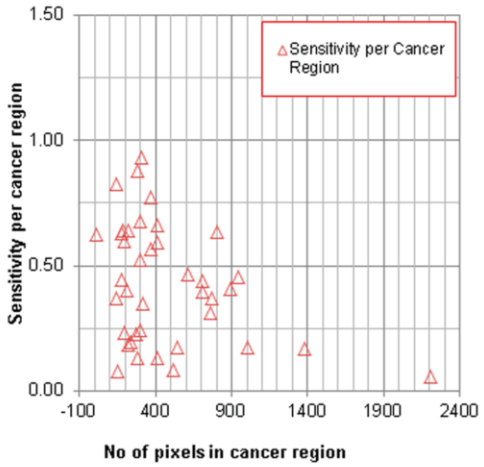

d

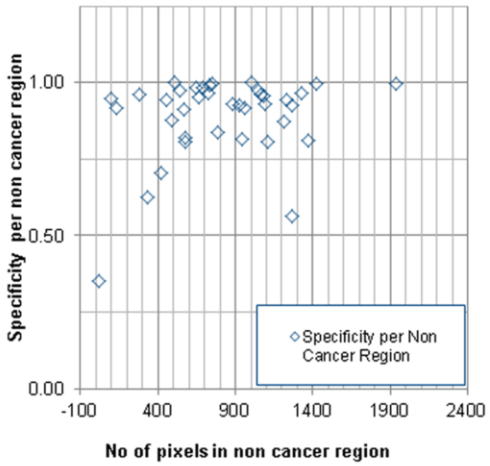

Figure 4.3 L5P_PZ model results. (a) ROC curve for L5P model and ADC showing the $ROC_{0.1}$ cutoff (b) Table showing AUC and $ROC_{0.1}$ values for each single predictor and L5P_PZ model. L5P_PZ results are shown in order of incremental addition of significant predictor to the model. Plots (c) and (d) show the L5P_PZ model's performance for cancer and non-cancer regions of different size by the calculation of sensitivity per cancer region and specificity per non cancer region.

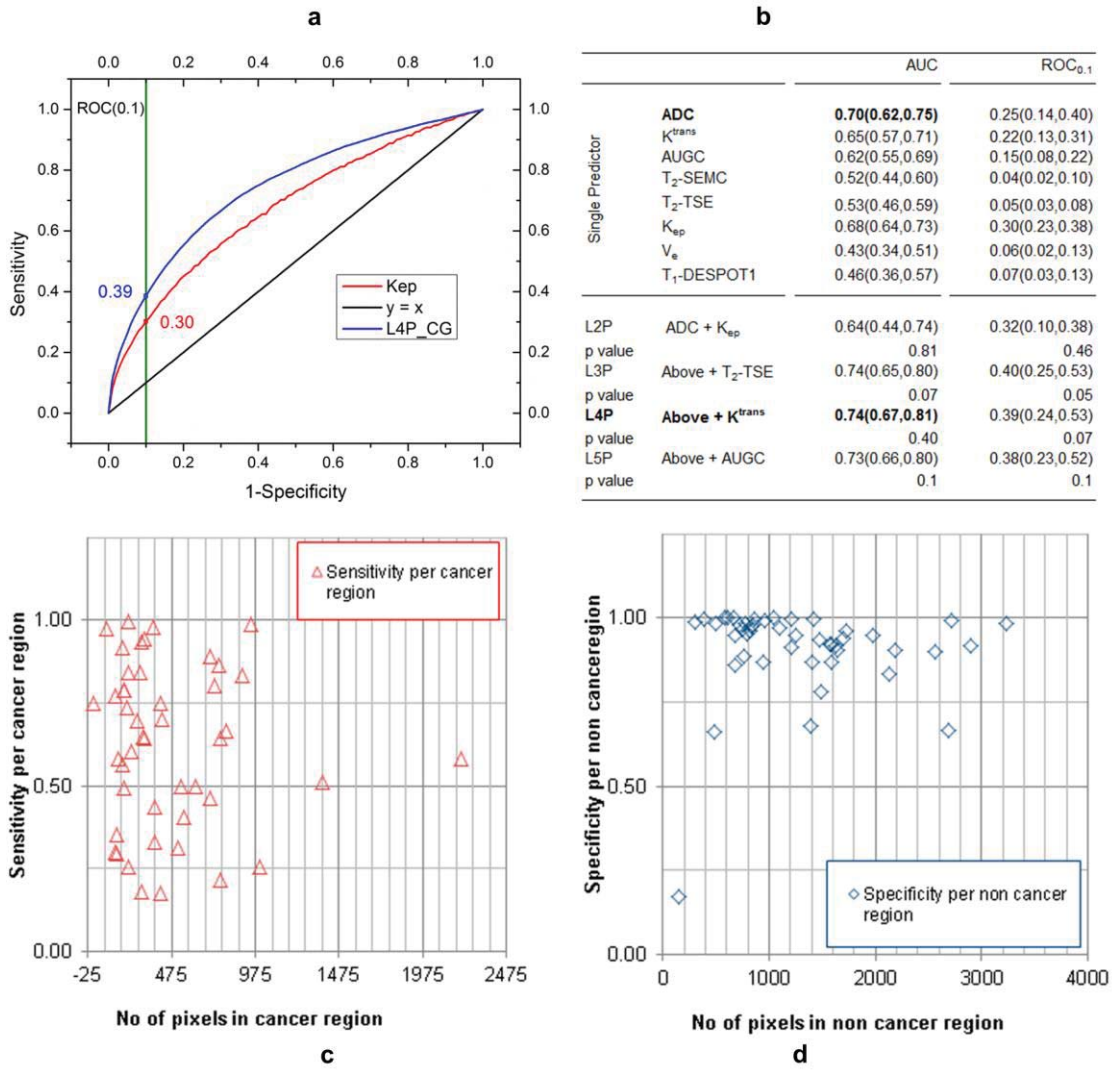

		AUC	$ROC_{0.1}$
Single Predictor	**ADC**	**0.70(0.62,0.75)**	0.25(0.14,0.40)
	K^{trans}	0.65(0.57,0.71)	0.22(0.13,0.31)
	AUGC	0.62(0.55,0.69)	0.15(0.08,0.22)
	T_2-SEMC	0.52(0.44,0.60)	0.04(0.02,0.10)
	T_2-TSE	0.53(0.46,0.59)	0.05(0.03,0.08)
	K_{ep}	0.68(0.64,0.73)	0.30(0.23,0.38)
	V_e	0.43(0.34,0.51)	0.06(0.02,0.13)
	T_1-DESPOT1	0.46(0.36,0.57)	0.07(0.03,0.13)
L2P	ADC + K_{ep}	0.64(0.44,0.74)	0.32(0.10,0.38)
p value		0.81	0.46
L3P	Above + T_2-TSE	0.74(0.65,0.80)	0.40(0.25,0.53)
p value		0.07	0.05
L4P	**Above + K^{trans}**	**0.74(0.67,0.81)**	0.39(0.24,0.53)
p value		0.40	0.07
L5P	Above + AUGC	0.73(0.66,0.80)	0.38(0.23,0.52)
p value		0.1	0.1

Figure 4.4 L4P_CG model results. (a) ROC curve for L4P_CG model and ADC showing the $ROC_{0.1}$ cutoff (b) Table showing AUC and $ROC_{0.1}$ values for each single predictor and L4P_CG model. L4P_CG results are shown in order of incremental addition of significant predictor to the model. Plots (c) and (d) show the L4P_CG model's performance for cancer and non-cancer regions of different size by the calculation of sensitivity per cancer region and specificity per non cancer region.

a

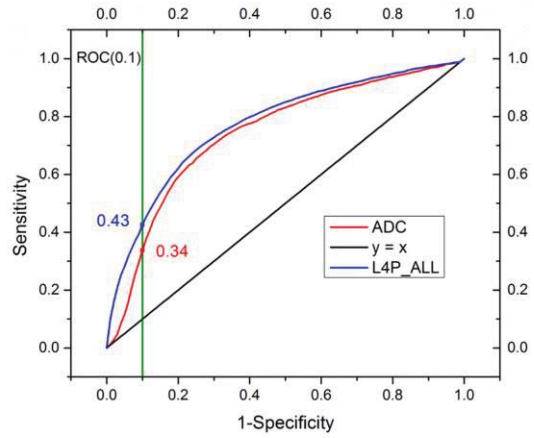

b

		AUC	$ROC_{0.1}$
Single Predictor	**ADC**	**0.74(0.69,0.79)**	0.34(0.22,0.46)
	K^{trans}	0.66(0.61,0.73)	0.23(0.16,0.33)
	AUGC	0.64(0.59,0.71)	0.16(0.09,0.24)
	T_2-SEMC	0.61(0.55,0.67)	0.10(0.05,0.16)
	T_2-TSE	0.61(0.56,0.66)	0.09(0.06,0.14)
	K_{ep}	0.66(0.62,0.72)	0.28(0.23,0.36)
	V_e	0.47(0.41,0.55)	0.08(0.03,0.16)
	T_1-DESPOT1	0.51(0.41,0.58)	0.09(0.04,0.15)
L2P	ADC + K_{ep}	0.72(0.52,0.79)	0.28(0.11,0.40)
p value		0.86	0.89
L3P	Above + T_2-TSE	0.78(0.70,0.83)	0.43(0.26,0.58)
p value		0.09	0.13
L4P	**Above + AUGC**	**0.77(0.72,0.83)**	0.43(0.29,0.58)
p value		**0.04**	0.09
L5P	Above + K^{trans}	0.77(0.72,0.83)	0.42(0.29,0.58)
p value		0.05	0.11

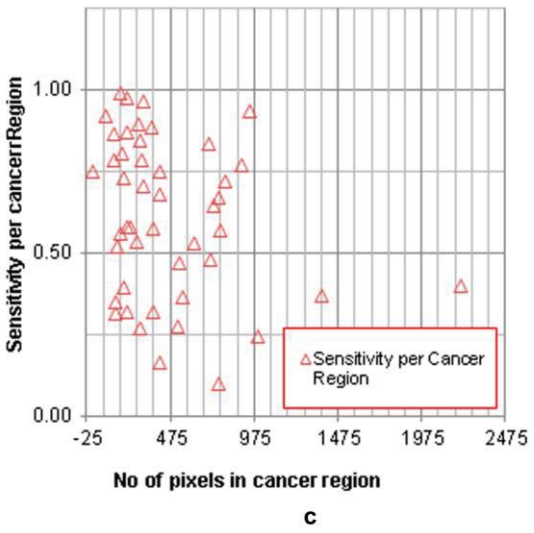

c

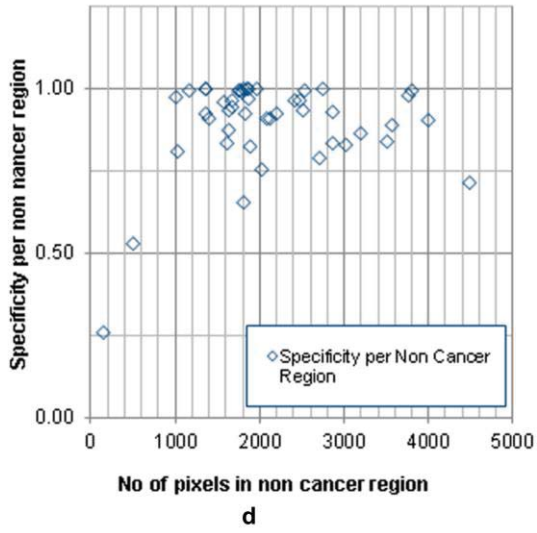

d

Figure 4.5 L4P_ALL model results. (a) ROC curve for L4P_ALL model and ADC showing the $ROC_{0.1}$ cutoff (b) Table showing AUC and $ROC_{0.1}$ values for each single predictor and L4P_ALL model. L4P_ALL results are shown in order of incremental addition of significant predictor to the model. Plots (c) and (d) show the L4P_ALL model's performance for cancer and non-cancer regions of different size by the calculation of sensitivity per cancer region and specificity per non cancer region.

a

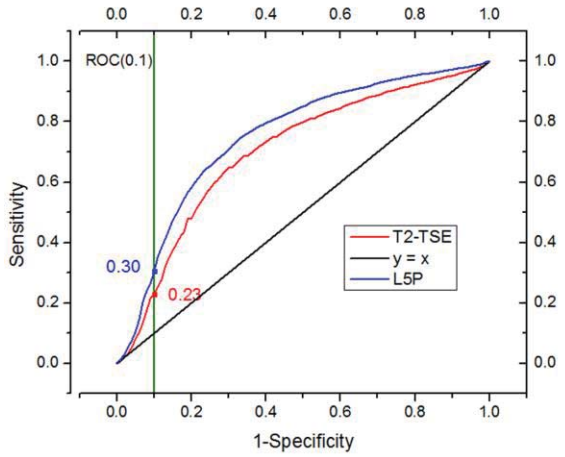

b

		AUC	$ROC_{0.1}$
Single Predictor	ADC	0.65(0.53, 0.75)	0.18(0.05, 0.42)
	K^{trans}	0.61(0.50, 0.72)	0.17(0.07, 0.35)
	AUGC	0.57(0.45, 0.68)	0.12(0.03, 0.25)
	T_2-SEMC	0.62(0.49, 0.72)	0.10(0.02, 0.30)
	T_2-TSE	**0.70(0.60, 0.80)**	0.23(0.11, 0.44)
	K_{ep}	0.61(0.52, 0.70)	0.20(0.12, 0.35)
	V_e	0.50(0.37, 0.60)	0.80(0.01, 0.23)
	T_1-DESPOT1	0.48(0.32, 0.63)	0.13(0.03, 0.26)
L2P	ADC + K_{ep}	0.37(0.10,0.65)	0.09(0,0.28)
p value		0.975	0.84
L3P	Above + T_2-TSE	0.58(0.25,0.70)	0.17(0.001,0.37)
p value		0.96	0.72
L4P	Above + AUGC	0.63(0.31,0.71)	0.24(0.02,0.38)
p value		0.90	0.61
L5P	**Above + K^{trans}**	**0.62(0.35,0.73)**	0.30(0.06,0.40)
p value		0.86	0.51

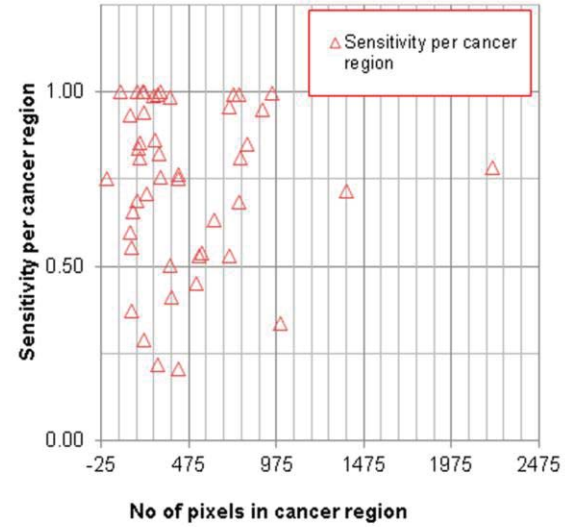

c

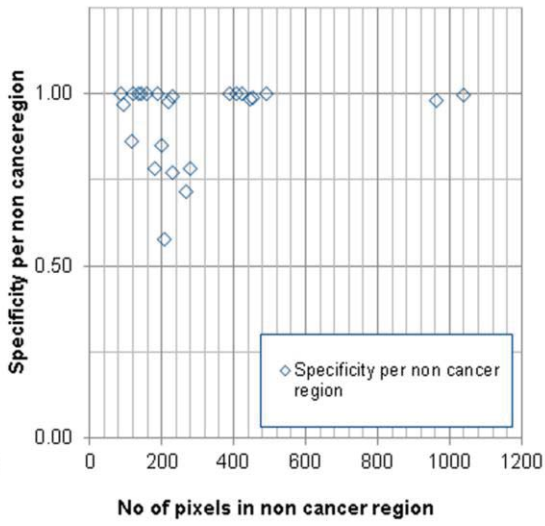

d

Figure 4.6 L5P_CG_{ROI} model results. (a) ROC curve for L5P_CG_{ROI} model and ADC showing the $ROC_{0.1}$ cutoff (b) Table showing AUC and $ROC_{0.1}$ values for each single predictor and L5P_CG_{ROI} model. L5P_CG_{ROI} results are shown in order of incremental addition of significant predictor to the model. Plots (c) and (d) show the L5P_CG_{ROI} model's performance for cancer and non-cancer regions of different size by the calculation of sensitivity per cancer region and specificity per non cancer region.

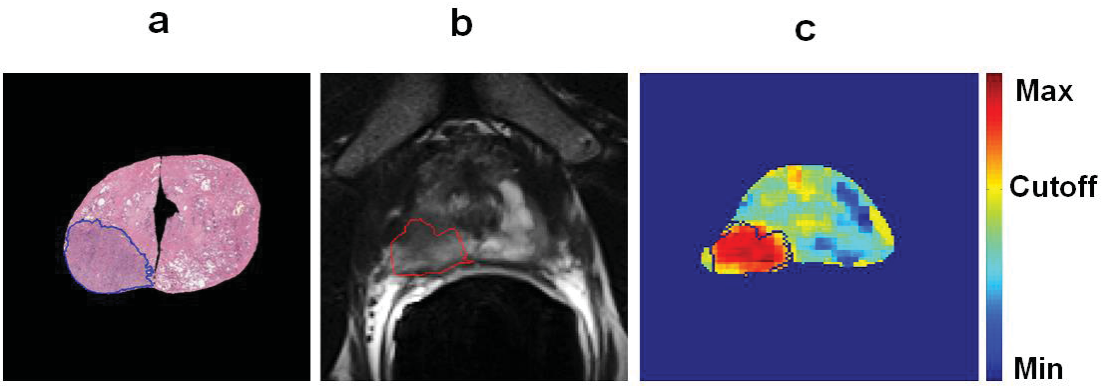

Figure 4.7 72 year old man with biopsy-confirmed PCa with Gleason score, 6 on the right side PZ of the prostate. (a): PWM with tumor outlined in blue. (b)Corresponding T_2-weighted MRI with registered tumor region overlay, and (c) composite biomarker score (CBS) map acquired using a L5P_PZ model with registered tumor region outline in black. Associated CBS colorbar shows ROC0.1 cutoff. The PZ tumor region can be seen appreciated in against the background in the CBS map and is composed of pixels with CBS > cutoff.

Generation of a CBS map using the L5P_PZ model for a representative case where the tumor is present in the right PZ is shown in Figure 4.7

Based on AUC calculations, ADC was the best performing single parameter for detection of PCa in data pools PZ, CG and ALL. T_2-TSE was the best single predictor for CG_{ROI}. The best performing LASSO models for data pools I-IV based on AUC values in incremental order of significant qMR parameters were L5P_PZ (ADC, AUGC, K_{ep}, T_2-TSE and K^{trans}), L4P_CG (K_{ep}, ADC, T_2-TSE, ,AUGC and K^{trans}), L4P_ALL (ADC, K_{ep}, T_2-TSE and AUGC), L5P_CG_{ROI} (K_{ep}, ,ADC, T_2-TSE, AUGC and K^{trans}).

L5P_PZ was the best performing model among all the other LASSO models with the highest AUC (0.84(0.81, 0.90)) and $ROC_{0.1}$ value (0.63(0.54, 0.78)). Among individual predictors, ADC had the highest AUC (0.82(0.77, 0.87)) and $ROC_{0.1}$ value (0.60 (0.47, 0.71)) for data pool I. Among all the models L5P_PZ shows the least variation in sensitivity per cancer region w.r.t. cancer region size whereas L4P_CG shows the least variation of specificity per non cancer region w.r.t non cancer region size. L4P_CG_{ROI} was not considered in the

specificity comparison as data pool IV includes annotated non-cancer regions that lack the heterogeneous makeup of non-cancer regions from data pools I-III.

4.4 Discussion

This chapter demonstrates the results of predictive MP-MRI models for PCa detection based on co-registered pathology as the gold standard for defining both regions of cancer and non-cancer. Manually transferring regions of cancer from pathology to imaging can bias the input data used to generate the predictive models. In this manual process, the features of the target image can't help but greatly influence the manual interpretation of the pathologic ROI on the MRI. The first issue is, which MRI dataset should be used. As the features of cancer on T_2, ADC and DCE-MRI are not always co-incident or even present, the transferred pathologic ROI would necessarily be different dependent on the MRI dataset chosen as the basis for transference. Second, it is not always clear where the cancer region is on the MRI especially in smaller volumes of disease or around the borders of disease where less distinct features are available due to partial voluming or lower grade disease. In this case, how is the region of cancer transferred? Most likely the process is different in this case where there are more distinct features of disease to assist in the region drawing on MRI. Finally, in cases of distortion between MRI and pathology, the region drawing becomes even more user dependent as local landmarks, which are sometimes hard to find, are not clearly identifiable close to the region where the ROI is needed. The use of pathology co-registered regions used for model development as shown in this work reduces potential bias in the determination of the training data regions and more accurately represents the wide range of values and spatial correspondence encountered in a multi parametric image set, compared with the use of summary values. This non-biased selection of cancer and inclusion of all non-cancer pixels is unique in this work.

The developed LASSO models combine information from multiple qMR datasets to generate a composite predictor score (CBS) to assess the risk of malignancy, precluding review of each MRI scan separately. While Figure 4.7 shows an example of a CBS map where a cutoff corresponding to the $ROC_{0.1}$ was used, the determination of an appropriate cutoff is still required for the application of each model prospectively and most likely will depend on the clinical application.

All the four multi-parametric LASSO models were able to better distinguish between voxels in normal and malignant prostate tissue, as determined quantitatively through the calculation of the mean area under the ROC curve, AUC compared to individual qMR parameters as shown in figures 4.3, 4.4, 4.5 and 4.6. The AUC values of the single and MP-MRI models lies within the range of studies shown in Table 4.1 (AUC range: [0.692, 0.999]); however, is important to note that since these models predict cancerous voxels in the prostate the ROC statistics are calculated voxel-wise and not region-wise.

The L4P_ALL and L4P_CG models show that four qMR parameters are most effective at detecting PCa in the whole prostate or CG alone however the best qMR parameters to use depends on the data pool. The plotted sensitivity per cancer region and specificity per non cancer region versus region size shows the performance of each model across regions of different sizes. It is important to note that these plots are based on $ROC_{0.1}$ cutoff and therefore give an expected high specificity. It would be desirable to have a cancer detection model with consistent sensitivity irrespective of lesion size. Among the four models L5P_PZ shows the least sensitivity to lesion size. The most likely reason for this is the absence of CG data from the non-cancer pool greatly reducing variability of the non-cancer data used for model development.

Training and test data for LASSO model generation used cancer data in combination with different pools of non-cancer voxels from CG and PZ tissue in the prostate. The different combinations were investigated because the

parameter values measured in the central gland differ from those measured in the peripheral zone and therefore, potentially, each zone may benefit from a different model. The limited number of CG lesions in the entire patient cohort (9 in 46 patients) lead to development of models L4P_CG and L5P_CG_{ROI} based on all cancer data (i.e. both GZ and PZ cancers) but different types of non-cancer data obtained from the CG. In L4P_CG, non-cancer data was obtained from NC_{CG} whereas L5P_CG_{ROI} had non-cancer data obtained from NC_{ROI}. In L4P_CG, the use of NC_{CG} obtained from prostates with CG cancer annotations along with those from prostates with PZ cancers allowed the assessment of model performance in detecting PCa in CG using a larger non-cancer CG data pool. In L5P_CG_{ROI}, ROIs for 'normal' data were restricted to exclude periurethral and fibromuscular cap regions that exhibit cancer-like characteristics as seen on MRI. It is possible that these ROIs may also contain regions of benign disease (e.g. Benign Prostate Hyperplasia)..

As seen from the difference between the initial and final number of cancer voxels in Table 4.4 in data pools II-IV 200 voxels were sampled from each cancer and non-cancer region. A comparison of all four model results obtained using all cancer & non cancer voxels versus a subset of 200 voxels showed no significant difference. This showed that after a certain point adding additional observations (voxels) from a single cluster (slice) provided essentially no information for estimating the predictive model other than slowing down the computer code used for fitting the model.

4.5 Conclusion

In this chapter the development of a multi-parametric MRI model to identify cancerous voxels in prostate tissue generated using pathology–MR coregistered datasets has been presented. Single and MP-MRI models for PCa

detection were obtained from pathology co-registered T_2, ADC, and DCE-MRI datasets with the final MP-MRI model including ADC, T_2-TSE, K^{trans}, K_{ep} and AUGC. These MP-MRI models can be used for the prediction of cancerous voxels in the peripheral zone, central gland or the whole prostate.

Chapter 5 Application of Methods to High and Ultra High-Field MP-MRI

5.1 Context

Multiparametric MRI studies of the prostate at ultra-high magnetic field(UHF) (i.e. 7T) carry with them the promise of improved disease characterization resulting from improvements in SNR, better parallel imaging performance and increased spectral resolution. This advancement to higher fields comes with its own disadvantages including higher motion sensitivity, increase in local specific absorption rates (SAR), B_1 field inhomogeneities and susceptibility artifacts. While initial MRI studies at 7T have been performed to explore the potential for improved PCa detection using anatomical imaging (118) and functional imaging studies (4,119), much work is still needed. One of the challenges in conducting DCE-MRI studies on the prostate at 7T is a limited understanding of the increasing influence of T_2* on T_1w acquisitions. While r_1 relaxivity has been shown to slightly decrease with increasing field strength, r_2* relaxivity increases dramatically and can dominate signal changes especially at higher CA concentrations. The standard conversion of change in signal intensity to change in concentration is affected by R_2* which is typically ignored as it is assumed that TE << T_2*, however this is no longer the case at 7T. The increasing R2* with field strength has a significant effect on the enhancement curves in tissue and catastrophic effects on the signal in the vasculature (4). To understand both R_1 and R_2* relaxivity, the following study was performed looking at both blood and saline at both 3T and 7T. The findings are relevant to paramagnetic contrast agent studies performed at UHF including DCE-MRI performed outside the prostate and vascular studies performed with contrast at throughout the body.

The rest of this chapter is adapted with permission from the following publication: Kalavagunta, C., Michaeli, S. and Metzger, G. J. (2014), *In vitro Gd-DTPA relaxometry studies in oxygenated venous human blood and aqueous solution at 3 and 7 T*. Contrast Media Mol Imaging, 9: 169–176. doi: 10.1002/cmmi.1568

This was a collaborative project between Dr Greg Metzger, Dr Shalom Michaeli and me. I devised a ways to obtain venous blood, oxygenate it, generate highly calibrated serial concentrations of Gd-DTPA and present the samples for experimentation in the MRI scanner while keeping everything at 37±2 °C. For post processing I performed relaxometry measurements calculations and fitted parameters accounting for propagated errors which greatly increased confidence in the final results.

5.2 Synopsis

In-vitro T_1 and T_2^* relaxivities (r_1 and r_2^*) of Gd-DTPA (GaD) in oxygenated human venous blood (OVB) and aqueous solution (AS) at 3T and 7T were calculated. GaD concentrations ([GaD]) in OVB and AS were prepared in the range 0-5 mM. All measurements were acquired at 37±2 ºC. At both 3T and 7T, a linear relationship was observed between [GaD] and R_1 in both AS and OVB. At 7T, r_1 in AS decreased by 7.5% ($p = 0.045$) while there was a negligible change in OVB. With respect to R_2^*, a linear relationship with [GaD] was only observed in AS, while a more complex relationship was observed in OVB; quadratic below and linear above 2 mM at both field strengths. There was a significant increase of over four-fold in r_2^* with GaD in OVB at 7T (for [GaD] above 2mM, $p << 0.01$) as compared to 3T. Furthermore, in comparison to r_1, r_2^* in AS was less than two-fold higher at both field strengths while in OVB it was ~twenty-fold and ~ninety-fold higher at 3T and 7T, respectively. This observation emphasizes the importance of r_2^* knowledge at high magnetic fields, ≥3T. The comparison between r_1 and r_2^* presented in this work is crucial in the design and optimization of high field MRI studies making use of paramagnetic contrast agents. This is especially true in multiple compartment systems such as blood where r_2^* dramatically increases while r_1 remains relatively constant with increasing magnetic field strength.

5.3 Introduction

The paramagnetic effectiveness of a contrast agent (CA) is measured by its relaxivity which is defined as the rate by which the relaxation rate changes per unit molar CA concentration. Typically the effect of clinically used paramagnetic gadolinium based contrast agents on the longitudinal relaxation rate constant R1≡1/T1 is of most interest. However, understanding CA based changes in

R2*≡1/T2*, a function of both spin-spin interactions and local magnetic field inhomogeneities, is becoming more important as clinical and research endeavors expand into ever increasing magnetic fields. The increasing R2* effect with gadolinium based CAs at higher fields compete with the T1-weighted signal increase relied upon in post-contrast anatomic imaging, contrast enhanced angiography studies and dynamic contrast enhanced MRI (DCE-MRI). Increasing concentrations of CA result in higher R1 values and increased signal on T1-weighted acquisitions while also producing higher R_2* which disproportionately decreases signal at higher concentrations. Based on the results determined in this study, sub-millisecond T2* relaxation times at 7T are possible with Gd-DTPA concentrations ([GaD]) of 5 mM in the blood. Such concentrations can easily be reached in-vivo when high injection rates of 3 ml/s are used (120) such as in DCE-MRI studies of the prostate.

Previous studies have shown that, without correcting for T_2* signal attenuation, subject dependent determination of the arterial input function was impossible for such studies (4). Similar effects are expected to negatively impact other contrast enhanced studies when performed at 7T such as first pass perfusion and angiography exams relying on T_1-weighted enhancement (5).Understanding the field dependent relationship between the two relaxation rate constants with respect to CA concentration in blood can be undertaken by defining both R_1 and R_2^* relaxivities, r_1 and r_2^* respectively, and will be necessary for understanding the tradeoffs of using gadolinium based CAs at high fields and in the optimization of both acquisition parameters and injection paradigms. While there is a wealth of information investigating the relaxivity of gadolinium based CA in the literature, there are also an equal number of varying acquisition methods and experimental conditions which can greatly vary the results. Therefore, the goal of this work was to use consistent experimental methods at both 3T and 7T to determine r_1 and r_2^*. For the paramagnetic CA, the relaxivity is a function of the motional correlation times, which includes several dynamic

components characterizing electron–proton dipolar coupling (121) and involving the magnetic moment of the metal ion. As the solvent of the CA has a tremendous effect on the relaxation properties, we investigated the relaxivity in both an aqueous solution (AS) and in fully oxygenated venous blood (OVB), both at physiological temperatures of 37±2°C. Because of its prominence in the literature and clinically use in our institution and elsewhere, Gadolinium-DTPA (Magnevist^{TM}, Bayer, Germany) (GaD) was the CA used in this study.

5.3.1 Theory

The addition of a paramagnetic CA like GaD to a solution increases both relaxation rate constants R_1 and R_2. The observed $R_{1,2(obs)}$ after addition of GaD is the sum of the native relaxation rate of the solution $R_{1,2(N)}$ plus any contribution from GaD defined as $R_{1,2(GaD)}$. Thus $R_{1,2(obs)} = R_{1,2(N)} + R_{1,2(GaD)}$ (assuming independence of the relaxation pathways). In dilute solutions of GaD the observed relaxation rate constant R_1 is assumed to be linearly dependent on [GaD]. The slope of the dependence is the relaxivity and the y-intercept is the native relaxation rate of the sample prior to the addition of GaD i.e. $R_{1,2(obs)} = r_{1,2(N)} \times [GaD] + R_{1,2(N)}$, where $r_{1,2(N)}$ is the relaxivity defined as the incremental increase in the relaxation rate per unit concentration of GaD. The apparent transverse relaxation rate constant R_2^* is defined as $R_2^* = R_2 + R_2'$, where R_2^* is the observed transverse relaxation rate. R_2 is the spin–spin relaxation rate constant and characterizes fluctuating magnetic field inhomogeneity effects, and R_2' ($R_2' \equiv 1/T_2'$) is that induced by the local magnetic field inhomogeneities within the voxel (122).

5.4 Methods

Commercially available formulation of GaD, having a concentration of 0.5 M, was mixed with OVB and AS to obtain final concentrations in the range 0-5.18 mM(OVB) and 0-4.83 mM(AS), respectively.

5.4.1 OVB Sample Preparation

Venous human blood for this study was collected in a Vacuette heparin vacutainer (Greiner, Monroe, NC) through venipuncture using a standard 23-gauge butterfly needle from a healthy donor. A high gauge needle was used to minimize hemolysis during blood collection. The tube was then gently inverted six times to thoroughly mix the blood in the vacutainer with heparin. This was done to avoid blood clot formation which would have rendered the specimen unacceptable for use. The blood in each vacutainer was then collected in a 1L side arm conical flask by pouring it slowly along the wall. The blood was then exposed to moist O_2 and air using an in-house oxygenation apparatus. In this setup, dry O_2 from the cylinder was passed through a conical flask containing distilled water (Kandiyohi Bottled Water Co., Willmar, MN). The resulting moist O_2 was then passed through a pressure gauge before interacting with the venous blood in the conical flask. The moist O_2 pressure was maintained at 5-10 SLPM (standard liters per minute) during oxygenation. The conical flask was stirred gently for 1.5 hours until the sO_2 reached 100%. An iStat (Abbott Point of Care Inc., Princeton, NJ) portable clinical analyzer was used to measure hematocrit (Hct), sO_2 and pO_2. A blood gas analyzer (Rapidlab-248, Siemens, Deerfield, IL) was used to measure pO_2. The final pO_2 (293.8 mmHg) was much higher than that of arterial blood (95 mmHg)(123).

A pO_2 decrease in plastic tube stored blood samples due to metabolism has been reported (124). This drop in pO_2 can be attributed to oxygen consumption by leucocytes in blood and diffusion of oxygen through the walls of

the plastic tube. While T_1 is known to have a slight linear dependency on pO_2 (6), a high pO_2 (hyperbaric O_2) was chosen to ensure that the blood sO_2 stayed above arterial blood sO_2 levels (>94%) through the duration of the MRI measurements.

5.4.2 GaD Solution in AS and OVB Preparation

A 0.1 M HEPES buffer solution was used to maintain the pH of distilled water at 7. GaD samples in AS were made by adding [GaD] to this buffer solution. OVB obtained earlier was used as the solvent for making the GaD arterial blood solutions. A Corning (Corning Inc., Corning, NY) 15mL clear polypropylene centrifuge tube was placed on a Mettler AM100 electronic balance (Mettler-Toledo, Inc., Columbus, OH). Microscopic volumes of GaD were added to the tube using a micropipette and the weight was recorded. This was followed by adding OVB or 0.1M (pH-7) HEPES solution to the tube and the final weight of the solution was recorded. The concentration accuracy of the GaD samples was calculated based on the weight measurements. Using the recorded weights and densities of GaD, human blood and distilled water at 22°C the final [GaD] obtained were, GaD in OVB: 0.00, 0.58, 1.12, 1.79, 1.98, 2.36, 2.88, 3.70, 3.90, 4.38, 5.18 mM. GaD in AS: 0.0, 0.43, 1.00, 1.48, 1.93, 2.42, 3.05, 3.42, 3.90, 4.42, 4.83 mM.

5.4.3 Phantom Setup

For both OVB and AS studies a plastic holder was used to house the 5 ml polystyrene round bottom test tubes containing the various [GaD] solutions. The holder was placed in a perforated container and surrounded by water bath tubing. A larger container then housed the whole setup and was filled with 0.45% saline solution to facilitate B_0 shimming over the phantom, to load the transmit

coil and provide efficient heat transfer from the water bath hose. All studies were performed at a temperature of 37±2 °C. This temperature was maintained by pumping heated water through the water bath tubing (Thermo Scientific Neslab RTE- 7 Digital One). MR images of the phantom setup are shown in Figure 5.1. The temperature was monitored using a thermistor (YSI 400 series) positioned in the water bath but away from the sample tubes and a DigiSense (Cole-Parmer, Chicago, IL) Temperature Controller. Blood oxygenation (sO_2, pO_2) and Hct were measured before and after each set of T_1, T_2^* experiments. Each blood phantom sample was gently turned upside down three times to ensure mixing before placement inside the scanner.

5.4.4 MR Instrumentation

All 3T measurements were performed on a Siemens Magnetom Trio scanner. Signal reception was achieved using a 12 channel head coil. RF transmission was performed using the scanner body coil. All 7T measurements were done on a Magnex 7T, 90 cm bore magnet with Siemens console and head gradients using a 16 channel transceive head coil.

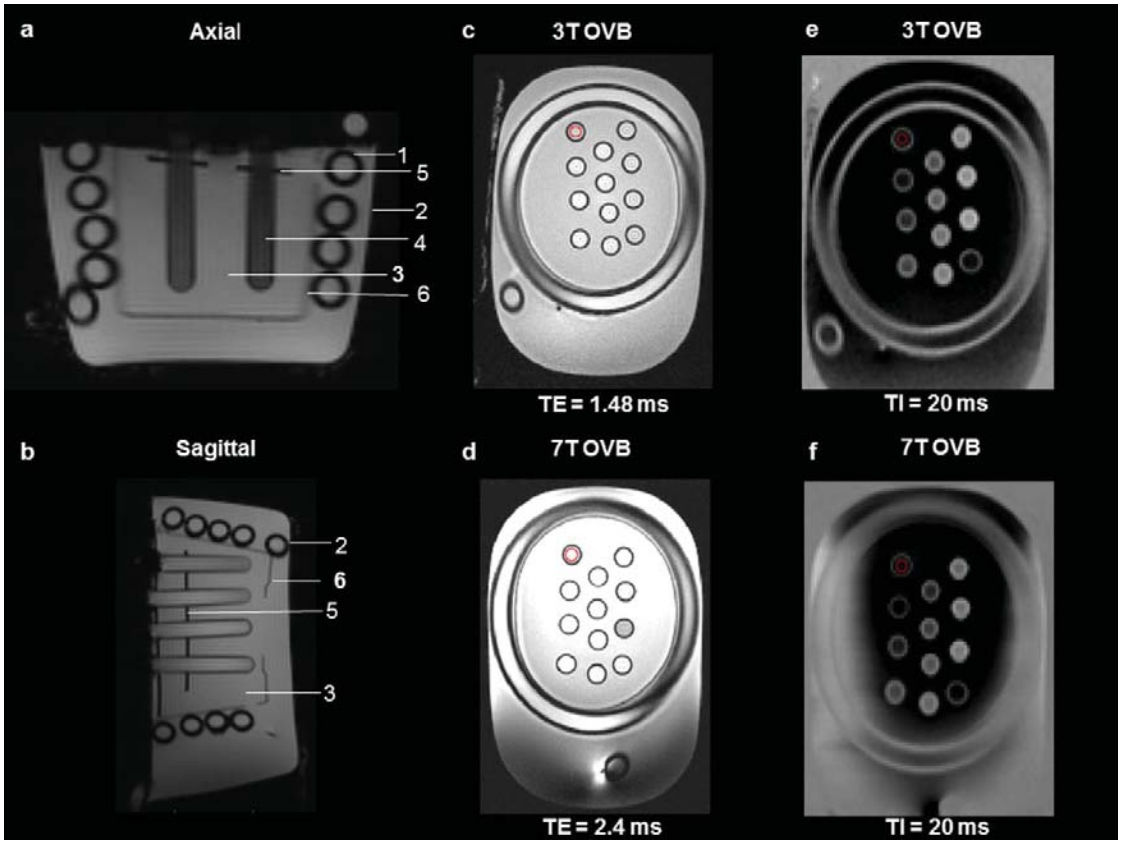

Figure 5.1 (a) Axial and (b) sagittal scout images of the phantom setup. Legend: 1, water bath tubing; 2, outer plastic container; 3, 0.45% saline water; 4, vial; 5, vial holder; 6, inner plastic container. Coronal view of the oxygenated venous blood (OVB) phantom from the first echo of the multi-echo acquisition used for calculating R_2* for (c) 3 T and (d) 7 T. Coronal view of the OVB phantom from the TI = 20 ms, inversion recovery- turbo flash (IR-TFL) acquisition for (e) 3 T and (f) 7 T. The location of circular regions of interest used for data analysis within each acquisition for the zero GaD vial are shown in (c)–(f).

5.4.5 T_1 Measurement

Multiple inversion recovery turbo flash (125) (IR-TFL) acquisitions were used to measure T_1 by varying the inversion delay. The inversion pre-pulse was accomplished with a non-selective adiabatic inversion pulse. Imaging

parameters for the IR-TFL sequence include: TR, 10 s; TE, 1.33 ms (3T), 1.05 ms (7T); nominal flip angle, 6°; acquisition matrix, 128^2; field of view, 190 mm; slice thickness, 3.5-5.0 mm; number of excitations NEX= 2; bandwidth per pixel, 1000 Hz (3T), 1395 Hz (7T). The inversion time (TI) was varied from 20 to 9000 ms (20-30 TIs). A centrically ordered phase encode ordering allowed the short TI times to be achieved at the expense of spatial blurring especially for samples with higher [GaD]. Examples of the TI=20 ms for both 3T and 7T are shown in Figure 5.2e and 1f, respectively. The T_1 measurement using the IR-TFL method was validated by using an inversion recovery spin echo acquisition with the AS phantom at 3T (IR-SE; TR, 3 s; TE, 11 ms; flip angle, 90°; acquisition matrix, 256^2; field of view, 300 mm^2; slice thickness, 5mm; NEX= 1; TI, 23 ms).

The average MR signal intensity (SI) and standard deviation for each region of interest (ROI) within each vial were obtained from the TFL images well within the vials to avoid partial volume effects with the wall of the container (Figure 5.1 e,f). For the inversion recovery sequence, the data was reconstructed in the real mode to allow negative signal intensities for fitting the T_1 recovery curve. T_2^* effects resulting from global field inhomogeneities were minimized by performing B_0 shimming within a localized coronal slab which included all the vials used in the analysis. The T_1 values were obtained by performing an instrumental fit on the ROI SIs versus their respective TIs. The equation used to fit the data was $SI(ROI) = A[0] \times (1-2\times\exp(-A[1]\times TI)) + A[2]$, where A[0], A[1] and A[2] are fit parameters such that $T_1 = 1/A[1]$. The equation was fit to the data using the LMFit function within IDL (ITT, Visual Information Solutions, Boulder, CO) which employs a Levenberg-Marquardt algorithm to find a solution to the fitted parameters. A linear relationship between R_1 and [GaD] was assumed to calculate r_1. The equation used to fit the data was $R_1 = r_1 \cdot [GaD] + Intercept$ where r_1 is the slope. The R_1 vs. [GaD] data was fit using a linear instrumental fit function in Origin 8.1(OriginLab Corp., Northampton, MA).

5.4.6 T_2^* Measurement

Multi-echo gradient echo acquisitions were performed to acquire the signal intensity data used to calculate T_2^*.Solvent and field strength dependent acquisition parameters are given in Table 5.1. Varying TE ranges and the gaps between successive echo times (ΔTE) were chosen to measure the relaxation characteristics of each sample. At 3T, measurements on both AS and OVB were acquired with two concatenated acquisitions while for OVB at 7T, 3 interleaved acquisitions were acquired with a minimum effective ΔTE (ΔTE_{eff}) of 0.81 ms to capture the potentially rapidly decaying signals for high [GaD]. Acquisition parameters common to all acquisitions included a 10 degree flip angle and 280 mm field of view. Images from the first TE of the multi-echo gradient echo acquisition and representative ROIs used for analysis are shown from the OVB phantom for both field strengths in Figure 5.1c and 1d, respectively.

T_2^* values were obtained by performing a monoexponential instrumental fit of the ROI SIs versus their respective TEs using the function: SI(ROI) = A[0]×(exp(-A[1]×TE))+A[2], where A[0], A[1] and A[2] are fit parameters and A[1] = R_2^*. The optimization routine LMFIT was used within IDL to fit the equation to the SI amplitudes. Parameter A[2] was set by identifying the SI mean magnitude of the background noise. The mean noise was also used as a threshold to limit the range of included echo times for R_2* estimation. To determine r_2^* relaxivity, the R_2^* versus [GaD] data was characterized by both a quadratic and a combination of both quadratic and linear functions. First, the full range of [GaD] was fit solely with the quadratic function ($R_2^* = A\times[GaD]^2 + B\times[GaD] + C$). Second, only lower [GaD] concentration were fit with the quadratic function while higher concentrations were fit with a linear relationship ($R_2^* = A\times[GaD] + B$). The R_2^* vs. [GaD] data was fit using the instrumental fit functions in Origin 8.1. The errors reported take into consideration the error propagation from volumetric analysis, nonlinear fit (T_1 and T_2^* calculation) and linear/nonlinear fits (r_1 and r_2^*

calculation). The standard errors of the fitting parameters were calculated from the square root of a main diagonal value of the variance-covariance matrix.

B_0	Sample	# Acquisitions	# Echoes per Acquisition	# Echoes Total	Minimum TE (ms)	ΔTE per Acquisition (ms)	Minimum ΔTE_{eff} (ms)*	TE Range (ms)	Matrix Size
3T	AS	2†	12	24	1.8	2.38	2.38	1.8-56.54	256
3T	OVB	2†	12	24	1.8	2.38	2.38	1.8-56.54	256
7T	AS	1	12	12	2.01	2.8	2.8	2.01-32.81	320
7T	OVB	3‡	4	28	2.36	2.44	0.81	2.36-11.29	320

† Acquisitions were concatenated.

‡ Acquisitions were interleaved to produce a minimum effective ΔTE shorter than the ΔTE per acquisition.

* The ΔTE after combining the data from all acquisitions.

Table 5.1 Acquisition parameters for $R2^*$ calculations.

5.5 Results

The native R_1 and R_2^* values for OVB and AS have been summarized in Table 5.2. The curve fits used to obtain r_1 and r_2^* relaxivities for [GaD] in AS and OVB are shown in Figure 5.2. The r_1 relaxivities for GaD in AS and OVB are shown in Table 5.3. For an increase in field strength from 3T to 7T there was a small (7.5%), but statistically significant ($p = 0.045$), decrease of GaD r_1 in AS with no observable change in OVB r_1 with an increase in field strength. The relationship between R_2^* and [GaD] for OVB and AS at 3T and 7T is shown in Figure 5.2. For an increase in field strength from 3T to 7T there was a 3% ($p = 0.2$) increase in GaD r_2^* relaxivity in AS (Table 5.4). In blood, the data was best described by a combined quadratic-linear relationship where a quadratic function better described the experimental data up to 1.98 mM while a linear function best described the R_2^* dependence on higher [GaD]. The most significant change in r_2^* was observed in OVB which increased over four-fold (for [GaD] beyond 2mM, $p << 0.01$).

Sample	R_1 (sec^{-1})	R_2^* (sec^{-1})
3T OVB	0.56±0.00	9.94±0.56
7T OVB	0.49±0.00	28.50±1.15
3T AS	0.24±0.00	1.38±0.81
7T AS	0.24±0.00	0.94±1.03

Table 5.2 R_1 and R_2^* values for Oxygenated Venous Blood (OVB) and Aqueous Solution (AS) at 3T and 7T at 37 ºC.

	OVB				AS
B_0	pO_2	sO_2	Hct	r_1	r_1
(T)	(mmHg)	(%)	(%)	($mM^{-1}s^{-1}$)	($mM^{-1}s^{-1}$)
3	114.5– 166.85	97-98	44	3.20±0.06	3.44±0.08
7	293.8	100	44	3.20±0.06	3.18±0.09

Table 5.3 T_1 relaxivities (r_1) of Gd-DTPA in Oxygenated Venous Blood (OVB) and Aqueous Solution (AS) at 37 ºC for both 3 and 7T along with respective pO_2, sO_2 and Hematocrit (Hct) ranges used for the measurements.

B_0	AS				OVB									
	[GaD] : 0 to 4.83 mM				[GaD] : 0 to 1.98 mM						[GaD] : 1.98 to 5.18 mM			
	$R_2^* = A\times[GaD] + B$				$R_2^* = A\times[GaD]^2 + B\times[GaD] + C$						$R_2^* = A\times[GaD] + B$			
	A	Err[æ]	B	Err[æ]	A[†]	Err[æ]	B[§]	Err[æ]	C[‡]	Err[æ]	A[⌂]	Err[æ]	B	Err[æ]
(T)	($s^{-1}mM^{-1}$)		(s^{-1})		($s^{-1}mM^{-1}$)		($s^{-1}mM^{-1}$)		(s^{-1})		($s^{-1}mM^{-1}$)		(s^{-1})	
3	4.21	0.04	1.21	0.11	5.76	4.77	26.61	8.08	8.99	2.60	68.90	6.85	-41.97	15.35
7	4.34	0.10	1.40	0.29	42.94	5.38	40.88	7.02	28.25	1.84	290.81	14.63	-270.20	33.62

† Coefficient "A" controls the speed of increase of R_2^* from the parabola vertex.

æ Fit Error.

§ B together with A controls the axis of symmetry of the parabola which is at [GaD] = -B/2A.

‡ Coefficient 'C" gives the R_2^* value of OVB (i.e. [GaD] = 0).

⌂ Slope gives r_2^*.

Table 5.4 Relationship of Gd-DTPA concentration [GaD] with R2* in Aqueous Solution (AS) and Oxygenated Venous Blood (OVB) at 3T and 7T.

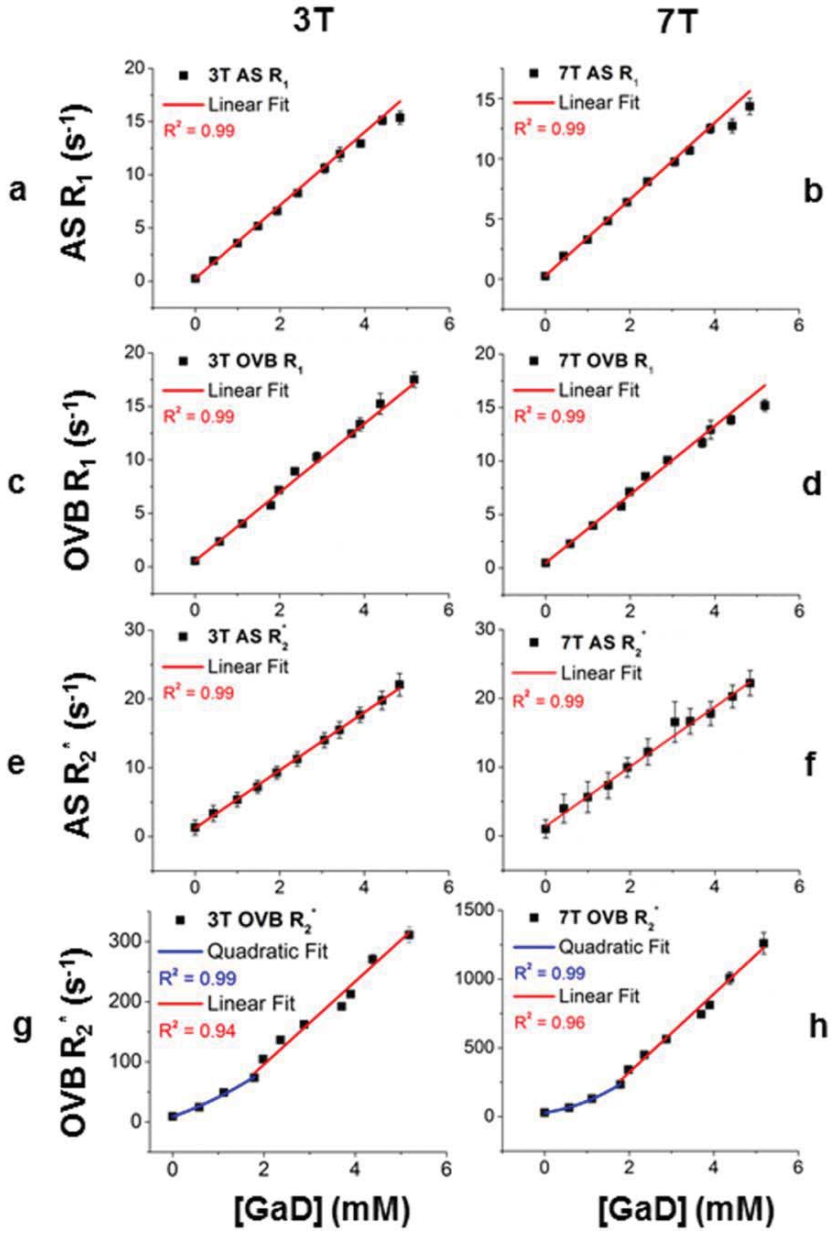

Figure 5.2 Plots of R_1 and R_2* vs [GaD] for oxygenated venous blood (OVB) and aqueous solution (AS) at 3 and 7 T. Plots of relaxivity modeled with linear (red) and quadratic (blue) functions are shown. A linear model was used to calculate R_1 relaxivity (r_1) for 3 and 7 T in both AS (a, b) and OVB (c, d). A linear model was also used to calculate R_2* relaxivity (r_2*) in AS (e, f). To determine r_2* in OVB, a quadratic function for [GaD] ≤ 2 mM and linear function for [GaD] ≥ 2 mM was found to characterize the data better than a quadratic fit alone over the whole range of [GaD] (g, h).

5.6 Discussion

The r_1 and r_2^* relaxivities of GaD depend on R_1 and R_2^* which in turn depend on many factors such as macromolecular content, temperature, pH, magnetic field strength, acquisition parameters and oxygenation. To put the values obtained in this study in the context of previous work, r_1 of GaD in water and blood obtained under similar experimental conditions are included in Tables 5.5 and 5.6, respectively. While previous studies investigating r_2^* of GaD have not been performed to date, native R_2^* in blood has been of great interest. Values at 1.5T have shown arterial blood to have values ranging from 3.94±0.50(126) to 5.02±0.2(127) s^{-1}. In the current study, large increases in native blood R_2^* were measured at 3T and 7T; 9.94±0.56 and 28.50±1.15 s^{-1}, respectively.

Reference no.	Year.	Solution type	Temperature (°C)	B_0 (T)	r_1 ($mM^{-1}s^{-1}$)	[GaD] (mM)	Scan type	Scanner	pH	*TE* (ms)	*TR* (ms)	*TI* (ms)
Our data	2013	AS	37±2	3	3.44±0.08	0-4.83	TF	ST	7	1.3	10000	20-9000
Our data	2013	AS	37±2	7	3.18±0.09	0-4.83	TF	M7T	7	1.1	10000	20-9000
114	1997	DW	38	1.5	2.95	0.01-5.93	SPIRFL	SM63SP	-	20	1000	25-6000
11	2005	W	37	0.47	3.4±0.2	0.25,0.5	TPIR	BPC20	-	-	-	-
11	2005	W	37	1.5	3.3±0.2	0.25,0.5	TPIR	SM	-	-	-	-
11	2005	W	37	3	3.1±0.2	0.25,0.5	TPIR	SMT	-	-	-	-
11	2005	W	37	4.7	3.2±0.2	0.25,0.5	TPIR	VI	-	-	-	-
12	1999	W	37	6.3	3.00±0.56	-	IR	HBNMRS	-	-	-	-

â	per kg of H2O	ST	Siemens Trio	TPIR	Two Pulse Inversion Recovery
W	Water	M7T	Magnex7T	BPC20	Bruker PC20 NMR Analyzer
DW	Deionized Water	SPIRFL	Single Point Inversion Recovery Flash	SM	Siemens Magnetom
TF	Turbo Flash	SM63SP	Siemens Magnetom 63SP	SMT	Siemens Magnetom Trio
VI	Varian Inova	WB	Water Baseline	HBNMRS	Home Built NMR Spectrometer

Table 5.5 A review of T_1 relaxivities (r_1) of Gd-DTPA (GaD) in water published in literature.

Reference no.	Year	Solution type	Temperature (°C)	B_0 (T)	r_1 ($mM^{-1}s^{-1}$)	[GaD] (mM)	Scan type	Scanner type	*TE* (ms)	*TR* (ms)	*TI* (ms)
Our data	2013	OVB	37±2	3	3.20±0.06	0-5.18	TF	ST	1.3	10000	20-9000
Our data	2013	OVB	37±2	7	3.20±0.06	0-5.18	TF	M7T	1.1	10000	20-9000
55	1999	HB	37	1.5	3.92	0-5	RFSSGE	VFR	-	-	-
11	2005	CB	37	1.5	4.3±0.3	0.2-0.5	TPIR	SM	-	-	-

CB	Canine Blood	VFR	Variable Field Relaxometer
HB	Human Blood	ST	Siemens Trio
TF	Turbo Flash	M7T	Magnex 7T
RFSSGE	R_f Spoiled Segmented Gradient Echo	SM	Siemens Magnetom
TPIR	Two Pulse Inversion Recovery		

Table 5.6 A review of T1 relaxivities (r1) of Gd-DTPA (GaD) in blood published in literature.

5.6.1 Dependence of R_2^* on Oxygenation and GaD in Blood

The characteristic linear relationship between R_2^* and [GaD] observed in AS was not observed in OVB. Blood has three major distinguishing characteristics from a homogenous sample such as AS. First, compared to saline, blood experiences longer motional correlation times (slow motion) resulting in increased proton-electron dipolar coupling. Second, it is multi-compartmental, consisting of the plasma and red blood cells (RBCs), where GaD (only present in the plasma) affects magnetic susceptibility differences between RBC and plasma. Third, it contains hemoglobin, the oxygen saturation of which also impacts the susceptibility mismatch between the two compartments. In the case of fully oxygenated blood, the multiple compartments, and the dynamic processes between them, most likely results in the complex relationships observed between R_2^* and [GaD].

In the full range of physiological conditions, the oxygen dependence of blood R_2^* is usually attributed to oxygenation based susceptibility of red blood cells (RBCs) where oxyhemoglobin is diamagnetic and de-oxyhemoglobin is paramagnetic, relative to blood plasma. In OVB, microscopic magnetic field gradients are set up between RBCs and plasma resulting in static and dynamic dephasing of spins that can result in an increase in R_2^* (128).

In deoxygenated blood, it was shown in a study by Blockley et al. that a quadratic behavior existed between R_2^* and [CA] (ProHance) (128). In this previous study a parabolic curve was fit to the data with the inflection point occurring at increasing concentrations with increasing field strength (1.0 mM and 1.3 mM at 3.0T and 7.0T, respectively). This relationship was described as originating from an initial susceptibility difference between the paramagnetic RBCs and the diamagnetic plasma in deoxygenated blood. As the [CA] increases

there is likely an increase in the net paramagnetism of blood plasma which could lead to an averaging of the RBC versus plasma susceptibility variations. The inflection point in the R_2^* curve represented the point at which the CA increases the paramagnetism of the plasma to match that of the RBCs. Beyond this point, the susceptibility difference between plasma and blood again increased as did R_2^*.

In the current study, oxygenated blood is investigated where the RBC are diamagnetic with respect to the blood plasma. While there is no inflection point observed in this data there is still an observed quadratic relationship between R_2^* and [Gad] at lower concentrations from 0-2 mM, however a quadratic function did not sufficiently describe the data above this range. The observed quadratic versus linear contributions was significantly different between 3T and 7T. This field dependence could be a result of varying contributions of susceptibility induced versus dipolar relaxation pathways further influenced by varying exchange and diffusion regimes with changes in [GaD].

While this study was not explicitly designed to elucidate the relaxation mechanisms involved, a brief discussion of factors that could contribute to the observed behavior follows. First, in the presence of GaD, which affects the relaxation rate constant of blood plasma predominantly, the regime of isothermal dynamics is shifted towards the intermediate motional regime (IMR) from the fast motional regime (FMR). In this study, because the apparent rate constants were altered by changing the concentration of GaD, and since GaD is only present in the plasma (site A) and not the RBC (site B), the "shutter speed", i.e., $|R_A-R_B|$, of dynamic processes is varied. The dynamic processes which include exchange and diffusion which collectively result in dynamic averaging (DA) and are additionally characterized by the rate constant k_{DA} (129). In this particular case the regime of exchange or diffusion in local susceptibility gradients or intracellular-extracellular water transport are varied with the increase of the concentration of GaD (130). It appears that the presence of increasing GaD in

plasma shifts the regime of the dynamic process by modifying the intrinsic relaxation rate constants at specific magnetic sites A or B undergoing exchange or diffusion, as well as the apparent populations of sites A (i.e., plasma water protons interacting with GaD) or B (RBC water protons). Moving in this direction takes us from a quadratic to a linear relationship with increasing [GaD] where $|R_A - R_B| >> k_{DA}$.

5.6.2 Effect of hyperoxygenation

Based on initial in-house experiments, the OVB samples were necessarily hyperoxygenated in order to maintain the blood at arterial sO_2 levels (sO_2 > 94%) over the complete MR scan period. At our highest pO_2 of 294 mmHg, Othee et al. have shown that the fraction of oxygen in the blood that is freely dissolved and not bound to hemoglobin is approximately 7% compared to 4% when exposed to room air (pO_2 = 138 mmHg)(131). At 8.4T, the increase in dissolved oxygen from 4% to7% would result in a minimal increase of 6% in blood T1 when measured at room temperature (131). In another study, Blockley et al. reported R_1 of whole blood versus (1-*Y*) at 3T and 7T, where '*Y*' represents the fractional sO_2 (128). In our 3T studies where *Y* = 0.97 and 7T studies where *Y* = 1, the predicted longitudinal relaxation times following Blockley's relation would be 1730 ms and 2041 ms, respectively. These values are in excellent agreement to our hyper-oxygenated OVB T_1 values of 1788.09±11.78 ms at 3T and 2055.43±14.00 ms at 7T.

The effect of hyperoxygenation on transverse relaxation is arguably much more complex. Molecular oxygen affects relaxation through paramagnetic interactions and, in addition, could influence magnetic susceptibility variations in the sample thus leading to different conditions of DA. These mechanisms are challenging to characterize and beyond the scope of the presented work. While a potential limitation of the current study, hyperoxygenation was required to maintain arterial sO_2 levels with the chosen experimental methods.

5.6.3 Acquisition Methods

Alternative strategies, both in terms of the experimental setup and data acquisition were also considered for this study. However, the desire to obtain a wide distribution of concentrations at physiological temperature and sO_2 led to the use of the IR-TFL sequence and rapidly imaging samples in an experimental setup with a concentration range from 0-5 mM. Determination of T_1 values using the IR-TFL method was validated with those obtained using the IR-SE sequence with the final values only differing by 3%.

As the Hct in the blood settles over the duration of the study, there is a change in the Hct content in the scanned MRI slice. An increase in Hct will lead to a higher value of r_1. Using the IR-TFL sequence allowed the data to be acquired rapidly in comparison to the IR-SE method which decreased the total data acquisition time from 65 to 12 minutes. Secondly, the vials were positioned vertically to lengthen the distance over which settling would occur. The scan plane was also positioned through the center of the vials to minimize the pile up of Hct at the bottom or the absence of Hct at the top of the vile. Based on repeat data acquisitions, a 0.4% decrease in r_1 per minute and a 0.3% increase in the slope of R_2^* vs. [GaD] per minute was found. Thus, the effect due to settling was minimal in this study.

The challenges with the chosen acquisition methods were T_2^* blurring of the IR-TFL acquisition and the potential for a spatially varying B_0 impacting primarily R_1 and R_2^* calculations, respectively. To minimize the effect of T_2^* blurring, which increases with [GaD], ROIs well within each sample vial were used for R_1 determination. Despite this strategy, slight variations from the linear relaxivity curve are still observed at the highest [GaD], (Figure 5.2 a-d). To address B_0 homogeneity, a local B_0 shim was used. While a majority of the signal used for B_0 shimming originated from the water bath, field perturbations from within and immediately around the samples had the potential of biasing the

global shim. For the AS samples, the expected linear relationship between R_2^* and [Gad] is observed for both 3T and 7T indicating that a reasonably homogeneous B_0 field was obtained with the chosen shimming methods.

This study provides important information on the susceptibility effects on R_2^* relaxation rate constants and their dependence on external static magnetic field in the presence of GaD. Importantly, because the susceptibility induced relaxation channel is one which significantly contributes to the free precession R_2 through its dependence on DA, our study indirectly provides insight into the free precession transverse relaxation of the blood in the presence of GaD as well. It should be emphasized that for accurate estimation of the intrinsic relaxation parameters from T_2 measurements, the measurements of R_2 relaxation dispersion using a Carr-Purcell-Meiboom-Gill (CPMG) acquisition is necessary.

5.7 Conclusion

The r_1 of AS and OVB remained similar both between sample types and field strengths with only minor differences observed. The R_2^* relaxivity of AS was also similar at both 3T and 7T with only a 3% increase at the higher field strength. Furthermore, in AS, r_2^* values at 3T and 7T were only 22% and 36% higher than the respective r_1 values. There was, on the other hand, a large effect of the multi-compartmental nature of blood which resulted in an apparent nonlinear relationship between R_2^* and [GaD] and tremendous increases in r_2^* not observed the homogeneous AS phantom. OVB r_2^* exhibited a large field dependence with an approximate four-fold increase in R_2^* relaxivity at 7T compared the 3T. In addition, OVB r_2^* was twenty-fold higher at 3T and ninety-fold higher at 7T compared to their respective r_1 values.

Knowledge of r_1 and r_2^* relaxivities are paramount to using contrast agents at any field strength. This study demonstrates sharply increasing r_2^* in the multi-compartment blood samples greatly outpaces the relatively static r_1

characteristics with increasing field strengths. Unless accounted for, studies relying on the typical T_1 based contrast enhancement typically afforded by paramagnetic contrast administration at lower field strengths may obtain erroneous results.

Chapter 6 Conclusions

6.1 Summary and Significance of Findings

The American Cancer Society estimates that as of January 1, 2014 there are currently three million men living with PCa in the US alone (132). An estimated 11.9 billion is spent each year in the US on PCa treatment (133). Over the past two decades, MRI has emerged as the leading imaging modality in detection and localization of PCa detection due to its excellent soft tissue contrast and its ability to generate tissue property dependent multi-parametric data (3). The work presented in this thesis leverages these advantages of MP-MRI in both high field and ultra-high field imaging in the development of methods for PCa detection.

6.1.1 LATIS Image Registration

The LATIS image registration method as detailed in Chapter 3 occupies a unique spot among Pathology-MR registration approaches found in literature. In this work we tackle the challenging problem of registering non-whole mount pathology to in vivo MRI data acquired with an endorectal coil in 35 cases and achieve registration accuracy of 1.54±0.65 mm. This registration accuracy along with DICE coefficient value of 0.9911±0.004 allows the confident use of pathology as a gold standard in our setup for developing predictive MRI models of disease. Since work began on this project in 2010 there have been other attempts in this area. Prabu et al. (134) used a free form deformation and statistical deformation model based regularizer to register six cases leading to a mean . Patel et al. (92) used spatial weighted mutual information to register 7

PWM slices and report a mean RMS error of 1.65 mm and mean DICE coefficient of 0.83.

Compared to other methods that require manual identification of numerous control points to facilitate accurate registration, LATIS offers the advantage of manually identifying large structures which is less labor and time intensive. More importantly, in some cases, selecting a sufficient number of control points may not even be possible. Selecting large structures rather than specific points is advantageous as it is makes LATIS potentially more robust in cases where the slicing or imaging plane are close but not exactly the same. While potentially less restrictive than other methods, LATIS still assumes that both source and target are approximately in the same plane through the prostate and still requires user input of identification and marking of structures on both datasets. Another limitation is that the assembling the individual digitized pathology images which compose the PWMHS involves user interaction and is suspect to variability.

6.1.2 MP-MRI Predictive Models

Four MP-MRI models for the prediction of PCa based on co-registered Pathology has been shown in Chapter 4. These models can be used to detect large and small lesions in the PZ (L5P_PZ), all cancer throughout the entire prostate (L3P_ALL) and all cancer versus non-cancer in the CG (L4P_CG and $L3P\_CG_{ROI}$). The second model is most unique and arguably the most useful prospectively as no segmentation of the prostate would be needed prior to applying the model. The third and fourth models are also unique as PCa is most prevalent in the PZ and there has been limited work done in using MP-MRI models for prediction of PCa in CG alone.

While more work still needs to be done in this area a possible application of these models could be the generation of CBS Maps on a voxel-wise basis. These maps would be very useful in guiding biopsies and improving cancer management decisions.

The uniqueness of our approach lies in the use of Pathology-MR coregistered datasets, inclusion of all cancer volumes > 0.19 cc and the use of voxel-wise analysis. With the LATIS based deformable co-registration (Chapter 4) we have reduce the bias in assessing the location and extent of disease in the MRI slice compared to previously proposed methods. While groups have presented similar models for cancer detection, the data imparted by pathology to the MRI has been done manually. In comparison to our modeling approach that uses mapped pathology regions, these other approaches are prone to biases in ROI definition due to subjectivity in operator interpretation of data within MP-MRI and Pathology images.

Future studies will incorporate a T_1-DESPOT1 based cutoff for voxel filtering. The clinical application of these models would require validation of different scanners and acquisition methods. The use of non coregistered datasets in model development might limit the application of these models in the clinic where the goal is to minimize user interactions in data generation. Co-registered datasets are usually not required as long as there is no patient motion. However, in the presence of patient motion and in the case of DWI where EPI-based field distortions are present, registration between the MP-MRI datasets would be necessary. Algorithms incorporating Dynamic Field Correction (DFC) (135) have been developed to account for EPI-based field distortions between the diffusion images. Anti-peristaltic drugs can be used to minimize patient motion. While some studies recommend injection of drugs like glucagon or hyoscine-N-butyl-bromide (HBB, butylscopolamine) for MR studies done at 1.5T (136,137), Roethke et al.(138) demonstrated that there was no significant effect of HBB administration on image quality for MRI studies at 3T. Other options for patient motion correction include the use of motion

correction algorithms(139) and MR sequences like PROPELLER(140). MRI-MRI Co-registration is an active area of investigation (141) and future work can incorporate available methods for this purpose.

These models can be applied at many points in the PCa management. The proposed user-independent generation of cancer biomarker score maps on a voxel-wise basis would assist in guiding biopsies, improve management decisions, increase clinician confidence with suggesting active surveillance rather than receive definitive therapy to their patients, improve monitoring of men over time either on active surveillance or post therapy and target focal therapies as they become used more prevalently used clinically. While a complete analysis has not been done to date, each of these applications could have a tremendous impact by reducing treatment costs, improving outcomes and increasing quality of life for patients by avoiding unnecessary treatment and the commonly occurring side effects of incontinence and impotence.

6.1.3 T_1 and T_2* Relaxivities of Gd-DTPA in Oxygenated Venous Blood and Aqueous Solution at 3 and 7T.

Gd-DTPA (Magnevist™) is one of the most widely used MRI contrast agents (CAs) today. The relaxation enhancement of Gd-DTPA depends on its relaxivity which in turn depends on factors like magnetic field strength, macromolecular content, pH and temperature (12,142-144). Chapter 5 details work done to calculate r_1 and r_2* relaxivities of Gd-DTPA in oxygenated venous blood (OVB) and aqueous solution. The results show that the R_1 relaxivity (r_1) was relatively constant from 3T to 7T in OVB while the R_2* relaxivity (r_2*) increased four-fold. Based on these results, it can be calculated that sub-millisecond T_2* relaxation times at 7T are possible with in-vivo Gd-DTPA concentrations ([GaD]) of 5 mM in

the blood which can be reached with injection rates of 3 ml/s (62). These effects could negatively impact contrast enhanced studies when performed at 7T if not accounted for in the sequence optimization and/or injection strategies. In general, the results from this study has multiple potential uses including 1) optimization of sequence parameters 2) development of contrast injection paradigms 3) calibration curves to determine [Gd] from changes in T_1 and T_2* relaxation rates (R_1 and R_2*).

6.2 Future Work

6.2.1 Correlation of MRI with Quantitative Pathology

In addition to providing information regarding disease location and grade, digital pathology can also be processed to provide valuable quantitative information like percentages of tissue components (like nuclei, stroma, lumen and cytoplasm). It is therefore possible to correlate individual qMR parameters with quantitative pathology to better understand the correspondence between in-vivo MR parameters and anatomic/molecular pathologic status of tissue. An initial exploratory analysis was performed on an eight patient cohort (48) where T_2-SEMC and ADC (cancer and non-cancer) values were correlated to corresponding nuclear density values and grade obtained from pathology. Both T_2-SEMC and ADC values for cancer were found to be lower than normal values in the CG and PZ ($p< 0.0625$ & $p<0.003$, respectively) while cancer nuclear densities were significantly higher (CG: $p<0.003$, PZ: $p< 0.003$). Negative correlations between nuclear density and ADC ($r = -0.98$) and ADC and T_2-SEMC($r = -0.65$) were found for tumor data (145). This study, as well as others (48), demonstrates that there are discernible pathologic features which correlate

with quantitative MRI metrics of PCa thus providing insight into the microstructure of the tissue. While it has been shown that Gleason score correlates positively to increased cellularity (146) and that nuclear density correlates with tumor aggressiveness (147,148), it is unknown how well these microscopic findings correlate to the macroscopic scale we currently operate in when imaging with MRI. The correlation of quantitative histopathological and pre-therapeutic MR parameters using Pathology-MR co-registered data sets, will help address these questions.

6.2.2 Variation of the L5P_CG_{ROI} Model

$NC_{CG\text{-}ROI}$ regions used in the L5P_CG_{ROI} model are obtained from user defined ROIs drawn on slices at least 9 mm away from regions of annotated cancer (Section 4.2.2). A direct comparison cannot be made currently between the L4P_CG and L5P_CG_{ROI} models as the non-cancer data belongs to different slices. To compare these models, user defined non cancer ROIs would need to be drawn with in NC_{CG} regions from Data Pool III. This would enable a comparison of cancer in CG with non-cancer CG data obtained from 1) NC_{CG} and 2) ROIs drawn with in NC_{CG} regions excluding the urethra, areas of fibromuscular cap and post-biopsy hemorrhage.

Bibliography

1. Ferlay J, Soerjomataram I, Ervik M, et al. GLOBOCAN 2012 v1.0, Cancer Incidence and Mortality Worldwide: IARC CancerBase No. 11 [Internet].Lyon, France: International Agency for Research on Cancer; 2013.Available from http://globocan.iarc.fr, accessed on 05/09/2014. 2012.
2. Langer DL. Multi-parametric Magnetic Resonance Imaging (MRI) in Prostate Cancer. Volume NR73119. Ann Arbor: University of Toronto (Canada); 2010. p. 145.
3. Jacobs MA, Mitsias P, Soltanian-Zadeh H, et al. Multiparametric MRI Tissue Characterization in Clinical Stroke With Correlation to Clinical Outcome Part 2. Stroke 2001;32(4):950-957.
4. Metzger GJB, P.J. Influence of contrast-dependent T2* effects on DCE-MRI of the prostate at 7T. Proc Intl Soc Mag Reson Med 17 2009:4369p.
5. Umutlu L, Maderwald S, Kinner S, et al. First-pass contrast-enhanced renal MRA at 7 Tesla: initial results. European radiology 2013;23(4):1059-1066.
6. Siegel R, Ma J, Zou Z, Jemal A. Cancer statistics, 2014. CA: A Cancer Journal for Clinicians 2014;64(1):9-29.
7. Howlader N, Noone AM, Krapcho M, et al. SEER Cancer Statistics Review, 1975-2011, National Cancer Institute. Bethesda, MD,http://seer.cancer.gov/csr/1975_2011/, based on November 2013 SEER data submission, posted to the SEER web site, April 2014. Accessed on May 22 2014. 2014.
8. Dasgupta P, Kirby RS. ABC of Prostate Cancer: John Wiley & Sons: 2011. 84 p.
9. Snell RS. Clinical Anatomy by Regions: Lippincott Williams & Wilkins: 2011.766p.
10. Cleveland Clinic - The Male Reproductive System. http://my.clevelandclinic.org/anatomy/male_reproductive_system/hic_the_male_reproductive_system.aspx. Accessed on 2014-05-28 Cleveland Clinic.
11. Rohrer M, Bauer H, Mintorovitch J, Requardt M, Weinmann H-J. Comparison of magnetic properties of MRI contrast media solutions at different magnetic field strengths. Invest Radiol 2005;40(11):715-724.
12. Rozijn T, van der Sanden B, Heerschap A, Creyghton J, Bovee W. Determination of in vivo rat muscle Gd-DTPA relaxivity at 6.3 T. Magnetic Resonance Materials in Physics, Biology and Medicine 1999;9(1):65-71.
13. Vas deferens. http://en.wikipedia.org/w/index.php?title=Vas_deferens&oldid=606116373. Accessed on 5/28/2014. Wikipedia, the free encyclopedia 2014.
14. Lee CH, Akin-Olugbade O, Kirschenbaum A. Overview of prostate anatomy, histology, and pathology. Endocrinology and metabolism clinics of North America 2011;40(3):565-575, viii-ix.
15. Roch A, Muller RN, Gillis P. Theory of proton relaxation induced by superparamagnetic particles. J Chem Phys 1999;110(11):5403-5411.

16. Chun FKH, Epstein JI, Ficarra V, et al. Optimizing Performance and Interpretation of Prostate Biopsy: A Critical Analysis of the Literature. Eur Urol 2010;58(6):851-864.
17. Mayes JM, Mouraviev V, Sun L, Tsivian M, Madden JF, Polascik TJ. Can the conventional sextant prostate biopsy accurately predict unilateral prostate cancer in low-risk, localized, prostate cancer? Urologic Oncology: Seminars and Original Investigations 2011;29(2):166-170.
18. Sasaki M, Shibata E, Kanbara Y, Ehara S. Enhancement effects and relaxivities of gadolinium-DTPA at 1.5 versus 3 Tesla: a phantom study. Magn Reson Med Sci 2005;4(3):145-149.
19. Rosensweig RE. Heating magnetic fluid with alternating magnetic field. J Magn Magn Mater 2002;252(1-3):370-374.
20. Schwab M. Encyclopedia of Cancer: Springer: 2008. 3307 p.
21. Leyendecker JR, Oliphant M. Problem Solving in Abdominal Imaging with CD-ROM: Elsevier Health Sciences: 2009. 740 p.
22. Tewari A. Prostate Cancer: A Comprehensive Perspective: A Comprehensive Perspective: Springer: 2013. 1090 p.
23. Ives EP, Burke MA, Edmonds PR, Gomella LG, Halpern EJ. Quantitative Computed Tomography Perfusion of Prostate Cancer: Correlation with Whole-Mount Pathology. Clinical Prostate Cancer 2005;4(2):109-112.
24. Cyran CC, von Einem JC, Paprottka PM, et al. Dynamic Contrast-Enhanced Computed Tomography Imaging Biomarkers Correlated With Immunohistochemistry for Monitoring the Effects of Sorafenib on Experimental Prostate Carcinomas. Invest Radiol 2012;47(1):49-57 10.1097/RLI.1090b1013e3182300fe3182304.
25. Penzkofer T, Tempany-Afdhal CM. Prostate cancer detection and diagnosis: the role of MR and its comparison with other diagnostic modalities--a radiologist's perspective. NMR Biomed 2014;27(1):3-15.
26. Farsad M, Schiavina R, Castellucci P, et al. Detection and localization of prostate cancer: correlation of 11C-choline PET/CT with histopathologic step-section analysis. Journal of Nuclear Medicine 2005;46(10):1642-1649.
27. Giovacchini G, Picchio M, Coradeschi E, et al. [11C] choline uptake with PET/CT for the initial diagnosis of prostate cancer: relation to PSA levels, tumour stage and anti-androgenic therapy. European journal of nuclear medicine and molecular imaging 2008;35(6):1065-1073.
28. Kwee SA, Coel MN, Lim J, Ko JP. Prostate Cancer Localization with 18Fluorine Fluorocholine Positron Emission Tomography. The Journal of Urology 2005;173(1):252-255.
29. Dickinson L, Ahmed HU, Allen C, et al. Magnetic resonance imaging for the detection, localisation, and characterisation of prostate cancer: recommendations from a European consensus meeting. Eur Urol 2011;59(4):477-494.
30. Durmus T, Baur A, Hamm B. Multiparametric Magnetic Resonance Imaging in the Detection of Prostate Cancer. Aktuelle Urologie 2014;45(2):119-126.
31. Hedgire SS, Oei TN, McDermott S, Cao K, Patel M Z, Harisinghani MG. Multiparametric magnetic resonance imaging of prostate cancer. The Indian journal of radiology & imaging 2012;22(3):160-169.

32. Hegde JV, Mulkern RV, Panych LP, et al. Multiparametric MRI of prostate cancer: an update on state-of-the-art techniques and their performance in detecting and localizing prostate cancer. J Magn Reson Imaging 2013;37(5):1035-1054.
33. Kurhanewicz J, Vigneron D, Carroll P, Coakley F. Multiparametric magnetic resonance imaging in prostate cancer: present and future. Curr Opin Urol 2007;18(1):71-77.
34. Moradi M, Salcudean SE, Chang SD, et al. Multiparametric MRI maps for detection and grading of dominant prostate tumors. J Magn Reson Imaging 2012;35(6):1403-1413.
35. Kobus T, Vos PC, Hambrock T, et al. Prostate cancer aggressiveness: in vivo assessment of MR spectroscopy and diffusion-weighted imaging at 3 T. Radiology 2012;265(2):457-467.
36. Verma S, Rajesh A, Morales H, et al. Assessment of aggressiveness of prostate cancer: correlation of apparent diffusion coefficient with histologic grade after radical prostatectomy. AJR Am J Roentgenol 2011;196(2):374-381.
37. Vos EK, Litjens GJ, Kobus T, et al. Assessment of prostate cancer aggressiveness using dynamic contrast-enhanced magnetic resonance imaging at 3 T. Eur Urol 2013;64(3):448-455.
38. Wang L, Mazaheri Y, Zhang J, Ishill NM, Kuroiwa K, Hricak H. Assessment of biologic aggressiveness of prostate cancer: correlation of MR signal intensity with Gleason grade after radical prostatectomy. Radiology 2008;246(1):168-176.
39. Roethke M, Anastasiadis AG, Lichy M, et al. MRI-guided prostate biopsy detects clinically significant cancer: analysis of a cohort of 100 patients after previous negative TRUS biopsy. World Journal of Urology 2012;30(2):213-218.
40. Thompson JE, Moses D, Shnier R, et al. Multiparametric Magnetic Resonance Imaging Guided Diagnostic Biopsy Detects Significant Prostate Cancer and could Reduce Unnecessary Biopsies and Over Detection: A Prospective Study. The Journal of Urology (0).
41. Langer DL, van der Kwast TH, Evans AJ, Trachtenberg J, Wilson BC, Haider MA. Prostate cancer detection with multi-parametric MRI: logistic regression analysis of quantitative T2, diffusion-weighted imaging, and dynamic contrast-enhanced MRI. J Magn Reson Imaging 2009;30(2):327-334.
42. Matulewicz L, Jansen JF, Bokacheva L, et al. Anatomic segmentation improves prostate cancer detection with artificial neural networks analysis of H magnetic resonance spectroscopic imaging. J Magn Reson Imaging 2013.
43. Anderson D, Golden B, Wasil E, Zhang H. Predicting prostate cancer risk using magnetic resonance imaging data. Inf Syst E-Bus Manage 2014:1-10.
44. Delongchamps NB, Rouanne M, Flam T, et al. Multiparametric magnetic resonance imaging for the detection and localization of prostate cancer: combination of T2-weighted, dynamic contrast-enhanced and diffusion-weighted imaging. 2011;107(9):1411-1418.
45. Litjens G, Debats O, Barentsz J, Karssemeijer N, Huisman H. Computer-Aided Detection of Prostate Cancer in MRI. Medical Imaging, IEEE Transactions on 2014;33(5):1083-1092.
46. Poulakis V, Witzsch U, de Vries R, et al. Preoperative neural network using combined magnetic resonance imaging variables, prostate-specific antigen, and

gleason score for predicting prostate cancer biochemical recurrence after radical prostatectomy. Urology 2004;64(6):1165-1170.
47. Puech P, Betrouni N, Makni N, Dewalle AS, Villers A, Lemaitre L. Computer-assisted diagnosis of prostate cancer using DCE-MRI data: design, implementation and preliminary results. International journal of computer assisted radiology and surgery 2009;4(1):1-10.
48. Kalavagunta C, Zhou X, Schmechel SC, Metzger GJ. Registration of in vivo prostate MRI and pseudo-whole mount histology using Local Affine Transformations guided by Internal Structures (LATIS). J Magn Reson Imaging 2014.
49. Chan I, Wells W, Mulkern RV, et al. Detection of prostate cancer by integration of line-scan diffusion, T2-mapping and T2-weighted magnetic resonance imaging; a multichannel statistical classifier. Medical Physics 2003;30(9):2390-2398.
50. Liney GP, Knowles AJ, Manton DJ, Turnbull LW, Blackband SJ, Horsman A. Comparison of conventional single echo and multi-echo sequences with a fast spin-echo sequence for quantitative T2 mapping: Application to the prostate. Journal of Magnetic Resonance Imaging 1996;6(4):603-607.
51. Liney GP, Turnbull LW, Lowry M, Turnbull LS, Knowles AJ, Horsman A. In vivo quantification of citrate concentration and water T2 relaxation time of the pathologic prostate gland using 1H MRS and MRI. Magn Reson Imaging 1997;15(10):1177-1186.
52. Gibbs P, Tozer DJ, Liney GP, Turnbull LW. Comparison of quantitative T2 mapping and diffusion-weighted imaging in the normal and pathologic prostate. Magn Reson Med 2001;46(6):1054-1058.
53. Biasiolli L, Lindsay A, Chai J, Choudhury R, Robson M. In-vivo quantitative T2 mapping of carotid arteries in atherosclerotic patients: segmentation and T2 measurement of plaque components. Journal of Cardiovascular Magnetic Resonance 2013;15(1):69.
54. Homer J, Beevers MS. Driven-equilibrium single-pulse observation of T1 relaxation. A reevaluation of a rapid “new” method for determining NMR spin-lattice relaxation times. Journal of Magnetic Resonance (1969) 1985;63(2):287-297.
55. Tan CH, Wei W, Johnson V, Kundra V. Diffusion Weighted Magnetic Resonance Imaging in Prostate Cancer: Meta-analysis. AJR Am J Roentgenol 2012;199(4):822-829.
56. Johansen-Berg H, Behrens TEJ. Diffusion MRI: From Quantitative Measurement to In vivo Neuroanatomy: Academic Press: 2013. 1186 p.
57. Zelhof B, Pickles M, Liney G, et al. Correlation of diffusion-weighted magnetic resonance data with cellularity in prostate cancer. BJU international 2009;103(7):883-888.
58. Thoeny HC, De Keyzer F, Boesch C, Hermans R. Diffusion-weighted imaging of the parotid gland: Influence of the choice of b-values on the apparent diffusion coefficient value. J Magn Reson Imaging 2004;20(5):786-790.
59. Le Bihan D, Breton E, Lallemand D, Aubin ML, Vignaud J, Laval-Jeantet M. Separation of diffusion and perfusion in intravoxel incoherent motion MR imaging. Radiology 1988;168(2):497-505.

60. Low RN, Fuller DB, Muradyan N. Dynamic Gadolinium-Enhanced Perfusion MRI of Prostate Cancer: Assessment of Response to Hypofractionated Robotic Stereotactic Body Radiation Therapy. American Journal of Roentgenology 2011;197(4):907-915.
61. Tofts PS. Modeling tracer kinetics in dynamic Gd-DTPA MR imaging. Journal of Magnetic Resonance Imaging 1997;7(1):91-101.
62. Parker GJ, Roberts C, Macdonald A, et al. Experimentally-derived functional form for a population-averaged high-temporal-resolution arterial input function for dynamic contrast-enhanced MRI. Magnetic resonance in medicine : official journal of the Society of Magnetic Resonance in Medicine / Society of Magnetic Resonance in Medicine 2006;56(5):993-1000.
63. Li X, Welch EB, Chakravarthy AB, et al. Statistical comparison of dynamic contrast-enhanced MRI pharmacokinetic models in human breast cancer. Magnetic resonance in medicine : official journal of the Society of Magnetic Resonance in Medicine / Society of Magnetic Resonance in Medicine 2012;68(1):261-271.
64. Tofts P. T1-weighted DCE Imaging Concepts: Modelling, Acquisition and Analysis. MAGNETOM Flash; 2010. p. 30.
65. Aalst WV, Twellmann T, Buurman H, Gerritsen F, Romeny BMH. Use of T2-weighted images in computer-aided diagnosis for breast MRI. Proceedings of the European Congress of Radiology (ECR 2008). Vienna, Austria: European Society of Radiology; 2008. p. C-591.
66. Langer DL, van der Kwast TH, Evans AJ, Trachtenberg J, Wilson BC, Haider MA. Prostate cancer detection with multi-parametric MRI: logistic regression analysis of quantitative T2, diffusion-weighted imaging, and dynamic contrast-enhanced MRI. J Magn Reson Imaging 2009;30(2):327-334.
67. Turkbey B, Pinto PA, Mani H, et al. Prostate Cancer: Value of Multiparametric MR Imaging at 3 T for Detection—Histopathologic Correlation 1. Radiology 2010;255(1):89-99.
68. Vilanova JC, Barceló-Vidal C, Comet J, et al. Usefulness of prebiopsy multifunctional and morphologic MRI combined with free-to-total prostate-specific antigen ratio in the detection of prostate cancer. AJR Am J Roentgenol 2011;196(6):W715-722.
69. McLaughlin PW, Narayana V, Kessler M, et al. The use of mutual information in registration of CT and MRI datasets post permanent implant. Brachytherapy 2004;3(2):61-70.
70. Lian J, Xing L, Hunjan S, et al. Mapping of the prostate in endorectal coil-based MRI/MRSI and CT: a deformable registration and validation study. Medical physics 2004;31(11):3087-3094.
71. Mizowaki T, Cohen GaN, Fung AYC, Zaider M. Towards integrating functional imaging in the treatment of prostate cancer with radiation: the registration of the MR spectroscopy imaging to ultrasound/CT images and its implementation in treatment planning. International Journal of Radiation Oncology*Biology*Physics 2002;54(5):1558-1564.
72. Parker CC, Damyanovich A, Haycocks T, Haider M, Bayley A, Catton CN. Magnetic resonance imaging in the radiation treatment planning of localized

prostate cancer using intra-prostatic fiducial markers for computed tomography co-registration. Radiother Oncol 2003;66(2):217-224.
73. Hu Y, Ahmed HU, Allen C, et al. MR to Ultrasound Image Registration for Guiding Prostate Biopsy and Interventions. In: Yang G-Z, Hawkes D, Rueckert D, Noble A, Taylor C, editors. Medical Image Computing and Computer-Assisted Intervention – MICCAI 2009. Volume 5761. Berlin, Heidelberg: Springer Berlin Heidelberg; 2009. p. 787-794.
74. Groenendaal G, Moman MR, Korporaal JG, et al. Validation of functional imaging with pathology for tumor delineation in the prostate. Radiother Oncol 2010;94(2):145-150.
75. Hadamard J. Sur les problèmes aux dérivées partielles et leur signification physique. Princeton university bulletin 1902;13(49-52):28.
76. König D, Rolski T, Schmidt V, Stoyan D. Stochastic processes with imbedded marked point processes (pmp) and thcir application in queneing. Mathematische Operationsforschung und Statistik Series Optimization 1978;9(1):125-141.
77. Ekeland I. On the variational principle. Journal of Mathematical Analysis and Applications 1974;47(2):324-353.
78. Periaswamy S, Weaver JB, Healy JDM, Rockmore DN, Kostelec PJ, Farid H. Differential affine motion estimation for medical image registration. In: Akram A, A.F. L, Unser MA, editors. Proceedings of the Medical Imaging 2000: Wavelet Applications in Signal and Image Processing. Volume 4119. San Diego, California, United States: SPIE; 2000. p. 1066-1075.
79. Periaswamy S, Farid H. Elastic registration in the presence of intensity variations. IEEE Transactions on Medical Imaging 2003;22(7):865-874.
80. Periaswamy S. General purpose medical image registration. Computer Science. Ann Arbor: Dartmouth College; 2003. p. 158-158 p.
81. Viswanath S, Bloch BN, Genega E, et al. A comprehensive segmentation, registration, and cancer detection scheme on 3 Tesla in vivo prostate DCE-MRI. Med Image Comput Comput Assist Interv Int Conf Med Image Comput Comput Assist Interv 2008;11(Pt 1):662-669.
82. Chappelow J, Madabhushi A. Multi-attribute combined mutual information (MACMI): An image registration framework for leveraging multiple data channels. In: Niessen WJ, Meijering E, editors. Proceedings of the 2010 7th IEEE International Symposium on Biomedical Imaging: From Nano to Macro. Rotterdam, Netherlands; 2010. p. 376-379.
83. Ward AD, Crukley C, McKenzie C, et al. Registration of in vivo prostate magnetic resonance images to digital histopathology images. Proceedings of International Workshop on Prostate cancer imaging: computer-aided diagnosis, prognosis, and intervention, Held in Conjunction with MICCAI 2010, MICCAI'10. Beijing, China: Springer-Verlag; 2010. p. 66-76.
84. Ward AD, Crukley C, McKenzie CA, et al. Prostate: registration of digital histopathologic images to in vivo MR images acquired by using endorectal receive coil. Radiology 2012;263(3):856-864.
85. Jo HH, Jung J, Jang Y, Hong H, Lee HJ. Histopathology and MR image fusion of the prostate. In: Reinhardt JM, Pluim JPW, editors. Proceedings of the Medical Imaging 2008: Image Processing. Volume 6914. San Diego, CA, USA SPIE; 2008. p. 691430-691430.

86. Park H, Kwee S, Thibault GP, et al. Registration methods for histological slides and ex vivo MRI of prostate. Proceedings of the 2007 IEEE Nuclear Science Symposium Conference. Volume 4. Honolulu, Hawaii, United States; 2007. p. 3102-3104.
87. Alic L, Haeck JC, Klein S, et al. Multi-modal image registration: matching MRI with histology. In: C. MR, Weaver JB, editors. Proceedings of the Medical Imaging 2010: Biomedical Applications in Molecular, Structural, and Functional Imaging. Volume 7626. San Diego, California, United States: SPIE; 2010. p. 762603-762609.
88. Chappelow J, Madabhushi A, Rosen M, Tomaszeweski J, Feldman M. Multimodal image registration of ex vivo 4 Tesla MRI with whole mount histology for prostate cancer detection. In: Pluim JPW, M. RJ, editors. Proceedings of the Medical Imaging 2007: Image Processing. Volume 6512. San Deigo, California, United States: SPIE; 2007. p. 65121S-65121S-65112.
89. Zhan Y, Ou Y, Feldman M, Tomaszeweski J, Davatzikos C, Shen D. Registering Histological and MR Images of Prostate for Image-based Cancer Detection. Acad Radiol 2007;14(11):1367-1381.
90. Ou Y, Shen D, Feldman M, Tomaszewski J, Davatzikos C. Non-rigid registration between histological and MR images of the prostate: A joint segmentation and registration framework. Proceedings of the 2009 IEEE Computer Society Conference on Computer Vision and Pattern Recognition Workshops. Volume 0. Miami, Florida, USA: IEEE Computer Society; 2009. p. 125-132.
91. Chappelow J, Madabhushi A, Rosen M, Tomaszeweski J, Feldman M. A combined feature ensemble based mutual information scheme for robust inter-modal, inter-protocol image registration. Proceedings of the 2007 4th IEEE International Symposium on Biomedical Imaging: From Nano to Macro. Arlington, Virginia, United States: IEEE; 2007. p. 644-647.
92. Patel P, Chappelow J, Tomaszewski J, et al. Spatially weighted mutual information (SWMI) for registration of digitally reconstructed ex vivo whole mount histology and in vivo prostate MRI. Engineering in Medicine and Biology Society,EMBC, 2011 Annual International Conference of the IEEE; 2011. p. 6269-6272.
93. Bookstein FL. Principal warps: thin-plate splines and the decomposition of deformations. IEEE Transactions on Pattern Analysis and Machine Intelligence 1989;11(6):567-585.
94. Kybic J, Unser M. Fast parametric elastic image registration. IEEE Transactions on Image Processing 2003;12(11):1427-1442.
95. Xie Z, Farin GE. Image registration using hierarchical B-splines. IEEE Transactions on Visualization and Computer Graphics 2004;10(1):85-94.
96. Meyer CR, Moffat BA, Kuszpit KK, et al. A methodology for registration of a histological slide and in vivo MRI volume based on optimizing mutual information. Mol Imaging 2006;5(1):16-23.
97. Pluim JPW, Maintz JBA, Viergever MA. Image registration by maximization of combined mutual information and gradient information. IEEE Transactions on Medical Imaging 2000;19(8):809-814.

98. Pluim JPW, Maintz JBA, Viergever MA. Mutual-information-based registration of medical images: a survey. IEEE Transactions on Medical Imaging 2003;22(8):986-1004.
99. Viola P, Wells WMIII. Alignment by maximization of mutual information. Proceeding of the 1995 IEEE 5th International Conference on Computer Vision. Cambridge, Massachusetts, United States; 1995. p. 16-23.
100. Wells WM, 3rd, Viola P, Atsumi H, Nakajima S, Kikinis R. Multi-modal volume registration by maximization of mutual information. Medical image analysis 1996;1(1):35-51.
101. Boldea V, Sharp GC, Jiang SB, Sarrut D. 4D-CT lung motion estimation with deformable registration: quantification of motion nonlinearity and hysteresis. Medical Physics 2008;35(3):1008-1018.
102. Brock KK, Nichol AM, Ménard C, et al. Accuracy and sensitivity of finite element model-based deformable registration of the prostate. Medical Physics 2008;35.
103. Brock KK, Sharpe MB, Dawson LA, Kim SM, Jaffray DA. Accuracy of finite element model-based multi-organ deformable image registration. Medical Physics 2005;32(6).
104. Dice LR. Measures of the amount of ecologic association between species. Ecology 1945;26(3):297-302.
105. Fitzpatrick JM, Hill DLG, Shyr Y, West J, Studholme C, Maurer CR. Visual assessment of the accuracy of retrospective registration of MR and CT images of the brain. IEEE Transactions on Medical Imaging 1998;17(4):571-585.
106. Kaus MR, Brock KK, Pekar V, Dawson LA, Nichol AM, Jaffray DA. Assessment of a model-based deformable image registration approach for radiation therapy planning. Int J Radiat Oncol Biol Phys 2007;68(2):572-580.
107. Rietzel E, Chen GTY. Deformable registration of 4D computed tomography data. Medical Physics 2006;33.
108. Wong JCH, Studholme C, Hawkes DJ, Maisey MN. Evaluation of the limits of visual detection of image misregistration in a brain fluorine-18 fluorodeoxyglucose PET MRI study. European Journal of Nuclear Medicine 1997;24:642-650.
109. Woods RP. Validation of Registration Accuracy. Handbook of Medical Image Processing and Analysis (Second Edition). Burlington: Academic Press; 2009. p. 569-575.
110. R Core Team. R: A Language and Environment for Statistical Computing. Vienna, Austria: R Foundation for Statistical Computing; 2013.
111. Eichelberger LE, Koch MO, Daggy JK, Ulbright TM, Eble JN, Cheng L. Predicting tumor volume in radical prostatectomy specimens from patients with prostate cancer. American journal of clinical pathology 2003;120(3):386-391.
112. Tibshirani R. Regression shrinkage and selection via the lasso. Journal of the Royal Statistical Society Series B (Methodological) 1996:267-288.
113. Held-Warmkessel J. Contemporary Issues in Prostate Cancer: A Nursing Perspective: Jones & Bartlett Learning: 2006. 486 p.
114. Reichenbach JR, Hackländer T, Harth T, Hofer M, Rassek M, Mödder U. 1H T1 and T2 measurements of the MR imaging contrast agents Gd-DTPA and Gd-DTPA BMA at 1.5T. European radiology 1997;7(2):264-274.

115. Polascik TJ. Imaging and Focal Therapy of Early Prostate Cancer: Springer: 2012. 392 p.
116. Karatzoglou A, Smola A, Hornik K, Zeileis A. kernlab - An S4 Package for Kernel Methods in R. Journal of Statistical Software 2004;11(9):1-20.
117. The State of Prostate MRI in 2013-Cancer Network. http://www.cancernetwork.com/oncology-journal/state-prostate-mri-2013. Accessed on 5/28/2014.; 2013.
118. Vos EK, Maas MC, Lagemaat MW, Orzada S, Bitz AK, Scheenen TWJ. Early experiences in Ultra High Field Prostate MR-imaging: Prostate Cancer Detection at 7T Proc Intl Soc Mag Reson Med 21 2013:1790p.
119. Metzger GJ, Auerbach EJ, Warlick CA, Hutter D, Adriany G, I. T. Evaluation of Improved Spatial and Spectral Resolution on Model Based Fitting of Prostate Spectroscopy at 7 Tesla. . Proc Intl Soc Mag Reson Med 20:4390; 2012.
120. Parker GJ, Roberts C, Macdonald A, et al. Experimentally-derived functional form for a population-averaged high-temporal-resolution arterial input function for dynamic contrast-enhanced MRI. Magn Reson Med 2006;56(5):993-1000.
121. Zhang H, Xie Y. Efficiency of paramagnetic relaxation enhancement in off-resonance rotating frame. Journal of magnetic resonance 2006;181(2):212-222.
122. Rinck PA. Magnetic resonance in medicine: the basic textbook of the European Magnetic Resonance Forum: Wiley-Blackwell: 2001. 264 p.
123. Trulock E. Clinical Methods: The History, Physical, and Laboratory Examinations. In: Walker HK HW, Hurst JW,, editor. 3rd ed. Boston: Butterworths; 1990.
124. Scott PV, Horton JN, Mapleson WW. Leakage of oxygen from blood and water samples stored in plastic and glass syringes. British medical journal 1971;3(5773):512-516.
125. Haase A. Snapshot FLASH MRI. Applications to T1, T2, and chemical-shift imaging. Magnetic resonance in medicine : official journal of the Society of Magnetic Resonance in Medicine / Society of 1990;13(1):77-89.
126. Barth M, Moser E. Proton NMR relaxation times of human blood samples at 1.5 T and implications for functional MRI. Cellular and molecular biology (Noisy-le-Grand, France) 1997;43(5):783-791.
127. Li D, Wang Y, Waight DJ. Blood oxygen saturation assessment in vivo usingT2 * estimation. Magnetic Resonance in Medicine 1998;39(5):685-690.
128. Blockley NP, Jiang L, Gardener AG, Ludman CN, Francis ST, Gowland PA. Field strength dependence of R1 and R2* relaxivities of human whole blood to ProHance, Vasovist, and deoxyhemoglobin. Magn Reson Med 2008;60(6):1313-1320.
129. Thulborn KR, Waterton JC, Matthews PM, Radda GK. Oxygenation dependence of the transverse relaxation time of water protons in whole blood at high field. Biochimica et biophysica acta 1982;714(2):265-270.
130. Li X, Springer CS, Jr., Jerosch-Herold M. First-pass dynamic contrast-enhanced MRI with extravasating contrast reagent: evidence for human myocardial capillary recruitment in adenosine-induced hyperemia. NMR Biomed 2009;22(2):148-157.
131. d'Othée BJ, Rachmuth G, Munasinghe J, Lang EV. The effect of hyperoxygenation on T1 relaxation time in vitro1. Acad Radiol 2003;10(8):854-860.

132. Cancer Treatment-Survivor Facts & Figures-American Cancer Society 2014-2015. http://www.cancer.org/research/cancerfactsstatistics/survivor-facts-figures. Accessed on 06/05/2014.
133. Cancer Trends Progress Report - Costs of Cancer Care.http://progressreport.cancer.gov/doc_detail.asp?pid=1&did=2009&chid=95&coid=926&mid=. Accessed on 06/05/2014.
134. Babu Prabu S, Toth R, Madabhushi A. A statistical deformation model (SDM) based regularizer for non-rigid image registration: application to registration of multimodal prostate MRI and histology. Volume 8676; 2013. p. 86760C-86760C-86713.
135. Geppert C, Feiweiher T, Janka R. Reduction of image distortions in breast DWI using dynamic field correction: impact on ADC assessment. Proceedings of the Annual Meeting of ESMRMB. Leipzig: 2011.
136. Dosda R, Marti-Bonmati L, Ronchera-Oms CL, Molla E, Arana E. Effect of subcutaneous butylscopolamine administration in the reduction of peristaltic artifacts in 1.5-T MR fast abdominal examinations. Eur Radiol 2003;13(2):294-298.
137. Barentsz J, Richenberg J, Clements R, et al. ESUR prostate MR guidelines 2012. European radiology 2012;22(4):746-757.
138. Roethke MC, Kuru TH, Radbruch A, Hadaschik B, Schlemmer H-P. Prostate magnetic resonance imaging at 3 Tesla: Is administration of hyoscine-N-butyl-bromide mandatory? World journal of radiology 2013;5(7):259.
139. iCAD: Products - Prostate MRI CAD.http://www.icadmed.com/products/prostate/prostatemri.htm.Accessed on 06/05/2014.
140. Roberts T, Haider M. Diffusion weighted imaging of the prostate gland in the face of magnetic susceptibility differences—parallel EPI and PROPELLER FSE approaches. Proceedings of the ISMRM Twelfth Scientific Meeting, Kyoto, Japan; 2004. p. 946.
141. Alterovitz R, Goldberg K, Pouliot J, et al. Registration of MR prostate images with biomechanical modeling and nonlinear parameter estimation. Med Phys 2006;33(2):446-454.
142. Caravan P, Farrar CT, Frullano L, Uppal R. Influence of molecular parameters and increasing magnetic field strength on relaxivity of gadolinium- and manganese-based T1 contrast agents. Contrast media & molecular imaging 2009;4(2):89-100.
143. Chang CA, Brittain HG, Telser J, Tweedle MF. pH dependence of relaxivities and hydration numbers of gadolinium(III) complexes of linear amino carboxylates. Inorganic Chemistry 1990;29(22):4468-4473.
144. Stanisz GJ, Henkelman RM. Gd-DTPA relaxivity depends on macromolecular content. Magnetic resonance in medicine : official journal of the Society of Magnetic Resonance in Medicine / Society of 2000;44(5):665-667.
145. Kalavagunta C, Warlick C, Zhou X, et al. Analysis of Quantitative MRI and Pathology based on Co-registered Regions of Prostate Cancer. Proc Int Soc Magn Reson Med 2012;20:2996.

146. Garcia FU, Taylor CA, Hou JS, Rukstalis DB, Stearns ME. Increased Cellularity of Tumor-Encased Native Vessels in Prostate Carcinoma Is a Marker for Tumor Progression. 0000;13(7):717-722.
147. Kuwano H, Miyazaki T, Tsutsumi S, et al. Cell Density Modulates the Metastatic Aggressiveness of a Mouse Colon Cancer Cell Line, Colon 26. 2004;67(5-6):441-449.
148. Tworek JA, Appelman HD, Singleton TP, Greenson JK. Stromal tumors of the jejunum and ileum. Mod Pathol 1997;10(3):200-209.